The Pennsylvania State University

The Graduate School

DEFECT ENGINEERING OF TWO-DIMENSIONAL ELECTRONICALLY FUNCITONAL MATERIALS

A Dissertation in

Materials Science and Engineering

by

Fu Zhang

Submitted in Partial Fulfillment
of the Requirements
for the Degree of

Doctor of Philosophy

December 2019

The dissertation of Fu Zhang was reviewed and approved* by the following:

Mauricio Terrones
Distinguished Professor of Physics, Chemistry, and Materials Science and Engineering
Dissertation Advisor
Chair of Committee

Joan A. Redwing
Professor of Materials Science and Engineering, Chemical Engineering, and Electrical Engineering
Associate Director of the Materials Research Institute
Director of the 2D Crystal Consortium – Materials Innovation Platform

Susan Sinnott
Professor of Materials Science and Engineering, and Chemistry
Head of the Department of Materials Science and Engineering

Saptarshi Das
Assistant Professor of Engineering Science& Mechanics

John Mauro
Professor of Materials Science and Engineering
Chair of Intercollege Graduate Degree Program in Materials Science and Engineering

*Signatures are on file in the Graduate School

ABSTRACT

In this thesis, we have carried out a systematic study on the material synthesis, state-of-the-art characterization and property investigations of transition metal dichalcogenides (TMDs) and their heterostructures by defect engineering. First, a defect-controlled approach for the nucleation and epitaxial growth of WSe_2 on hBN is demonstrated. The results reveal an important nucleation mechanism for epitaxial growth of van der Waals heterostructures and indicate that hBN is a superior substrate for synthesizing single crystal TMD films, exhibiting a reduced density of inverted domain boundaries and improved optical and electronic properties. Second, we discuss the synthesis of high quality superconducting α-phase molybdenum carbide (α-Mo_2C) flakes and 2D molybdenum carbide/disulfide heterostructures exhibiting higher superconducting transition temperatures, an insight into the formation mechanism and possible epitaxial-strained or moiré configurations of MoS_2/γ-MoC are discussed to explain the latter. Third, we have used a plasma-assisted method to introduce carbon-hydrogen (CH) units within monolayer WS_2 for the first time. The carbon doping leads to reduction of the optical band gap, and the electronic transport gradually becomes entirely p-type behavior as the carbon doping level increases. Fourth, we have successfully used a single-step powder vaporization method to synthesis vanadium-doped WS_2 (V-WS_2) monolayers with a wide spectrum of vanadium concentrations. Interestingly, as-synthesized V-WS_2 monolayers show a consistent reduction of the optical bandgap and the emergence of the p-type transport branch (reaching ambipolarity), as a function of vanadium concentration. In addition, ferromagnetic ordering is simultaneously induced in monolayer V-WS_2 at room temperature and reaches optimal at ~2%at. vanadium concentrations. We have demonstrated that the electronic, optical and magnetic properties of TMDs could be tuned by defect engineering such as introducing foreign atoms into the lattice or by heterostacks formation. Mechanisms associated with these changes were also elucidated. The results summarized in this thesis could contribute to

the fabrication of next-generation optoelectronic, magneto-optical and magneto-electronic devices, which is foreseen that 2D materials could have practical applications in the near future.

TABLE OF CONTENTS

LIST OF FIGURES

LIST OF TABLES

ACKNOWLEDGEMENTS

I would firstly like to express my sincere thanks and appreciation to my PhD thesis advisor, Prof. Mauricio Terrones, for providing me this precious opportunity working in his research group, and his knowledgeable academic guidance and constant kind encouragement throughout my PhD study. I would like to thank my committee members Dr. Joan Redwing and Dr. Susan Sinnott and Dr. Saptarshi Das for their advice, consideration, time and effort. I would also want to express my sincere thanks to my master thesis advisor Dr. Nasim Alem, for providing me the fascinating research opportunity in graduate school at Penn State, her academic guidance throughout my Master study at Penn State.

I would also like to thank all the research associates Dr. Ana Laura Elias, Dr. Nestor Perea, Dr. Kazunori Fujisawa, and Dr. Yin-Ting Yeh, graduated lab mates Zhong Lin, Yu Lei, Simin Feng, Haoyue Zhu and Chanjing Zhou, for their great guidance and assistance for my PhD study, current lab mates Tianyi Zhang, Mingzu Liu, He Liu, Etahn Kahn and Tomotaroh Granzier-Nakajima, Rosemary Bittel and all the other members in the Terrones group my comrade in arms who shares the joys and sorrows, for their great guidance and assistance for my PhD study, we are a family!

My thanks also go to all my collaborators, especially Dr. Vincent Crespi, Dr. Yuanxi Wang and Boyang Zheng; Dr. Joshua Robinson; Dr. Luis Balicas from FSU and Dr. Manh-Huong Phan from USF; Dr. Xiaotian Zhang and Dr. Tanushree Choudhury; Dr. Daniel Schulman and Amritanand Sebastian, who provide great guidance, assistance and help in my thesis. I would also like to thank wonderful team members at Materials Characterization Lab at Penn State, Ke Wang, Jennifer Gray, Haiying Wang, Jeffrey Shallenberger. I would also like to thank my friends including Yan Dong, Guang Yang, Li Tang for their companionship and consideration always.

Finally, I want to extend my deepest gratitude to my father Xiuli Zhang, my mother Liping Sun for their infinite support, understanding and love for me. Past five years at Penn State is both long and short to me, for meeting so many wonderful people and coming across the adventure, I want to express my sincere thanks to the Pennsylvania State University to provide me this unforgettable experiences and professional trainings. I will always love you and it is such a honor to be a Penn Stater!

Chapter 1

Introduction and Literature Review

1.1 Two-dimensional (2D) materials library

1.1.1 Graphene

Graphene, owns a hexagonal lattice with carbon sp^2 bonds (Fig. 1-1), is an atomically thin layered material that has been widely investigated.[1] Significant scientific breakthroughs have been made in materials science field at 2004 since Novoselov and Geim successfully exfoliated single layer graphene by scotch tape,[1] the achievement in physics investigation of exfoliated graphene is also awarded Nobel prize at 2010. Atomically thin two-dimensional (2D) materials research topics has been burgeoning for last 15 years already from then on. Distinct properties would emerge when materials reduce in one dimension due to quantum effect. Graphene exhibits no band gap in the electronic structure because its crystal structure, act as a semimetal with zero density of state at Fermi level (Figs. 1-1c and d). Graphene endow unique properties such as excellent heat and electrical conductivity, most robust ever tested[2], high opacity[3] and flexibility[4], holding great promise in next generation electronics[5] and optoelectronics[6]. However, graphene-based field effect transistors (FET) fails to effectively function switching off as insulators thus show low on/off ratio. Extensive efforts have been done for open up a small band gap at Fermi level to realize gate/light controllability of carriers, such as chemical functionalization,[7] substitutional nitrogen[8] or boron[9] doping, strain engineering[10] and moiré engineering[11]. Although there is graphene is suitable for

spin carrier for spintronics due to extremely low spin-orbital interaction,[12] lacking of a sizeable band gap (1-2 eV) limit its practical applications as electronics and optoelectronics. Such functionalities could be realized in other 2D nonconducting material systems including dielectric hexagonal boron nitride (hBN), semiconducting layered transition metal dichalcogenides (TMDs).

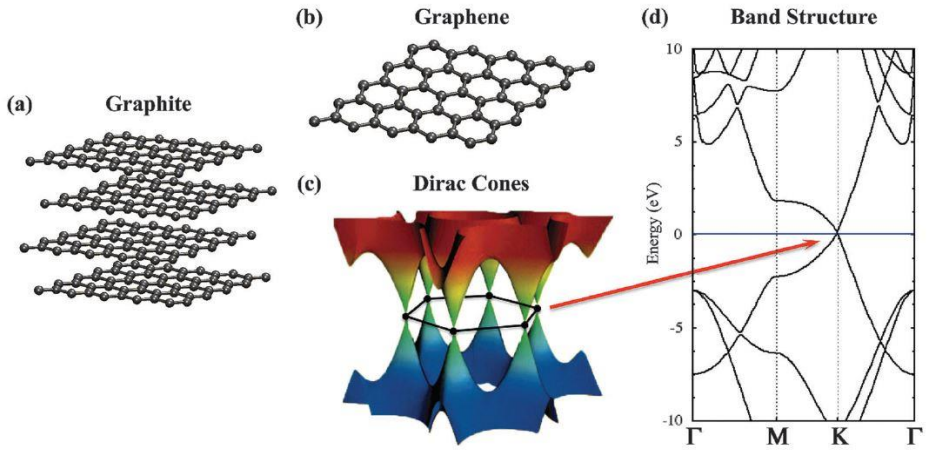

Figure 1- 1 Crystal structure of the (a) bulk graphite and (b) monolayer graphene, respectively; (c) Dirac cones and (d) band structure of monolayer graphene, from Ref [13].

1.1.2 Boron nitride

Hexagonal boron nitride (hBN) as one of various crystalline polymorphs of boron nitride, act as structural analogue of layered graphene. As a thermally conducting yet electrically insulating 2D material[14], hBN owns attractive properties such as high mechanical strength,[15] chemically inert, electron tunneling barrier,[16] and high optical transparency, thus has been lauded as an ideal dielectric layers to maintain the intrinsic electronic and optoelectronic properties of TMDs[17,18] as well as an outstanding template for the growth of vdW heterostructures[19] and building blocks for fabrication of optical[20] and electronic devices[21] (Fig. 1-2). It has been show that semiconducting MoS_2 exhibits less electrically fluctuations on dielectric hBN,[22] which is free of charged surface localized states and charged inhomogeneity, leading to higher carrier mobility of 2D materials (10

times higher than that on oxide Si substrate).[23,24] The lacking of inversion symmetry in hBN also suppress inversion domain formation[25] when synthesizing TMDs thin films to eliminate degrading device performance[26] and possibly inducing undesirable multilayer growth[27].

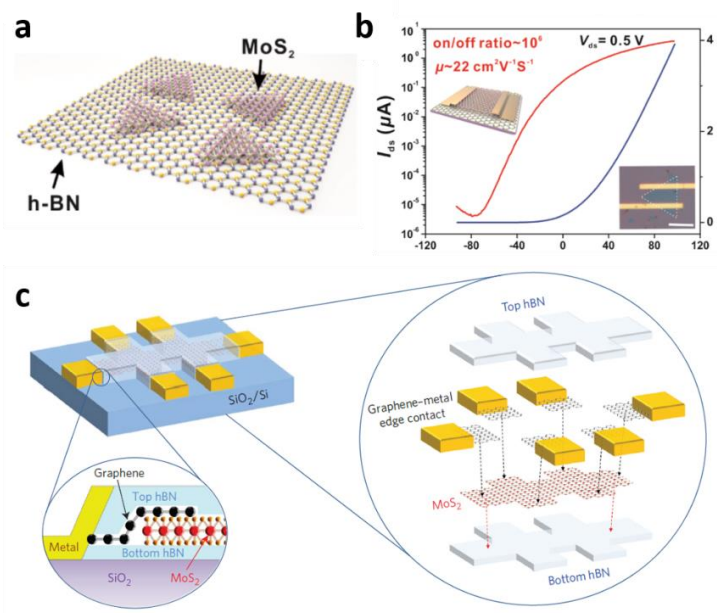

Figure 1- 2 (a) Schematic of MoS_2/BN vertically stacked heterostructures, (b) I_{ds}–V_{gs} curves show the transport characteristics of MoS_2/h-BN heterostructures based FET from Ref [19]; (c) Schematic of Lego heterostack by hBN-encapsulated MoS_2, inset is the anatomy of the building blocks, from Ref [28].

1.1.3 Transition metal dichalcogenides

Layered transition metal dichalcogenides (TMDs) are considered another 2D material system with versatile chemical formula MX_2 which consists of transition metal atoms M (e.g., Mo, W, mostly constrained in groups IV-VI) sandwiched between two layers of chalcogen atoms X (S, Se, Te) (Fig. 1-3), the weak out-of-plane van der Waal bonding and strong in-plane covalent bonding enable isolation of TMDs materials down to monolayers.[29] Two main polytypes of layered TMDs are concreted by above mentioned layers as 2H and 1T phases, the coordination of transition metal atom is trigonal prismatic in 2H phase and octahedral in 1T phase.

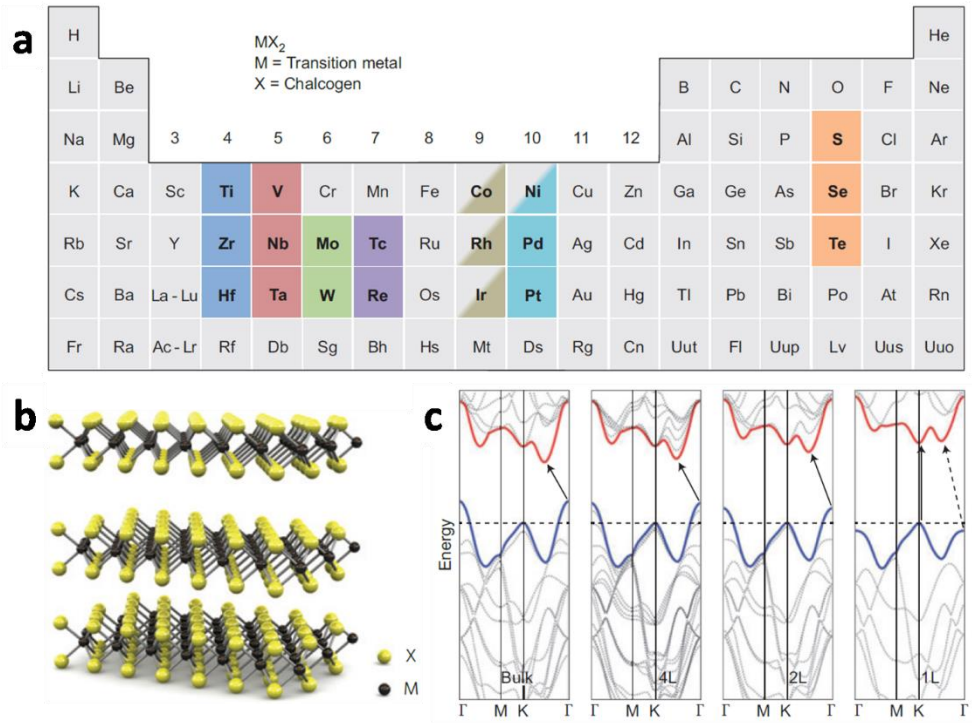

Figure 1- 3 Crystal structure of monolayer TMDs (a) All the possible transition metal elements and chalcogen elements in the periodic table that can crystallized as layered structures are highlighted, from Ref [29]; (b) Schematic representation of a typical MX_2 structure; (c) Electronic band structure of bulk, 4 layers (4L), 2L and monolayer MoS_2 from Ref [30].

It is appealing that most atomically thin TMDs show exotic properties with respect to their bulk counterparts[31,32] benefiting from the nature of anisotropic bonding (weak interlayer van der Waals forces and strong in-plane bonds)[33]. A representative semiconducting TMD, MoS_2, is considered as an outstanding candidate for optoelectronic devices[32] due to its indirect to direct bandgap transition[31] (when thin down to monolayer), thus resulting in an enhancement in the photoluminescence yield, and for atomically thin FET[34] because of the high on/off current ratios ($>10^5$)[35] and tunability in carrier type and concentration. It is also reported that MoS_2 can serve as a catalyst for hydrogen evolution reaction (HER) due to its catalytically active edge sites.[36] The electronic structure of TMDs is dominated by the transition metal coordination environment and its remaining (M^{4+}) d-electron after bonding with chalcogen.[29] The electronic properties of pristine

TMDs range from semiconductors (MoS_2, WS_2, $MoSe_2$ and WSe_2) to metallic (VS_2, NbS_2). Exotic behaviors in certain TMDs are also been explored such as superconductivity in $MoTe_2$[37], ferromagnetic ordering in VSe_2[38], and charge wave density in TaS_2[39], and so on.

1.1.4 Transition metal carbides

The recently discovered functionalized transitional metal carbides (MXenes, with formula of $M_{n+1}T_xC_n$, where M is the transitional metal and T refers to the functional group), provide new 2D building blocks, with potentially useful properties especially in electrical energy storage.[40] Yet extensive intrinsic defects and lacking of large area controllable synthesis method hindered investigation of their fundamental physical properties and applications in electronics.[41] More recently, it has been reported that large area 2D transition metal carbides (TMCs) crystals such as α-phase Mo_2C can be synthesized by chemical vapor deposition, as-grown high quality 2D α-Mo_2C show thickness dependent superconducting transition temperatures (T_C) up to 4K which makes it a promising candidate for studying the intrinsic properties of superconductivity in two dimensions (Fig. 1-4).[42]

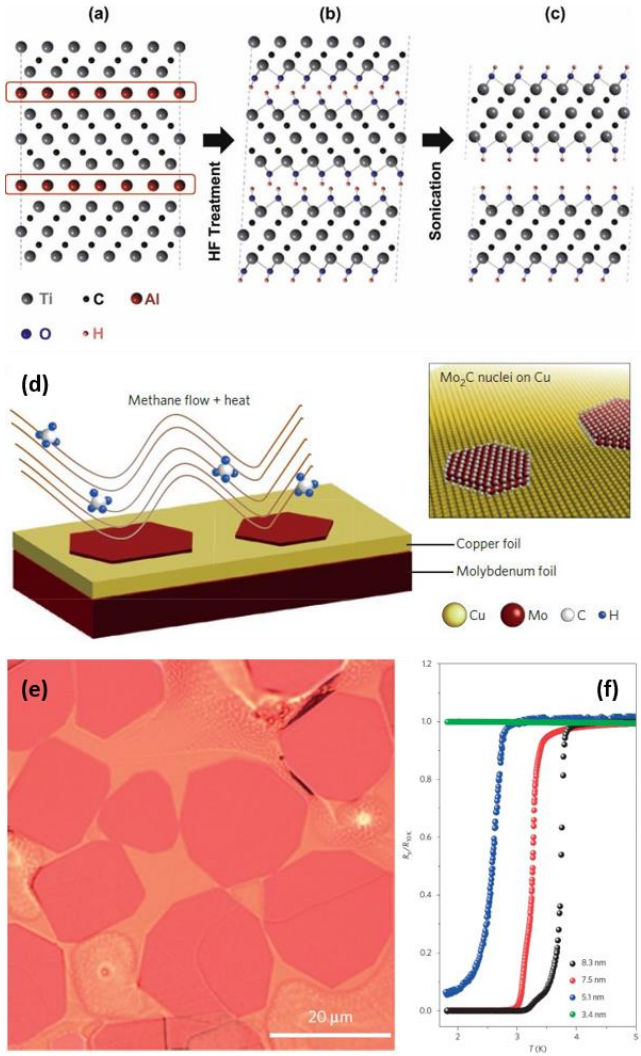

Figure 1- 4 (a)-(c) Schematics of the MXene (Ti_3AlC_2) crystal structure and related exfoliation process. The Al atoms was substituted as OH ions after etching by HF, sonication of the etched flakes in methanol results in hydrogen bonds breaking between layers then separation into thin sheets from Ref [43]; (d) schematics of CVD growth of 2D Mo_2C crystals from Ref [41]; (e)optical image of 2D Mo_2C grown on Cu, (f) Thickness dependence of superconductivity of 2D ultrathin Mo_2C crystals from Ref [42].

1.2 2D TMD-based Heterostacks/Alloys and Properties

1.2.1 Heterostacks by transition metal dichalcogenides

Above-mentioned van der Waal materials including conductive graphene, semiconducting TMDs, insulating BN and superconducting TMC can be integrated or assembled together into a multilayer stack (vertical heterostructures) or stitched as in-plane contact. The resulting "customer-made" designs provide an approach to novel properties and functionalities of these 2D materials, also called as van der Waal solids (Fig. 1-5). As an excellent vdW dielectric layer, BN has been proven to be a perfect substrate for graphene electronics with atomically flat interfaces, reduced impurity doping and chemically inactivity.[44] Exotic physical properties has been investigated since then such as Moiré superlattices in graphene/BN heterostacks induced Hofstadter's butterfly and fractal quantum Hall effect[45], enhanced light matter interactions in TMDs/graphene heterostacks[46]. Thanks to the weak interlayer vdW forces in 2D materials, arbitrary 2D layers could be vertically stacked with various orders or orientations simply by exfoliation-stacking technique.[47] By stacking WS_2 on graphene, unprecedented high current modulation at room temperature and high on/off ratio is obtained due to the coupling of tunneling and thermionic transport with respect to the barrier, with practical applications in flexible and transparent next generation devices.[48] Considering the limitation on controllability and scalability of the exfoliation-stacking technique, it is highly desired to produce targeted 2D heterostructures by direct synthesize method. Beyond the truth that scalable synthesizing individual 2D layers then transfer layer-by-layer to form heterostacks, one can improve to direct synthesize one 2D materials on another to avoid the inevitably interface contaminations and wrinkles from transfer process. Robinson *et al*. realized the direct and controllable synthesis of van der Waal solids based on graphene, hBN, MoS_2, and $WSe_2$with atomically sharp interface and precise orientation relations.[49] Besides that, TMDs on graphene,[50,51,52] TMDs on BN,[19,25,53], graphene/BN stacks[54] or in-plane heterostructures[55], TMDs on another TMDs,[56,57] graphene/TMC heterostructures,[58,59,60] are realized by controllable synthesis method with intriguing properties in electronics[19], optoelectronic[56,57], catalysis[51,60] and

superconductivity[58,59]. The growth mechanism, atomic registry and properties of metalorganic chemical vapor deposition grown WSe_2/BN are systematically studied in Chapter 3.

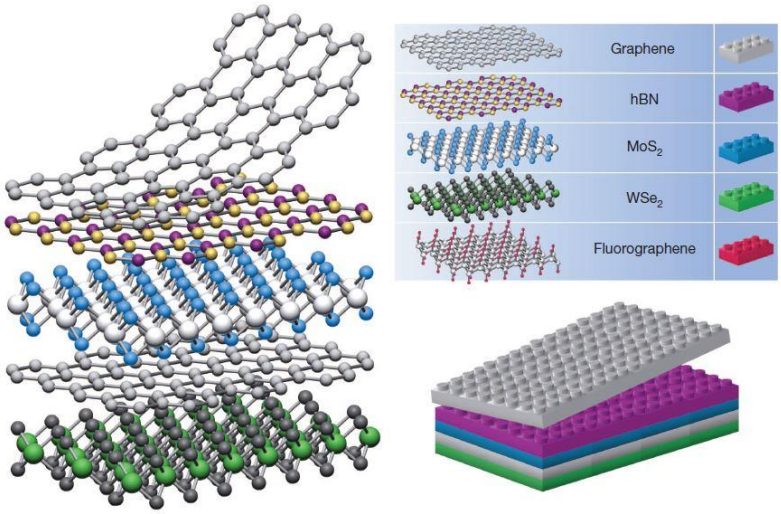

Figure 1- 5 Building van der Waals solids. arbitrary 2D layers could be vertically stacked by exfoliation-stacking technique or direct growth of one kind of 2D material on other from Ref [47].

After the experimental isolation of both 2D TMDs and TMCs, new fundamental challenges arise in regards of the possible doping or combination of both kinds of materials. TMC/TMD alloy structures are explored to exhibit intriguing properties for innovative applications (Fig. 1-6). One route to realize the TMD/TMC hybridization is direct carburization of 2D TMDs into chalcogenide-carbide alloys, such hybrids have shown great potential applications on the HER catalysis properties with hydrogen adsorption Gibbs free energy near zero due to the existence of Mo-S-C ternary bonds.[61,62] Zhao *et al*. reported a vertical aligned MoS_2/Mo_2C assembly acted as a binder-free hybrid catalyst own the low overpotential and low Tafel slope which is a result of metallic Mo_2C nanodomains dispersed at active edge sites of MoS_2.[61] Enhanced HER function on turnover frequency was also found in sulfur-decorated Mo_2C nanoparticles reported by Tang *et al*.[63] Recently Jeon *et al.* demonstrated an epitaxial Mo_2C/MoS_2 heterojunction platform with a small Schottky barrier height with low contact resistance, the metallic Mo_2C could serve as electrical

contacts to the semiconducting MoS_2.[64] Very recently, the synthesis of large-area monolayer TMCs by a CVD method was reported[65]. The as-grown materials are highly crystalline, and can be transferred to arbitrary substrates for sulfidation or selenization. Such hybrid structures with high-degree of crystallinity and atomically sharp interfaces are expected to exhibit novel properties for innovative applications. For example, in a lateral TMD/TMC heterojunction configuration, the metallic phases could serve as electrical contacts to the semiconducting disulfides.[64] In a vertically stacked geometry, the plasmonic mode generated from the metal carbide or byproduct graphene quantum dots may monitor the band structures or be coupled to the excitonic emission of the semiconducting phase.[66,67] A similar effect has been previously reported in gold decorated MoS_2.[68] It is expected to identify new physical phenomena in these systems that are either stable or metastable and determine the physical origins of these phenomena.

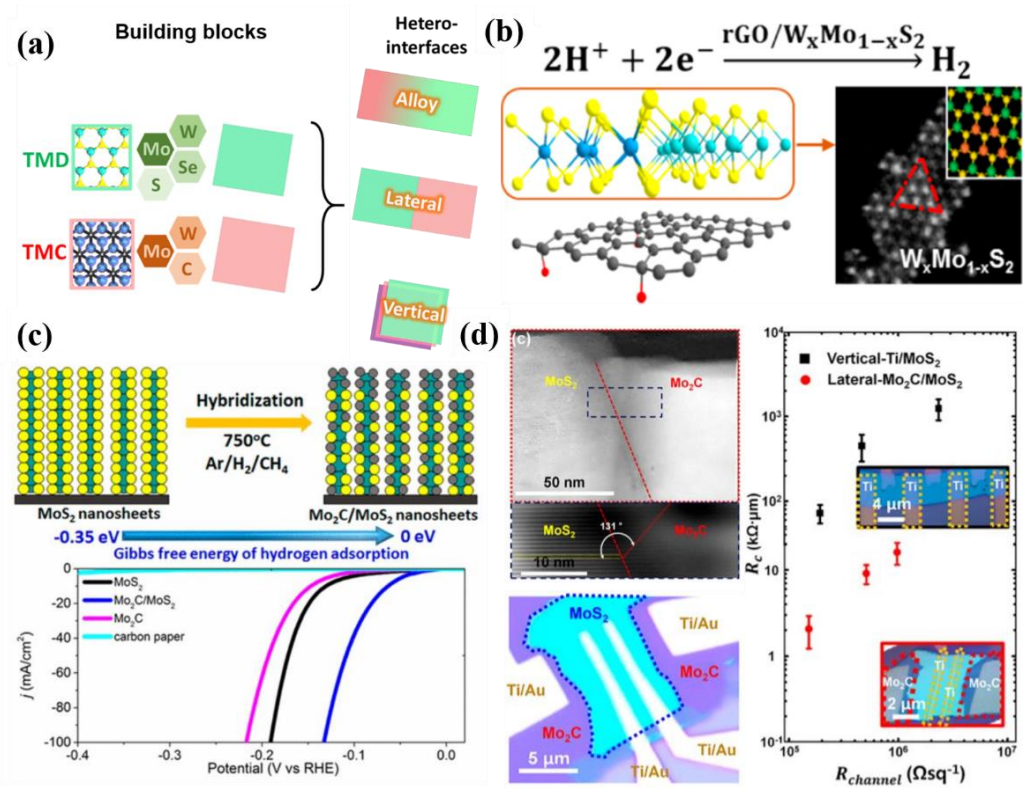

Figure 1- 6 (a) Vision of the proposed effort. TMDs and TMCs, will be blended in different compositions and configurations, in order to create novel alloys and heterostructures; (b) structure of $W_xMo_{1-x}S_2$/rGO nanosheets as effective hydrogen evolution reaction catalyst from Ref [69]; (c) Synthesis and hydrogen evolution reaction catalysis performance of alloyed Mo_2C/MoS_2 from Ref [61];

(d) the channel sheet resistance of top-contact Ti/MoS_2 (black) and lateral-contact Mo_2C/MoS_2 junction based FET devices (red) from Ref [64].

1.2.2 Alloys of transition metal dichalcogenides

Compared with other material engineering methods, such as chemical functionalization[70], alloying is non-volatilely able to tailor the material's band gap.[71] With a designed "pattern regrowth" method, graphene and BN alloy (some literature also called as BCN alloys) is realized as ultrathin circuit component.[72,73] Many studies show that it is possible to engineer catalytic[74,75,76], electronic[77,78], and optical[79,80] properties by alloying 2D layered TMDs (Fig. 1-7), especially commonly studied TMDs such as MoS_2, $MoSe_2$, WS_2 and WSe_2, allowing completed range of alloy compositions.[80,81] Engineering the performance of layered TMDs-based electronic devices can be achieved through alloying by regulating the positions of valence band and conduction band.[78] The tunable band gaps in alloys can excite cut-off with wide spectrum of detection wavelengths, which hold great promise in optoelectronics such as photodetecting devices.[79,80] It is expected that even greater flexibility and manipulation of the alloy's properties could be achieved.

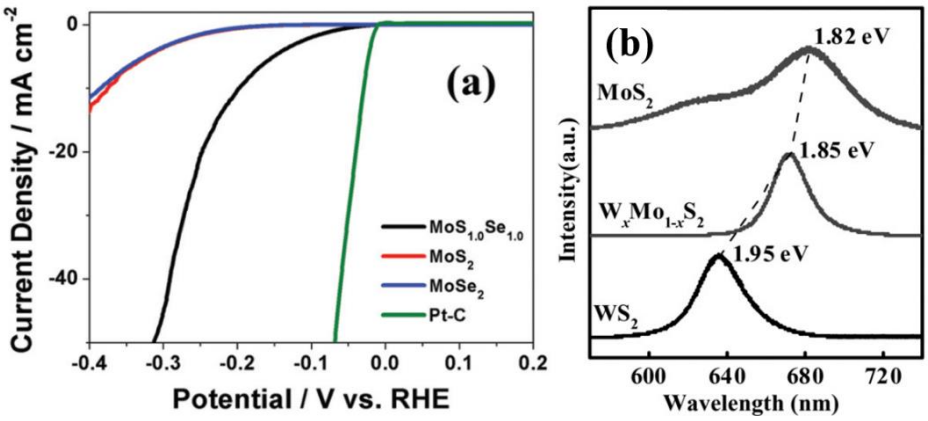

Figure 1- 7 (a) Hydrogen evolution reaction catalysis performance of alloyed $MoS_{2(1-x)}Se_{2x}$ from Ref [82]; (b) Tunable PL responses from monolayer $W_xMo_{1-x}S_2$ and their pristine counterparts from Ref [83].

To date, 2D superconductivity became an emergent scientific frontier currently addressing a number of unanswered questions, such as the disparate evolution of the superconducting transition temperature in the different compounds as a function of the layer numbers.[84] In the two-dimensional limit superconductivity is found to exhibit unique properties: for example, monolayer FeSe grown on $SrTiO_3$, is claimed to display superconductivity at temperatures as high as T_c=100 K[85,86] in contrast to the bulk value T_c=8 K. Ionic liquid induced superconductivity on the surface of TMDs[87] such as MoS_2 as well as the intrinsic superconductivity in exfoliated metallic TMDs (e.g. $NbSe_2$) display a remarkable resilience with respect to external magnetic fields at in-plane direction.[88] In few layers or in monolayer 1*H*-TaS_2 the superconducting upper critical fields are found to surpass the Pauli-limiting field by a factor exceeding six.[84] The spin-singlet Cooper pairing would occur among carriers at the *K* and *K*' valleys having opposite spins which is evidence for the so-called Ising-paired state. In the monolayer limit, the functional form of the spin-orbit coupling is predicted to orient the orbital moments and hence the coupled spins (of the quasiparticles), perpendicularly to the superconducting planes which renormalizes the Pauli limiting field. Although, this scenario is not applicable to few layered crystals, these still display remarkably high upper critical fields for reasons that remain to be understood. 2D superconductivity became an emergent scientific frontier currently addressing a number of unanswered questions, such as the disparate evolution of the superconducting transition temperature in the different compounds as a function of the number of layers.[84]

Emergent superconductivity is found in 1T'-MoS_2 monolayers with upper critical field beyond Pauli paramagnetic limit, through chemical exfoliation from bulk 2H-phase.[89] In the type-II Weyl semimetallic candidate $MoTe_2$, T_c can be enhanced either through sulfur doping which induces a phase transition (from 1T' to T_d (monoclinic to orthorhombic) phase)[90], which is claimed

to enhance the electron-phonon coupling[91], or through exfoliation down to the monolayer limit that is believed to stabilize the T_d phase at room temperature.[92] Multilayer $W_xMo_{1-x}C_yS_2$ were realized by mixing, oxidizing and sulfurizing mixtures of Mo and WC at high temperatures (800-1100 °C) by Terrones *et al.* at 2000.[93,94] The obtained multilayer systems exhibit superconducting behavior. The different phases in molybdenum carbide display distinct superconducting properties which opens up the possibility of manipulating the performance of the carbide system via phase transitions such as alloying or formation of heterostacks with transition metal disulfide. Studies of molybdenum carbide/ disulfide heterostack/alloy structures and properties are discussed in Chapter 4.

1.2.3 Doping in transition metal dichalcogenides

Controllable and non-volatile tailoring of the desired properties of TMDs can be realized by substitutional doping,[95] where substituting foreign atoms engineer the materials also called as defect engineering.[96] Taking into account introducing a foreign atom substitute in a crystal lattice, the atom/ion relative size, valence and electronegativity are all crucial factors tailoring the resulting properties.[96] Superior than other engineering methods such as chemical functionalization,[70] which mainly relies on the electron transfer between TMDs and adsorbed organic species, substitutional doping is able to controllably tailor both the material's band gap and crystalline structure, as demonstrated theoretically[71] and experimentally[78,79] (Fig. 1-8). New functionalities including emerging spin-orbit anisotropies, thermal transport anisotropies[97] and the rising of magnetic order[98], have also been explored for doped TMDs. The approach used to dope TMDs is highly dependent on the elements that could be introduced into the crystalline lattice. Transitional metal disulfide/diselenide or molybdenum/tungsten dichalcogenides based doped materials were widely

investigated for adjustable optical bandgaps at full-range composition variations,[80,99] substitutional cation doping also drastically alters the electronic structure of the TMDs,[100] such as degenerated n-type transport by rhenium doping[101] and emergence of p-branch by niobium dopants[102], tantalum can also substitute the metal cation in TMDs in order to achieve a p-type electronic behavior.[103,104]

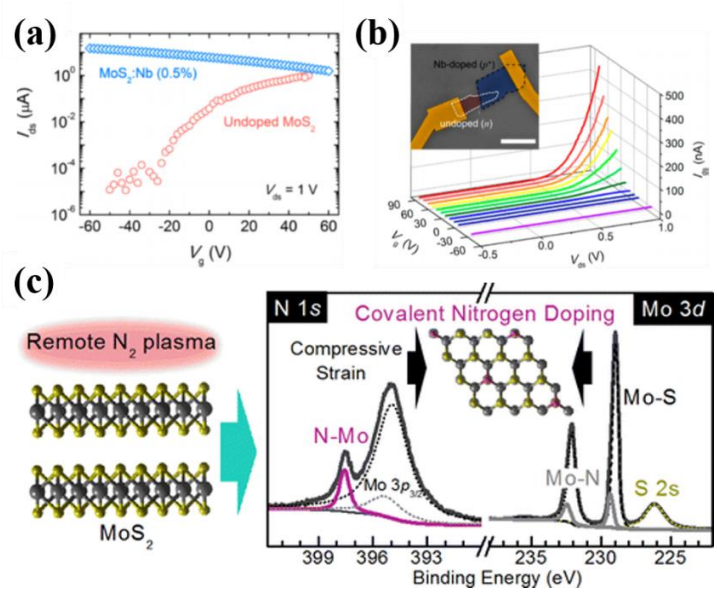

Figure 1- 8 (a) A rectification characteristic of p−n junction built by van der Waals pristine/Nb-doped MoS_2 stacked flakes; (b) I−V curves of the stacked p-n junction at variable applied voltages from Ref [104]. (c) Nitrogen doped MoS_2 by N_2 plasma treatment and induced compression strain in the lattice from Ref [105].

In addition, chalcogen (anion) doping could achieve stable and controllable tailoring of TMDs. A p-type doping behavior can also be obtained or enhanced by introducing substitutional phosphorus in MoS_2-based field effect transistors[106], as well as through oxygen molecule physisorption[107]. In a recent report, covalent nitrogen doping resulted in variations of the MoS_2 electronic structure.[105] Reversible optical and electronic properties of hydrogenated $MoSe_2$ were realized by simply treat monolayers with hydrogen plasma.[108] These studies enlighten our exploration on anion doping of carbon into TMDs via plasma-assisted method,[109] which will be discussed in Chapter 5.

Encouragingly, magnetic doping at the intrinsic paramagnetic TMDs[110] could also be achieved by substitutional doping as reported by both theoretical and experimental studies. Ferromagnetism in 2D semiconducting systems is an astonishing property that promotes the fundamental studies of the spin behavior at low dimensions and envisions new gate-modulated spintronic applications—exploits both the charge- and the spin- based data manipulation and storage.[111,112] 2D TMDs based diluted magnetic semiconductors (DMSs) have recently been investigated through incorporation of magnetic transition metal atoms such as V[113], Ni[114], Co[115] and Mn[116] within lattices, room-temperature ferromagnetism could even be preserved in V-doped WSe_2,[113] and V-decorated $MoTe_2$.[117] Correlations among the doping concentration, the emergent ferromagnetic feature and other functionalities (electronic and optoelectronic) in these materials have not been well understood, knowledge of which is in great demand for new opportunities as novel magnetoelectric and magneto-optic applications.[118,119] We successfully synthesized high quality V-doped WS_2 monolayers with variable doping levels, an intrinsic ferromagnetic state at room temperature in monolayer moderate V-doped WS_2 (optimal at 2%) is demonstrated detailed in Chapter 6.

1.3 Assembly methods for TMD based heterostacks and alloys

1.3.1 Assembly of TMD Heterostacks

Similar to synthetic routes of pristine 2D materials, the assembly method of heterostacks of 2D material also can be classified as bottom-up and top-down methods.[120] Mimicking the exfoliation of graphene by scotch tape, other 2D blocks including pristine and doped TMDs could

readily serve as building blocks by mechanical peeling apart from their parent counterparts. Reliable blind[121] or deterministic[122] transfer methods are used for stacking these materials in arbitrary orders to realize unique functions. It is expected to get clean and atomically sharp interfaces due to the free-dangling bonds for layered materials after stacking, while the defects in the material and transfer process would inevitably introduce wrinkles or contaminations in the heterostack assemblies.[122,123] The atomic structure of the defects within the interface can affect or deteriorate the physical, chemical and electronic properties of vdW heterostacks as well as the fabrication and functionality of devices.[47] Moreover, manual transfer cannot precisely regulate the stacking orientation of the two nanosheets. To address this problem, scalable and controllable synthesis method is imperative to obtain vdW heterostructure with a clean interface[49] benefitting from elimination of postgrowth handling.

Scalable and controllable CVD and powder vaporization (PV) synthesis of TMDs on graphene was firstly[124] and then extensively[50,125,126] investigated due to the unique properties on the heterostacks such as PL quenching effect in TMDs/graphene vdW heterostructures[50,125] (Fig. 1-9). Previous works[19,22,127,128] have also reported TMDs/hBN heterostructures synthesized by CVD process, some of them[22, 128] demonstrated TMDs show preferred growth orientation on hBN surface while the others did not, which may related to the hBN surface defect conditions and synthesis methods. Directly epitaxial growth of TMDs on another TMDs are also widely studied as in-plane heterojunctions with atomically sharp interfaces,[129,130,131] or as out-of-plane heterostacks for novel physical phenomena such resonant tunneling effect in an atomically thin MoS_2/WSe_2 stack with negative differential resistance characteristics,[56] strong interlayer exitonic transition at WS_2/MoS_2 vertical heterostacks due to type II band alignment,[129] and Moiré or strain engineering of electronic structures of TMDs by epitaxy growth.[57] Although enormous devotions are applied to the CVD

synthesis of TMD-based heterostacks, the fundamental epitaxial mechanism are not well understand, such as the orientation epitaxial relationship would exist or not between different process and the interface interferences with vdW bonding. Another obstacle for atomically sharp interfaces heterostack formation comes from the sequences for materials synthesis, the epitaxial substrate materials must hold integrity when experiencing the harsh CVD process for synthesizing another material, such as high temperature or chemical reactive species incorporation. Subtle fluctuation in TMD(A)/TMD(B) heterostack synthesis process may lead to totally different compositions, such as diffused alloys instead of clear stack interfaces, the instabilities still need further discussion. Other heterostack assembly methods are also developed for specific cases in applications such as molecular beam epitaxy (MBE),[38,132] solution-based method[69,133].

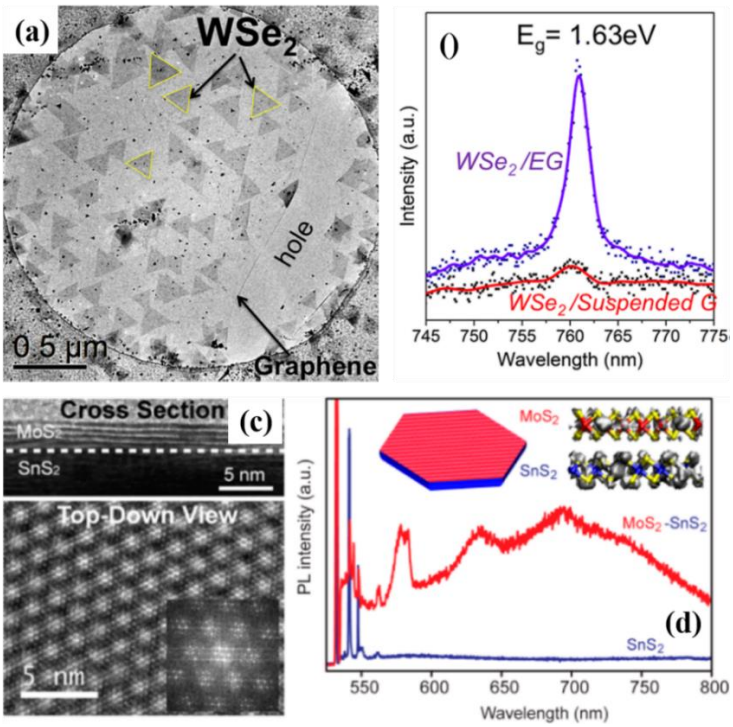

Figure 1- 9 (a) TEM image of freestanding vertical heterostructure of WSe_2/graphene; (b) PL responses from freestanding WSe_2/graphene films and substrate coupled WSe_2/EG heterostructures indicates drastic PL emission quenching when suspending from Ref [59]; (c) TEM analyses of MoS_2/SnS_2 in both cross-sectional direction and planar view, the Moire patterns at planar view shows the lattice and angle mismatch between MoS_2 and SnS_2 during epitaxy; (d) PL spectra of pristine SnS_2 (blue) and epitaxial MoS_2/SnS_2 heterostacks (red) from Ref [57].

1.3.2 Synthesis methods of alloying/doping in TMDs

Alloying and doping are promising methods to enable the novel physical phenomena and functionalities in TMDs.[134] Almost entire family of transition metals in periodic table has been considered as alloying/doping species by density functional theory (DFT) calculations[134,135,136] or already experimental realized to date, these elements including cation elements Re,[101] Nb,[102] Ta,[103,104] Mn,[137] Fe,[138] Co[115,139] and Au[140], and anion elements N,[105] P,[106] H[108], C[109] and O[141]. The doping methods vary from physical vapor deposition, solution-based synthesis, chemical vapor transport, powder vaporization to chemical vapor deposition. Each method owns its advantages and drawbacks which could be compensated by optimizing the process or combination of methods.

Solution-based synthesis method for 2D materials nanostructures have advantages in scalable and high yielding of high surface area materials, low temperature compatibility which are desired for catalysis performance. Fluorinated hBN are realized in a solvothermal solution-based environment with fluorinating agent, the resulting materials behaves as a magnetic semiconductor comparing the pristine insulating BN nanosheets,[142] Alloys of $Mo_xW_{1-x}Se_2$ and $WS_{2y}Se_{2(1-y)}$ colloidal few layers were reported by Sun *et al.*[143] exhibiting full spectrum of composition ranges in terms of cation and anion. The alloyed materials show modulated bandgaps, which can be adjusted between 1.51 and 1.93 eV which are promising for optical applications. Hydrothermal synthesis of transition metal doped TMDs nanosheets are also widely studied such as Cu-doped MoS_2[144] and V-doped MoS_2[145,146] sheets, the electronic structure of deliberately doped semiconducting MoS_2 will significantly monitored for tunable optical and electronic properties, energy storage properties[146] and even emergence of ferromagnetism[144].

Physical vapor deposition (PVD) method is sophisticated technique to produce alloyed metal or thin film coatings for various applications,[147] and has been extended as a reliable way to synthesis transition metal dichalcogenides.[148] The growth of $MoS_{2(1-x)}Se_{2x}$ monolayer alloys with controllable edge terminations and morphology were reported by Feng *et al*.[149] PVD methods are also applied for alloyed metal seed coatings for further sulfurization (thin film convection),[148] these structures are used to understand the growth mechanism of TMDs, and the obtained vertically aligned alloyed nanosheets are readily as HER catalysis electrodes.[150]

Chemical vapor transport (CVT) reaction is most adopted as a process for crystallization of TMD purified crystals or alloyed/doped TMD crystals.[151] The volatile derivatives (elemental precursor) were sealed and located at the hotter side of tube furnace with a temperature gradient, migrating via a transport agent, and slowly convert to stoichiometric crystals at the cooler end. The as grown crystals endow high degree of crystallinity, the alloyed/ doped elements are uniformly dispersed with high spatial homogeneity in the crystals as long as the designed reaction follows the thermodynamic rules as an exothermic process.[152] Random distribution of anion in CVT produced MS_xSe_{2-x} (M= Mo, W) alloyed crystals are reported by Nguyen et al. with detailed characterizations in structures and composition and readily for exfoliation for further applications.[153] It is also demonstrated that nickel doping in WSe_2 crystals[114] by CVT process can introduce ferromagnetic ordering in the lattice, and V-doped MoS_2[154] crystals with various doping concentrations exhibit tunable semimetal character which is suitable as effective HER catalyst.

Comparing with chemical vapor transport (or solid-state reaction) growth of bulk alloy and then following mechanical or chemical exfoliation for obtaining 2D layered materials, powder vaporization and CVD are lauded as most flexible and explored methods for doping or alloying

foreign elements (no matter cation or anion) into TMD materials, with controllable morphology and scalable crystal size, advantages in short time scales, lower temperatures and flexible precursor choices.[155] While the more kinetics-driven CVD processes may results in different synthetic morphologies of alloyed materials, such as homogeneous alloys,[77,100] non-uniform alloys with composition gradient,[97, 156] and phase-segregated heterostructures.[131] These methods can be included in two categories. First is multiple-steps preparation method that to use the pristine materials as a platform, treated with post doping techniques such as ion exchange[157], diffusion[61] or decoration[63,117]. These methods show great flexibilities from pristine counterparts to induced species which opens a pathway to tailor the intrinsic properties of the 2D materials, by strain engineering and structural engineering. In two-step synthesis MoS_2-WS_2 heterostructures, 2D heterostack or 1D lateral heterojunction can be selectively generated by tuning the process temperature.[129] On the other hand, one-step synthesis processes are extensively investigated for controllable and reliable process which show more benefits for practical applications. Methods such metal convection (PVD of metal seedings followed by sulfidation)[103, 148] are feasible for alloying and doping. By careful selection of dopant precursor and optimization of growth parameters, one-step CVD process are also applied for simultaneously synthesis of pristine/doped/alloyed TMD materials which are controllable and readily study the effect of alloying/doping.

1.4 Objectives and Organization of the Thesis

Chapter 1 provides the literature reviews and current research statues of 2D materials beyond graphene, including transition metal dichalcogenides and their derivatives, such as

heterostacks and alloys. The synthesis methods and properties of the TMD-based heterostacks and alloys are also discussed.

Chapter 2 summarize the experimental procedures and methods including material synthesis methods, characterization and property performance test.

The research subjects (Chapter 3-6) mentioned in this thesis are listed as follow:

(1) Defect-controlled nucleation and orientation of WSe_2 on hBN——a route to single crystal epitaxial monolayers. This study provides a tentative solution to ultimate problem of single crystal growth of TMD monolayers, using boron nitride polarized dangling bonds free surface as vdW epitaxial growth substrate. (Chapter 3)

(2) Superconductivity enhancement of molybdenum carbide via the formation of carbide/disulfide heterostacks. High quality superconducting α-phase molybdenum carbide (Mo_2C) flakes were used to engineer 2D molybdenum carbide/disulfide heterostructures. This approach induced controlled successive phase transitions between various superconducting carbide phases, which led to consecutive increases in T_C. (Chapter 4)

(3) Carbon doping of WS_2 monolayers: Band gap reduction and p-type doping transport. By assistance of plasma, we successful introduce carbon-hydrogen species into WS_2 monolayers for the first time. The carbon-doped WS_2 monolayers exhibit tunable optical and electronic properties, as revealed by both experimental measurements and theoretical simulations. (Chapter 5)

(4) One-step synthesis of monolayer vanadium-doped tungsten disulfide: an emerging room-temperature diluted magnetic semiconductor. Vanadium-doped tungsten disulfide (V-WS_2) monolayers with a wide spectrum of vanadium concentrations were synthesized by a reliable single-step powder vaporization method. Ferromagnetic ordering is induced in monolayer V-WS_2 at room temperature and reaches optimal at ~2%at. (Chapter 6)

Finally, chapter 7 contains the conclusions and future work of this thesis.

1.5 Reference

1. Novoselov, K. S.; Geim, A. K.; Morozov, S. V.; Jiang, D.; Zhang, Y.; Dubonos, S. V.; Grigorieva, I. V.; Firsov, A. A., Electric field effect in atomically thin carbon films. *science* **2004,** *306* (5696), 666-669.

2. Lee, C.; Wei, X.; Kysar, J. W.; Hone, J., Measurement of the elastic properties and intrinsic strength of monolayer graphene. *science* **2008,** *321* (5887), 385-388.

3. Kuzmenko, A.; Van Heumen, E.; Carbone, F.; Van Der Marel, D., Universal optical conductance of graphite. *Physical review letters* **2008,** *100* (11), 117401.

4. Xu, Y.; Bai, H.; Lu, G.; Li, C.; Shi, G., Flexible graphene films via the filtration of water-soluble noncovalent functionalized graphene sheets. *Journal of the American Chemical Society* **2008,** *130* (18), 5856-5857.

5. Li, X.; Tao, L.; Chen, Z.; Fang, H.; Li, X.; Wang, X.; Xu, J.-B.; Zhu, H., Graphene and related two-dimensional materials: Structure-property relationships for electronics and optoelectronics. *Applied Physics Reviews* **2017,** *4* (2), 021306.

6. Bonaccorso, F.; Sun, Z.; Hasan, T.; Ferrari, A., Graphene photonics and optoelectronics.

Nature photonics **2010,** *4* (9), 611.

7. Balog, R.; Jørgensen, B.; Nilsson, L.; Andersen, M.; Rienks, E.; Bianchi, M.; Fanetti, M.; Lægsgaard, E.; Baraldi, A.; Lizzit, S., Bandgap opening in graphene induced by patterned hydrogen adsorption. *Nature materials* **2010,** *9* (4), 315.

8. Wang, H.; Maiyalagan, T.; Wang, X., Review on recent progress in nitrogen-doped graphene: synthesis, characterization, and its potential applications. *Acs Catalysis* **2012,** *2* (5), 781-794.

9. Tang, Y.-B.; Yin, L.-C.; Yang, Y.; Bo, X.-H.; Cao, Y.-L.; Wang, H.-E.; Zhang, W.-J.; Bello, I.; Lee, S.-T.; Cheng, H.-M., Tunable band gaps and p-type transport properties of boron-doped graphenes by controllable ion doping using reactive microwave plasma. *Acs Nano* **2012,** *6* (3), 1970-1978.

10. Gui, G.; Li, J.; Zhong, J., Band structure engineering of graphene by strain: first-principles calculations. *Physical Review B* **2008,** *78* (7), 075435.

11. Cao, Y.; Fatemi, V.; Fang, S.; Watanabe, K.; Taniguchi, T.; Kaxiras, E.; Jarillo-Herrero, P., Unconventional superconductivity in magic-angle graphene superlattices. *Nature* **2018,** *556* (7699), 43.

12. Rao, C. e. N. e. R.; Sood, A. e. K.; Subrahmanyam, K. e. S.; Govindaraj, A., Graphene: the new two-dimensional nanomaterial. *Angewandte Chemie International Edition* **2009,** *48* (42), 7752-7777.

13. Miró, P.; Audiffred, M.; Heine, T., An atlas of two-dimensional materials. *Chemical Society Reviews* **2014,** *43* (18), 6537-6554.

14. Gibb, A.; Alem, N.; Zettl, A., Low pressure chemical vapor deposition synthesis of hexagonal boron nitride on polycrystalline metal foils. *physica status solidi (b)* **2013,** *250* (12), 2727-2731.

15. Iskandar, F.; Kim, S.-G.; Nandiyanto, A. B. D.; Kaihatsu, Y.; Ogi, T.; Okuyama, K., Direct synthesis of hBN/MWCNT composite particles using spray pyrolysis. *Journal of Alloys and Compounds* **2009,** *471* (1-2), 166-171.

16. Britnell, L.; Gorbachev, R. V.; Jalil, R.; Belle, B. D.; Schedin, F.; Katsnelson, M. I.; Eaves, L.; Morozov, S. V.; Mayorov, A. S.; Peres, N. M., Electron tunneling through ultrathin boron nitride crystalline barriers. *Nano letters* **2012,** *12* (3), 1707-1710.

17. Dean, C.; Young, A.; Cadden-Zimansky, P.; Wang, L.; Ren, H.; Watanabe, K.; Taniguchi, T.; Kim, P.; Hone, J.; Shepard, K., Multicomponent fractional quantum Hall effect in graphene. *Nature Physics* **2011,** *7* (9), 693-696.

18. Dean, C. R.; Young, A. F.; Meric, I.; Lee, C.; Wang, L.; Sorgenfrei, S.; Watanabe, K.; Taniguchi, T.; Kim, P.; Shepard, K., Boron nitride substrates for high-quality graphene electronics. *Nature nanotechnology* **2010,** *5* (10), 722-726.

19. Fu, L.; Sun, Y.; Wu, N.; Mendes, R. G.; Chen, L.; Xu, Z.; Zhang, T.; Rümmeli, M. H.; Rellinghaus, B.; Pohl, D., Direct Growth of MoS_2/h-BN Heterostructures via a Sulfide-Resistant Alloy. *ACS nano* **2016,** *10* (2), 2063-2070.

20. Wan, Y.; Zhang, H.; Wang, W.; Sheng, B.; Zhang, K.; Wang, Y.; Song, Q.; Mao, N.; Li, Y.; Wang, X., Origin of improved optical quality of monolayer molybdenum disulfide grown on hexagonal boron nitride substrate. *Small* **2016,** *12* (2), 198-203.

21. Cui, X.; Lee, G.-H.; Kim, Y. D.; Arefe, G.; Huang, P. Y.; Lee, C.-H.; Chenet, D. A.; Zhang, X.; Wang, L.; Ye, F., Multi-terminal transport measurements of MoS_2 using a van der Waals heterostructure device platform. *Nature nanotechnology* **2015,** *10* (6), 534-540.

22. Yan, A.; Velasco Jr, J.; Kahn, S.; Watanabe, K.; Taniguchi, T.; Wang, F.; Crommie, M. F.; Zettl, A., Direct growth of single-and few-layer MoS_2 on h-BN with preferred relative rotation angles. *Nano letters* **2015,** *15* (10), 6324-6331.

23. Chen, J.-H.; Jang, C.; Xiao, S.; Ishigami, M.; Fuhrer, M. S., Intrinsic and extrinsic performance limits of graphene devices on SiO_2. *Nature nanotechnology* **2008,** *3* (4), 206-209.

24. Zhang, X.; Zhang, F.; Wang, Y.; Schulman, D. S.; Zhang, T.; Bansal, A.; Alem, N.; Das, S.; Crespi, V. H.; Terrones, M., Defect-Controlled Nucleation and Orientation of WSe_2 on hBN: A Route to Single-Crystal Epitaxial Monolayers. *ACS nano* **2019,** *13* (3), 3341-3352.

25. Zhang, F.; Wang, Y.; Erb, C.; Wang, K.; Moradifar, P.; Crespi, V. H.; Alem, N., Full orientation control of epitaxial MoS_2 on hBN assisted by substrate defects. *Physical Review B* **2019,** *99* (15), 155430.

26. Zhou, W.; Zou, X.; Najmaei, S.; Liu, Z.; Shi, Y.; Kong, J.; Lou, J.; Ajayan, P. M.; Yakobson, B. I.; Idrobo, J.-C., Intrinsic structural defects in monolayer molybdenum disulfide. *Nano letters* **2013,** *13* (6), 2615-2622.

27. Kang, K.; Xie, S.; Huang, L.; Han, Y.; Huang, P. Y.; Mak, K. F.; Kim, C.-J.; Muller, D.; Park, J., High-mobility three-atom-thick semiconducting films with wafer-scale homogeneity. *Nature* **2015,** *520* (7549), 656.

28. Cui, X.; Lee, G.-H.; Kim, Y. D.; Arefe, G.; Huang, P. Y.; Lee, C.-H.; Chenet, D. A.; Zhang, X.; Wang, L.; Ye, F., Multi-terminal transport measurements of MoS_2 using a van der Waals heterostructure device platform. *Nature nanotechnology* **2015,** *10* (6), 534.

29. Chhowalla, M.; Shin, H. S.; Eda, G.; Li, L.-J.; Loh, K. P.; Zhang, H., The chemistry of two-dimensional layered transition metal dichalcogenide nanosheets. *Nature chemistry* **2013,** *5* (4), 263.

30. Wang, Q. H.; Kalantar-Zadeh, K.; Kis, A.; Coleman, J. N.; Strano, M. S., Electronics and optoelectronics of two-dimensional transition metal dichalcogenides. *Nature nanotechnology* **2012,** *7* (11), 699.

31. Mak, K. F.; Lee, C.; Hone, J.; Shan, J.; Heinz, T. F., Atomically thin MoS_2: a new direct-gap semiconductor. *Physical Review Letters* **2010,** *105* (13), 136805.

32. Wang, Q. H.; Kalantar-Zadeh, K.; Kis, A.; Coleman, J. N.; Strano, M. S., Electronics and optoelectronics of two-dimensional transition metal dichalcogenides. *Nature nanotechnology* **2012,** *7* (11), 699-712.

33. Verble, J.; Wietling, T.; Reed, P., Rigid-layer lattice vibrations and van der waals bonding in hexagonal MoS_2. *Solid State Communications* **1972,** *11* (8), 941-944.

34. Kim, S.; Konar, A.; Hwang, W.-S.; Lee, J. H.; Lee, J.; Yang, J.; Jung, C.; Kim, H.; Yoo, J.-B.; Choi, J.-Y., High-mobility and low-power thin-film transistors based on multilayer MoS_2 crystals. *Nature communications* **2012,** *3*, 1011.

35. Radisavljevic, B.; Radenovic, A.; Brivio, J.; Giacometti, i. V.; Kis, A., Single-layer MoS_2 transistors. *Nature nanotechnology* **2011,** *6* (3), 147-150.

36. Wang, H.; Lu, Z.; Xu, S.; Kong, D.; Cha, J. J.; Zheng, G.; Hsu, P.-C.; Yan, K.; Bradshaw, D.; Prinz, F. B., Electrochemical tuning of vertically aligned MoS_2 nanofilms and its application in improving hydrogen evolution reaction. *Proceedings of the National Academy of Sciences* **2013,** *110* (49), 19701-19706.

37. Qi, Y.; Naumov, P. G.; Ali, M. N.; Rajamathi, C. R.; Schnelle, W.; Barkalov, O.; Hanfland, M.; Wu, S.-C.; Shekhar, C.; Sun, Y., Superconductivity in Weyl semimetal candidate $MoTe_2$. *Nature communications* **2016,** *7*, 11038.

38. Bonilla, M.; Kolekar, S.; Ma, Y.; Diaz, H. C.; Kalappattil, V.; Das, R.; Eggers, T.; Gutierrez, H. R.; Phan, M.-H.; Batzill, M., Strong room-temperature ferromagnetism in VSe_2 monolayers on van der Waals substrates. *Nature nanotechnology* **2018,** *13* (4), 289.

39. Scruby, C.; Williams, P.; Parry, G., The role of charge density waves in structural transformations of 1T TaS_2. *Philosophical Magazine* **1975,** *31* (2), 255-274.

40. Halim, J.; Kota, S.; Lukatskaya, M. R.; Naguib, M.; Zhao, M. Q.; Moon, E. J.; Pitock, J.; Nanda, J.; May, S. J.; Gogotsi, Y., Synthesis and characterization of 2D molybdenum carbide

(MXene). *Advanced Functional Materials* **2016,** *26* (18), 3118-3127.

41. Gogotsi, Y., Chemical vapour deposition: transition metal carbides go 2D. *Nature materials* **2015,** *14* (11).

42. Xu, C.; Wang, L.; Liu, Z.; Chen, L.; Guo, J.; Kang, N.; Ma, X.-L.; Cheng, H.-M.; Ren, W., Large-area high-quality 2D ultrathin Mo_2C superconducting crystals. *Nature materials* **2015,** *14* (11), 1135.

43. Naguib, M.; Kurtoglu, M.; Presser, V.; Lu, J.; Niu, J.; Heon, M.; Hultman, L.; Gogotsi, Y.; Barsoum, M. W., Two-dimensional nanocrystals produced by exfoliation of Ti_3AlC_2. *Advanced Materials* **2011,** *23* (37), 4248-4253.

44. Dean, C. R.; Young, A. F.; Meric, I.; Lee, C.; Wang, L.; Sorgenfrei, S.; Watanabe, K.; Taniguchi, T.; Kim, P.; Shepard, K. L., Boron nitride substrates for high-quality graphene electronics. *Nature nanotechnology* **2010,** *5* (10), 722.

45. Dean, C. R.; Wang, L.; Maher, P.; Forsythe, C.; Ghahari, F.; Gao, Y.; Katoch, J.; Ishigami, M.; Moon, P.; Koshino, M., Hofstadter's butterfly and the fractal quantum Hall effect in moiré superlattices. *Nature* **2013,** *497* (7451), 598.

46. Britnell, L.; Ribeiro, R.; Eckmann, A.; Jalil, R.; Belle, B.; Mishchenko, A.; Kim, Y.-J.; Gorbachev, R.; Georgiou, T.; Morozov, S., Strong light-matter interactions in heterostructures of atomically thin films. *Science* **2013,** *340* (6138), 1311-1314.

47. Geim, A. K.; Grigorieva, I. V., Van der Waals heterostructures. *Nature* **2013,** *499* (7459), 419.

48. Georgiou, T.; Jalil, R.; Belle, B. D.; Britnell, L.; Gorbachev, R. V.; Morozov, S. V.; Kim, Y.-J.; Gholinia, A.; Haigh, S. J.; Makarovsky, O., Vertical field-effect transistor based on graphene–WS_2 heterostructures for flexible and transparent electronics. *Nature nanotechnology* **2013,** *8* (2), 100.

49. Lin, Y.-C.; Lu, N.; Perea-Lopez, N.; Li, J.; Lin, Z.; Peng, X.; Lee, C. H.; Sun, C.; Calderin, L.; Browning, P. N., Direct synthesis of van der Waals solids. *Acs Nano* **2014,** *8* (4), 3715-3723.

50. Azizi, A.; Eichfeld, S.; Geschwind, G.; Zhang, K.; Jiang, B.; Mukherjee, D.; Hossain, L.; Piasecki, A. F.; Kabius, B.; Robinson, J. A., Freestanding van der Waals heterostructures of graphene and transition metal dichalcogenides. *ACS nano* **2015,** *9* (5), 4882-4890.

51. Biroju, R. K.; Das, D.; Sharma, R.; Pal, S.; Mawlong, L. P.; Bhorkar, K.; Giri, P.; Singh, A. K.; Narayanan, T. N., Hydrogen evolution reaction activity of graphene–MoS_2 van der Waals heterostructures. *ACS Energy Letters* **2017,** *2* (6), 1355-1361.

52. Gao, T.; Song, X.; Du, H.; Nie, Y.; Chen, Y.; Ji, Q.; Sun, J.; Yang, Y.; Zhang, Y.; Liu, Z., Temperature-triggered chemical switching growth of in-plane and vertically stacked graphene-boron nitride heterostructures. *Nature communications* **2015,** *6*, 6835.

53. Wang, S.; Wang, X.; Warner, J. H., All chemical vapor deposition growth of MoS_2: h-BN vertical van der Waals heterostructures. *ACS nano* **2015,** *9* (5), 5246-5254.

54. Liu, Z.; Song, L.; Zhao, S.; Huang, J.; Ma, L.; Zhang, J.; Lou, J.; Ajayan, P. M., Direct growth of graphene/hexagonal boron nitride stacked layers. *Nano letters* **2011,** *11* (5), 2032-2037.

55. Liu, Z.; Ma, L.; Shi, G.; Zhou, W.; Gong, Y.; Lei, S.; Yang, X.; Zhang, J.; Yu, J.; Hackenberg, K. P., In-plane heterostructures of graphene and hexagonal boron nitride with controlled domain sizes. *Nature nanotechnology* **2013,** *8* (2), 119.

56. Lin, Y.-C.; Ghosh, R. K.; Addou, R.; Lu, N.; Eichfeld, S. M.; Zhu, H.; Li, M.-Y.; Peng, X.; Kim, M. J.; Li, L.-J., Atomically thin resonant tunnel diodes built from synthetic van der Waals heterostructures. *Nature communications* **2015,** *6*, 7311.

57. Zhang, X.; Meng, F.; Christianson, J. R.; Arroyo-Torres, C.; Lukowski, M. A.; Liang, D.; Schmidt, J. R.; Jin, S., Vertical heterostructures of layered metal chalcogenides by van der Waals epitaxy. *Nano letters* **2014,** *14* (6), 3047-3054.

58. Qiao, J.-B.; Gong, Y.; Zuo, W.-J.; Wei, Y.-C.; Ma, D.-L.; Yang, H.; Yang, N.; Qiao, K.-Y.; Shi, J.-A.; Gu, L., One-step synthesis of van der Waals heterostructures of graphene and two-dimensional superconducting α− Mo_2C. *Physical Review B* **2017,** *95* (20), 201403.

59. Xu, C.; Song, S.; Liu, Z.; Chen, L.; Wang, L.; Fan, D.; Kang, N.; Ma, X.; Cheng, H.-M.; Ren, W., Strongly coupled high-quality graphene/2D superconducting Mo_2C vertical heterostructures with aligned orientation. *ACS nano* **2017,** *11* (6), 5906-5914.

60. Geng, D.; Zhao, X.; Chen, Z.; Sun, W.; Fu, W.; Chen, J.; Liu, W.; Zhou, W.; Loh, K. P., Direct synthesis of large-area 2D Mo_2C on in situ grown graphene. *Advanced Materials* **2017,** *29* (35), 1700072.

61. Zhao, Z.; Qin, F.; Kasiraju, S.; Xie, L.; Alam, M. K.; Chen, S.; Wang, D.; Ren, Z.; Wang, Z.; Grabow, L. C., Vertically aligned MoS_2/Mo_2C hybrid nanosheets grown on carbon paper for efficient electrocatalytic hydrogen evolution. *ACS Catalysis* **2017,** *7* (10), 7312-7318.

62. Wu, J.; Ma, L.; Samanta, A.; Liu, M.; Li, B.; Yang, Y.; Yuan, J.; Zhang, J.; Gong, Y.; Lou, J., Growth of Molybdenum Carbide–Graphene Hybrids from Molybdenum Disulfide Atomic Layer Template. *Advanced Materials Interfaces* **2017,** *4* (4).

63. Tang, C.; Wang, W.; Sun, A.; Qi, C.; Zhang, D.; Wu, Z.; Wang, D., Sulfur-decorated molybdenum carbide catalysts for enhanced hydrogen evolution. *ACS Catalysis* **2015,** *5* (11), 6956-6963.

64. Jeon, J.; Park, Y.; Choi, S.; Lee, J.; Lim, S. S.; Lee, B. H.; Song, Y. J.; Cho, J. H.; Jang, Y. H.; Lee, S., Epitaxial Synthesis of Molybdenum Carbide and Formation of a Mo_2C/MoS_2 Hybrid Structure via Chemical Conversion of Molybdenum Disulfide. *ACS nano* **2018,** *12* (1), 338-346.

65. Xu, C.; Wang, L.; Liu, Z.; Chen, L.; Guo, J.; Kang, N.; Ma, X.-L.; Cheng, H.-M.; Ren, W., Large-area high-quality 2D ultrathin Mo_2C superconducting crystals. *Nature materials* **2015,** *14* (11), 1135-1141.

66. Wu, J.; Ma, L.; Samanta, A.; Liu, M.; Li, B.; Yang, Y.; Yuan, J.; Zhang, J.; Gong, Y.; Lou, J., Growth of molybdenum carbide–graphene hybrids from molybdenum disulfide atomic layer template. *Advanced Materials Interfaces* **2017,** *4* (4), 1600866.

67. Liu, P.; Zhu, X.; Feng, C.; Huang, M.; Li, J.; Lu, Y.; Xiang, B., Enhanced p-type behavior in the hybrid structure of graphene quantum dots/2D-WSe_2. *Applied Physics Letters* **2017,** *111* (11), 111603.

68. Sobhani, A.; Lauchner, A.; Najmaei, S.; Ayala-Orozco, C.; Wen, F.; Lou, J.; Halas, N. J., Enhancing the photocurrent and photoluminescence of single crystal monolayer MoS_2 with resonant plasmonic nanoshells. *Applied Physics Letters* **2014,** *104* (3), 031112.

69. Lei, Y.; Pakhira, S.; Fujisawa, K.; Wang, X.; Iyiola, O. O.; Perea López, N. s.; Laura Elías, A.; Pulickal Rajukumar, L.; Zhou, C.; Kabius, B., Low-temperature Synthesis of Heterostructures of Transition Metal Dichalcogenide Alloys ($W_xMo_{1-x}S_2$) and Graphene with Superior Catalytic Performance for Hydrogen Evolution. *ACS nano* **2017,** *11* (5), 5103-5112.

70. Sreeprasad, T.; Nguyen, P.; Kim, N.; Berry, V., Controlled, defect-guided, metal-nanoparticle incorporation onto MoS_2 via chemical and microwave routes: electrical, thermal, and structural properties. *Nano letters* **2013,** *13* (9), 4434-4441.

71. Komsa, H.-P.; Krasheninnikov, A. V., Two-dimensional transition metal dichalcogenide alloys: stability and electronic properties. *The journal of physical chemistry letters* **2012,** *3* (23), 3652-3656.

72. Levendorf, M. P.; Kim, C.-J.; Brown, L.; Huang, P. Y.; Havener, R. W.; Muller, D. A.; Park, J., Graphene and boron nitride lateral heterostructures for atomically thin circuitry. *Nature* **2012,** *488* (7413), 627.

73. Lu, J.; Zhang, K.; Liu, X. F.; Zhang, H.; Sum, T. C.; Neto, A. H. C.; Loh, K. P., Order–disorder transition in a two-dimensional boron–carbon–nitride alloy. *Nature communications* **2013,**

4, 2681.

74. Voiry, D.; Yamaguchi, H.; Li, J.; Silva, R.; Alves, D. C.; Fujita, T.; Chen, M.; Asefa, T.; Shenoy, V. B.; Eda, G., Enhanced catalytic activity in strained chemically exfoliated WS_2 nanosheets for hydrogen evolution. *Nature materials* **2013,** *12* (9), 850-855.

75. Yang, L.; Fu, Q.; Wang, W.; Huang, J.; Huang, J.; Zhang, J.; Xiang, B., Large-area synthesis of monolayered $MoS_{2(1-x)}Se_{2x}$ with a tunable band gap and its enhanced electrochemical catalytic activity. *Nanoscale* **2015,** *7* (23), 10490-10497.

76. Gong, Q.; Cheng, L.; Liu, C.; Zhang, M.; Feng, Q.; Ye, H.; Zeng, M.; Xie, L.; Liu, Z.; Li, Y., Ultrathin $MoS_{2(1-x)}Se_{2x}$ Alloy Nanoflakes For Electrocatalytic Hydrogen Evolution Reaction. *ACS Catalysis* **2015,** *5* (4), 2213-2219.

77. Feng, Q.; Zhu, Y.; Hong, J.; Zhang, M.; Duan, W.; Mao, N.; Wu, J.; Xu, H.; Dong, F.; Lin, F., Growth of large-area 2D $MoS_{2(1-x)}Se_{2x}$ semiconductor alloys. *Advanced Materials* **2014,** *26* (17), 2648-2653.

78. Kang, J.; Tongay, S.; Li, J.; Wu, J., Monolayer semiconducting transition metal dichalcogenide alloys: Stability and band bowing. *Journal of Applied Physics* **2013,** *113* (14), 143703.

79. Klee, V.; Preciado, E.; Barroso, D.; Nguyen, A. E.; Lee, C.; Erickson, K. J.; Triplett, M.; Davis, B.; Lu, I.-H.; Bobek, S., Superlinear Composition-Dependent Photocurrent in CVD-Grown Monolayer $MoS_{2(1-x)}$) Se_{2x} Alloy Devices. *Nano letters* **2015,** *15* (4), 2612-2619.

80. Li, H.; Duan, X.; Wu, X.; Zhuang, X.; Zhou, H.; Zhang, Q.; Zhu, X.; Hu, W.; Ren, P.; Guo, P., Growth of alloy MoS_{2x} $Se_{2(1-x)}$ nanosheets with fully tunable chemical compositions and optical properties. *Journal of the American Chemical Society* **2014,** *136* (10), 3756-3759.

81. Chen, Y.; Xi, J.; Dumcenco, D. O.; Liu, Z.; Suenaga, K.; Wang, D.; Shuai, Z.; Huang, Y.-S.; Xie, L., Tunable band gap photoluminescence from atomically thin transition-metal

dichalcogenide alloys. *Acs Nano* **2013,** *7* (5), 4610-4616.

82. Kiran, V.; Mukherjee, D.; Jenjeti, R. N.; Sampath, S., Active guests in the $MoS_2/MoSe_2$ host lattice: efficient hydrogen evolution using few-layer alloys of $MoS_{2(1-x)}Se_{2x}$. *Nanoscale* **2014,** *6* (21), 12856-12863.

83. Liu, X.; Wu, J.; Yu, W.; Chen, L.; Huang, Z.; Jiang, H.; He, J.; Liu, Q.; Lu, Y.; Zhu, D., Monolayer $W_xMo_{1-x}S_2$ Grown by Atmospheric Pressure Chemical Vapor Deposition: Bandgap Engineering and Field Effect Transistors. *Advanced Functional Materials* **2017,** *27* (13), 1606469.

84. Sergio, C.; Sinko, M. R.; Gopalan, D. P.; Sivadas, N.; Seyler, K. L.; Watanabe, K.; Taniguchi, T.; Tsen, A. W.; Xu, X.; Xiao, D., Tuning Ising superconductivity with layer and spin–orbit coupling in two-dimensional transition-metal dichalcogenides. *Nature communications* **2018,** *9*.

85. He, S.; He, J.; Zhang, W.; Zhao, L.; Liu, D.; Liu, X.; Mou, D.; Ou, Y.-B.; Wang, Q.-Y.; Li, Z., Phase diagram and electronic indication of high-temperature superconductivity at 65 K in single-layer FeSe films. *Nature materials* **2013,** *12* (7), 605.

86. Ge, J.-F.; Liu, Z.-L.; Liu, C.; Gao, C.-L.; Qian, D.; Xue, Q.-K.; Liu, Y.; Jia, J.-F., Superconductivity above 100 K in single-layer FeSe films on doped $SrTiO_3$. *Nature materials* **2015,** *14* (3), 285.

87. Ye, J.; Zhang, Y.; Akashi, R.; Bahramy, M.; Arita, R.; Iwasa, Y., Superconducting dome in a gate-tuned band insulator. *Science* **2012,** *338* (6111), 1193-1196.

88. Xi, X.; Wang, Z.; Zhao, W.; Park, J.-H.; Law, K. T.; Berger, H.; Forró, L.; Shan, J.; Mak, K. F., Ising pairing in superconducting $NbSe_2$ atomic layers. *Nature Physics* **2016,** *12* (2), 139.

89. Peng, J.; Liu, Y.; Luo, X.; Wu, J.; Lin, Y.; Guo, Y.; Zhao, J.; Wu, X.; Wu, C.; Xie, Y., High Phase Purity of Large-Sized 1T-MoS_2 Monolayers with 2D Superconductivity. *Advanced Materials* **2019,** *31* (19), 1900568.

90. Li, Y.; Gu, Q.; Chen, C.; Zhang, J.; Liu, Q.; Hu, X.; Liu, J.; Liu, Y.; Ling, L.; Tian, M., Nontrivial superconductivity in topological $MoTe_{2-x}S_x$ crystals. *Proceedings of the National Academy of Sciences* **2018,** *115* (38), 9503-9508.

91. Chen, F.; Luo, X.; Xiao, R.; Lu, W.; Zhang, B.; Yang, H.; Li, J.; Pei, Q.; Shao, D.; Zhang, R., Superconductivity enhancement in the S-doped Weyl semimetal candidate $MoTe_2$. *Applied Physics Letters* **2016,** *108* (16), 162601.

92. Rhodes, D.; Yuan, N. F.; Jung, Y.; Antony, A.; Wang, H.; Kim, B.; Chiu, Y.-c.; Taniguchi, T.; Watanabe, K.; Barmak, K., Enhanced Superconductivity in Monolayer T_d-$MoTe_2$ with Tilted Ising Spin Texture. *arXiv preprint arXiv:1905.06508* **2019**.

93. Hsu, W. K.; Zhu, Y. Q.; Firth, S.; Terrones, M.; Terrones, H.; Trasobares, S.; Clark, R. J.; Kroto, H. W.; Walton, D. R., $W_xMo_yC_zS_2$ nanotubes. *Carbon* **2001,** *39* (7), 1107-1111.

94. Hsu, W.; Zhu, Y.; Boothroyd, C.; Kinloch, I.; Trasobares, S.; Terrones, H.; Grobert, N.; Terrones, M.; Escudero, R.; Chen, G., Mixed-Phase $W_xMo_yC_zS_2$ Nanotubes. *Chemistry of materials* **2000,** *12* (12), 3541-3546.

95. Feng, S.; Lin, Z.; Gan, X.; Lv, R.; Terrones, M., Doping two-dimensional materials: ultra-sensitive sensors, band gap tuning and ferromagnetic monolayers. *Nanoscale Horizons* **2017,** *2* (2), 72-80.

96. Lin, Z.; Carvalho, B. R.; Kahn, E.; Lv, R.; Rao, R.; Terrones, H.; Pimenta, M. A.; Terrones, M., Defect engineering of two-dimensional transition metal dichalcogenides. *2D Materials* **2016,** *3* (2), 022002.

97. Azizi, A.; Wang, Y.; Lin, Z.; Wang, K.; Elias, A. L.; Terrones, M.; Crespi, V. H.; Alem, N., Spontaneous formation of atomically thin stripes in transition metal dichalcogenide monolayers. *Nano letters* **2016,** *16* (11), 6982-6987.

98. Xia, B.; Liu, P.; Liu, Y.; Gao, D.; Xue, D.; Ding, J., Re doping induced 2H-1T phase

transformation and ferromagnetism in MoS_2 nanosheets. *Applied Physics Letters* **2018,** *113* (1), 013101.

99. Lin, Z.; Thee, M. T.; Elías, A. L.; Feng, S.; Zhou, C.; Fujisawa, K.; Perea-López, N.; Carozo, V.; Terrones, H.; Terrones, M., Facile synthesis of MoS_2 and $Mo_xW_{1-x}S_2$ triangular monolayers. *Apl Materials* **2014,** *2* (9), 092514.

100. Gong, Y.; Liu, Z.; Lupini, A. R.; Shi, G.; Lin, J.; Najmaei, S.; Lin, Z.; Elías, A. L.; Berkdemir, A.; You, G., Band gap engineering and layer-by-layer mapping of selenium-doped molybdenum disulfide. *Nano letters* **2013,** *14* (2), 442-449.

101. Zhang, K.; Bersch, B. M.; Joshi, J.; Addou, R.; Cormier, C. R.; Zhang, C.; Xu, K.; Briggs, N. C.; Wang, K.; Subramanian, S., Tuning the electronic and photonic properties of monolayer MoS_2 via in situ rhenium substitutional doping. *Advanced Functional Materials* **2018,** *28* (16), 1706950.

102. Suh, J.; Park, T.-E.; Lin, D.-Y.; Fu, D.; Park, J.; Jung, H. J.; Chen, Y.; Ko, C.; Jang, C.; Sun, Y., Doping against the native propensity of MoS_2: degenerate hole doping by cation substitution. *Nano letters* **2014,** *14* (12), 6976-6982.

103. Laskar, M. R.; Nath, D. N.; Ma, L.; Lee, E. W.; Lee, C. H.; Kent, T.; Yang, Z.; Mishra, R.; Roldan, M. A.; Idrobo, J.-C., p-type doping of MoS_2 thin films using Nb. *Applied Physics Letters* **2014,** *104* (9), 092104.

104. Chua, X. J.; Luxa, J.; Eng, A. Y. S.; Tan, S. M.; Sofer, Z. k.; Pumera, M., Negative electrocatalytic effects of p-doping niobium and tantalum on MoS_2 and WS_2 for the hydrogen evolution reaction and oxygen reduction reaction. *ACS Catalysis* **2016,** *6* (9), 5724-5734.

105. Azcatl, A.; Qin, X.; Prakash, A.; Zhang, C.; Cheng, L.; Wang, Q.; Lu, N.; Kim, M. J.; Kim, J.; Cho, K., Covalent nitrogen doping and compressive strain in MoS_2 by remote N_2 plasma exposure. *Nano letters* **2016,** *16* (9), 5437-5443.

106. Nipane, A.; Karmakar, D.; Kaushik, N.; Karande, S.; Lodha, S., Few-layer MoS_2 p-type devices enabled by selective doping using low energy phosphorus implantation. *ACS nano* **2016,** *10* (2), 2128-2137.

107. Tongay, S.; Zhou, J.; Ataca, C.; Liu, J.; Kang, J. S.; Matthews, T. S.; You, L.; Li, J.; Grossman, J. C.; Wu, J., Broad-range modulation of light emission in two-dimensional semiconductors by molecular physisorption gating. *Nano letters* **2013,** *13* (6), 2831-2836.

108. Ma, K. Y.; Yoon, S. I.; Jang, A.-R.; Jeong, H. Y.; Kim, Y.-J.; Nayak, P. K.; Shin, H. S., Hydrogenation of monolayer molybdenum diselenide via hydrogen plasma treatment. *Journal of Materials Chemistry C* **2017,** *5* (43), 11294-11300.

109. Zhang, F.; Lu, Y.; Schulman, D. S.; Zhang, T.; Fujisawa, K.; Lin, Z.; Lei, Y.; Elias, A. L.; Das, S.; Sinnott, S. B., Carbon doping of WS_2 monolayers: Bandgap reduction and p-type doping transport. *Science advances* **2019,** *5* (5), eaav5003.

110. Dietl, T., Ferromagnetic semiconductors. *Semiconductor Science and Technology* **2002,** *17* (4), 377.

111. Gibertini, M.; Koperski, M.; Morpurgo, A.; Novoselov, K., Magnetic 2D materials and heterostructures. *Nat. Nanotech* **2019,** *14*, 408-419.

112. Li, H.; Ruan, S.; Zeng, Y. J., Intrinsic Van Der Waals Magnetic Materials from Bulk to the 2D Limit: New Frontiers of Spintronics. *Advanced Materials* **2019**, 1900065.

113. Yun, S. J.; Duong, D. L.; Doan, M.-H.; Singh, K.; Phan, T. L.; Choi, W.; Kim, Y.-M.; Lee, Y. H., Room-temperature ferromagnetism in monolayer WSe_2 semiconductor via vanadium dopant. *arXiv preprint arXiv:1806.06479* **2018**.

114. Habib, M.; Muhammad, Z.; Khan, R.; Wu, C.; ur Rehman, Z.; Zhou, Y.; Liu, H.; Song, L., Ferromagnetism in CVT grown tungsten diselenide single crystals with nickel doping. *Nanotechnology* **2018,** *29* (11), 115701.

115. Wang, Y.; Li, S.; Yi, J., Electronic and magnetic properties of Co doped MoS_2 monolayer. *Scientific reports* **2016,** *6*, 24153.

116. Ramasubramaniam, A.; Naveh, D., Mn-doped monolayer MoS_2: an atomically thin dilute magnetic semiconductor. *Physical Review B* **2013,** *87* (19), 195201.

117. Coelho, P. M.; Komsa, H. P.; Lasek, K.; Kalappattil, V.; Karthikeyan, J.; Phan, M. H.; Krasheninnikov, A. V.; Batzill, M., Room-Temperature Ferromagnetism in $MoTe_2$ by Post-Growth Incorporation of Vanadium Impurities. *Advanced Electronic Materials* **2019,** *5* (5), 1900044.

118. Ohno, H.; Chiba, D.; Matsukura, F.; Omiya, T.; Abe, E.; Dietl, T.; Ohno, Y.; Ohtani, K., Electric-field control of ferromagnetism. *Nature* **2000,** *408* (6815), 944.

119. Chang, C.-Z.; Zhang, J.; Feng, X.; Shen, J.; Zhang, Z.; Guo, M.; Li, K.; Ou, Y.; Wei, P.; Wang, L.-L., Experimental observation of the quantum anomalous Hall effect in a magnetic topological insulator. *Science* **2013,** *340* (6129), 167-170.

120. Lv, R.; Robinson, J. A.; Schaak, R. E.; Sun, D.; Sun, Y.; Mallouk, T. E.; Terrones, M., Transition metal dichalcogenides and beyond: synthesis, properties, and applications of single-and few-layer nanosheets. *Accounts of chemical research* **2014,** *48* (1), 56-64.

121. Zhang, F.; Erb, C.; Runkle, L.; Zhang, X.; Alem, N., Etchant-free transfer of 2D nanostructures. *Nanotechnology* **2017,** *29* (2), 025602.

122. Zhang, T.; Fujisawa, K.; Granzier-Nakajima, T.; Zhang, F.; Lin, Z.; Kahn, E.; Perea-López, N.; Elías, A. L.; Yeh, Y.-T.; Terrones, M., Clean Transfer of 2D Transition Metal Dichalcogenides using Cellulose Acetate for Atomic Resolution Characterizations. *ACS Applied Nano Materials* **2019**.

123. Lee, G.-H.; Yu, Y.-J.; Cui, X.; Petrone, N.; Lee, C.-H.; Choi, M. S.; Lee, D.-Y.; Lee, C.; Yoo, W. J.; Watanabe, K., Flexible and transparent MoS_2 field-effect transistors on hexagonal boron nitride-graphene heterostructures. *ACS nano* **2013,** *7* (9), 7931-7936.

124. Shi, Y.; Zhou, W.; Lu, A.-Y.; Fang, W.; Lee, Y.-H.; Hsu, A. L.; Kim, S. M.; Kim, K. K.; Yang, H. Y.; Li, L.-J., van der Waals epitaxy of MoS_2 layers using graphene as growth templates. *Nano letters* **2012,** *12* (6), 2784-2791.

125. Pierucci, D.; Henck, H.; Naylor, C. H.; Sediri, H.; Lhuillier, E.; Balan, A.; Rault, J. E.; Dappe, Y. J.; Bertran, F.; Le Fèvre, P., Large area molybdenum disulphide-epitaxial graphene vertical Van der Waals heterostructures. *Scientific reports* **2016,** *6*, 26656.

126. Liu, X.; Balla, I.; Bergeron, H.; Campbell, G. P.; Bedzyk, M. J.; Hersam, M. C., Rotationally commensurate growth of MoS_2 on epitaxial graphene. *ACS nano* **2015,** *10* (1), 1067-1075.

127. Ling, X.; Lee, Y.-H.; Lin, Y.; Fang, W.; Yu, L.; Dresselhaus, M. S.; Kong, J., Role of the seeding promoter in MoS_2 growth by chemical vapor deposition. *Nano letters* **2014,** *14* (2), 464-472.

128. Okada, M.; Sawazaki, T.; Watanabe, K.; Taniguch, T.; Hibino, H.; Shinohara, H.; Kitaura, R., Direct chemical vapor deposition growth of WS_2 atomic layers on hexagonal boron nitride. *ACS nano* **2014,** *8* (8), 8273-8277.

129. Gong, Y.; Lin, J.; Wang, X.; Shi, G.; Lei, S.; Lin, Z.; Zou, X.; Ye, G.; Vajtai, R.; Yakobson, B. I., Vertical and in-plane heterostructures from WS_2/MoS_2 monolayers. *Nature materials* **2014,** *13* (12), 1135.

130. Huang, C.; Wu, S.; Sanchez, A. M.; Peters, J. J.; Beanland, R.; Ross, J. S.; Rivera, P.; Yao, W.; Cobden, D. H.; Xu, X., Lateral heterojunctions within monolayer $MoSe_2$–WSe_2 semiconductors. *Nature materials* **2014,** *13* (12), 1096.

131. Duan, X.; Wang, C.; Shaw, J. C.; Cheng, R.; Chen, Y.; Li, H.; Wu, X.; Tang, Y.; Zhang, Q.; Pan, A., Lateral epitaxial growth of two-dimensional layered semiconductor heterojunctions. *Nature nanotechnology* **2014,** *9* (12), 1024.

132. Fu, D.; Zhao, X.; Zhang, Y.-Y.; Li, L.; Xu, H.; Jang, A.-R.; Yoon, S. I.; Song, P.; Poh, S. M.; Ren, T., Molecular beam epitaxy of highly crystalline monolayer molybdenum disulfide on hexagonal boron nitride. *Journal of the American Chemical Society* **2017,** *139* (27), 9392-9400.

133. Yan, Y.; Xia, B.; Li, N.; Xu, Z.; Fisher, A.; Wang, X., Vertically oriented MoS_2 and WS_2 nanosheets directly grown on carbon cloth as efficient and stable 3-dimensional hydrogen-evolving cathodes. *Journal of Materials Chemistry A* **2015,** *3* (1), 131-135.

134. Dolui, K.; Rungger, I.; Pemmaraju, C. D.; Sanvito, S., Possible doping strategies for MoS_2 monolayers: An ab initio study. *Physical Review B* **2013,** *88* (7), 075420.

135. Cheng, Y.; Zhu, Z.; Mi, W.; Guo, Z.; Schwingenschlögl, U., Prediction of two-dimensional diluted magnetic semiconductors: Doped monolayer MoS_2 systems. *Physical Review B* **2013,** *87* (10), 100401.

136. Feng, N.; Mi, W.; Cheng, Y.; Guo, Z.; Schwingenschlögl, U.; Bai, H., First principles prediction of the magnetic properties of Fe-X_6 (X= S, C, N, O, F) doped monolayer MoS_2. *Scientific reports* **2014,** *4*, 3987.

137. Zhang, K.; Feng, S.; Wang, J.; Azcatl, A.; Lu, N.; Addou, R.; Wang, N.; Zhou, C.; Lerach, J.; Bojan, V., Manganese doping of monolayer MoS_2: the substrate is critical. *Nano letters* **2015,** *15* (10), 6586-6591.

138. Wang, S. Y.; Ko, T. S.; Huang, C. C.; Huang, Y. S., Optical and electrical properties of MoS_2 and Fe-doped MoS_2. *Japanese Journal of Applied Physics* **2014,** *53* (4S), 04EH07.

139. Li, B.; Huang, L.; Zhong, M.; Huo, N.; Li, Y.; Yang, S.; Fan, C.; Yang, J.; Hu, W.; Wei, Z., Synthesis and transport properties of large-scale alloy $Co_{0.16}Mo_{0.84}S_2$ bilayer nanosheets. *ACS nano* **2015,** *9* (2), 1257-1262.

140. Lin, Y. C.; Dumcenco, D. O.; Komsa, H. P.; Niimi, Y.; Krasheninnikov, A. V.; Huang, Y. S.; Suenaga, K., Properties of individual dopant atoms in single-layer MoS_2: atomic structure,

migration, and enhanced reactivity. *Advanced materials* **2014,** *26* (18), 2857-2861.

141. Kang, N.; Paudel, H. P.; Leuenberger, M. N.; Tetard, L.; Khondaker, S. I., Photoluminescence quenching in single-layer MoS_2 via oxygen plasma treatment. *The Journal of Physical Chemistry C* **2014,** *118* (36), 21258-21263.

142. Radhakrishnan, S.; Das, D.; Samanta, A.; Carlos, A.; Deng, L.; Alemany, L. B.; Weldeghiorghis, T. K.; Khabashesku, V. N.; Kochat, V.; Jin, Z., Fluorinated h-BN as a magnetic semiconductor. *Science advances* **2017,** *3* (7), e1700842.

143. Sun, Y.; Fujisawa, K.; Lin, Z.; Lei, Y.; Mondschein, J. S.; Terrones, M.; Schaak, R. E., Low-Temperature Solution Synthesis of Transition Metal Dichalcogenide Alloys with Tunable Optical Properties. *Journal of the American Chemical Society* **2017,** *139* (32), 11096-11105.

144. Xia, B.; Guo, Q.; Gao, D.; Shi, S.; Tao, K., High temperature ferromagnetism in Cu-doped MoS_2 nanosheets. *Journal of Physics D: Applied Physics* **2016,** *49* (16), 165003.

145. Ahmed, S.; Ding, X.; Bao, N.; Bian, P.; Zheng, R.; Wang, Y.; Murmu, P. P.; Kennedy, J. V.; Liu, R.; Fan, H., Inducing high coercivity in MoS_2 nanosheets by transition element doping. *Chemistry of Materials* **2017,** *29* (21), 9066-9074.

146. Zhang, Q.; Wang, L.; Wang, J.; Yu, X.; Ge, J.; Zhang, H.; Lu, B., Semimetallic vanadium molybdenum sulfide for high-performance battery electrodes. *Journal of Materials Chemistry A* **2018,** *6* (20), 9411-9419.

147. Mattox, D. M., *Handbook of physical vapor deposition (PVD) processing*. William Andrew: 2010.

148. Jung, Y.; Shen, J.; Liu, Y.; Woods, J. M.; Sun, Y.; Cha, J. J., Metal seed layer thickness-induced transition from vertical to horizontal growth of MoS_2 and WS_2. *Nano letters* **2014,** *14* (12), 6842-6849.

149. Feng, Q.; Mao, N.; Wu, J.; Xu, H.; Wang, C.; Zhang, J.; Xie, L., Growth of $MoS_{2(1-x)}Se_{2x}$

(x= 0.41–1.00) Monolayer Alloys with Controlled Morphology by Physical Vapor Deposition. *ACS nano* **2015,** *9* (7), 7450-7455.

150. Woods, J. M.; Jung, Y.; Xie, Y.; Liu, W.; Liu, Y.; Wang, H.; Cha, J. J., One-step synthesis of MoS2/WS2 layered heterostructures and catalytic activity of defective transition metal dichalcogenide films. *ACS nano* **2016,** *10* (2), 2004-2009.

151. Binnewies, M.; Glaum, R.; Schmidt, M.; Schmidt, P., Chemical vapor transport reactions–A historical review. *Zeitschrift für anorganische und allgemeine Chemie* **2013,** *639* (2), 219-229.

152. Nitsche, R.; Bölsterli, H.; Lichtensteiger, M., Crystal growth by chemical transport reactions—I: Binary, ternary, and mixed-crystal chalcogenides. *Journal of Physics and Chemistry of Solids* **1961,** *21* (3-4), 199-205.

153. Nguyen, M. A. T.; Gupta, A. S.; Shevrin, J.; Akamatsu, H.; Xu, P.; Lin, Z.; Wang, K.; Zhu, J.; Gopalan, V.; Terrones, M., Random anion distribution in MS_xSe_{2-x} (M= Mo, W) crystals and nanosheets. *RSC advances* **2018,** *8* (18), 9871-9878.

154. Sun, X.; Dai, J.; Guo, Y.; Wu, C.; Hu, F.; Zhao, J.; Zeng, X.; Xie, Y., Semimetallic molybdenum disulfide ultrathin nanosheets as an efficient electrocatalyst for hydrogen evolution. *Nanoscale* **2014,** *6* (14), 8359-8367.

155. Shi, Y.; Li, H.; Li, L.-J., Recent advances in controlled synthesis of two-dimensional transition metal dichalcogenides via vapour deposition techniques. *Chemical Society Reviews* **2015,** *44* (9), 2744-2756.

156. Li, H.; Zhang, Q.; Duan, X.; Wu, X.; Fan, X.; Zhu, X.; Zhuang, X.; Hu, W.; Zhou, H.; Pan, A., Lateral Growth of Composition Graded Atomic Layer $MoS_{2(1-x)}$ Se_{2x} Nanosheets. *Journal of the American Chemical Society* **2015,** *137* (16), 5284-5287.

157. Zhang, J.; Jia, S.; Kholmanov, I.; Dong, L.; Er, D.; Chen, W.; Guo, H.; Jin, Z.; Shenoy, V. B.; Shi, L., Janus monolayer transition-metal dichalcogenides. *ACS nano* **2017,** *11* (8), 8192-8198.

Chapter 2

Experimental Procedure and Material Characterization

2.1 Synthesis of pristine/doped/ alloyed transition metal dichalcogenide and carbide

2.1.1 Metal organic chemical vapor deposition of tungsten diselenide on boron nitride

The hBN flakes were mechanically exfoliated from powder (grade PT 110, Momentive Performance Materials) and placed on a c-plane sapphire substrate. The hBN flakes on sapphire substrate is applied for reactive ion etching treatment. 50 sccm of helium gas was introduced into a Tepla M4L Plasma Etch system at a regulated pressure of 180 mTorr, with a radio frequency (13.56 MHz) power of 50W to generate He plasma. Different etching times were applied to hBN surfaces while fixing other plasma generation parameters. Both freestanding ME-hBN (transferred by PMMA-assisted method onto TEM grid) and ME-hBN placed on sapphire substrate were used as templates to fabricate WSe_2/hBN heterostructures by gas source CVD process by Dr. Xiaotian Zhang at Prof. Joan M. Redwing's laboratory.[1,2] Substrate was placed onto a SiC-coated graphite susceptor which was inductively heated up to 800ºC under H_2 in a cold wall vertical quartz tube reactor. $W(CO)_6$ and H_2Se was introduced into the reactor during the whole growth process.

2.1.2 Powder vaporization synthesis of pristine tungsten disulfide monolayers

Pristine monolayer WS_2 samples were synthesized by atmospheric pressure chemical vapor deposition (CVD)[3]. Silicon substrates with 300nm of SiO_2 were used as growth substrates for powder vaporization process. These substrates were cleaned as follow: first sonicated in acetone and isopropyl alcohol for 10 minutes each and then cleaned with deionized water, followed by medium air plasma treated for 10 mins. afterwards, they were sonicated and rinsed with deionized water again and dried with pure nitrogen. A quartz tube furnace with ultra-high purity argon as the carrier gas was employed as the reaction chamber. Mixed powders of WO_3 and NaBr (5 mg:1 mg) were loaded inside an aluminum boat, and air plasma cleaned Si/SiO_2 wafers were placed on the top of the boat facing down. Sulfur powders (300 mg) were located the upstream and were vaporized at 250°C during the experiments. In a typical 15 min synthesis, WO_3 and NaBr powders along with the growth substrate were heated up to 825 °C, while the sulfur was simultaneously heated up by a heating tape. The furnace was allowed to cool to room temperature naturally.

2.1.3 Plasma-assisted carbon doping of monolayer WS_2

As-grown WS_2 monolayers were placed at the hot-zone of a home-built inductively coupled plasma enhanced CVD system (PECVD).[4] The plasma was generated by applying radio frequency (13.56 MHz) to a mixture of CH_4 and Ar/H_2. At around 1 Torr. The system was ramped up to 400 °C in 15 min and the experiment was carried out for 10 min. The flow of Ar/H_2 was 200 sccm during the treatment, and flow of CH_4 varied from 2 to 8 sccm, in order to achieve samples with various doping levels. It is noteworthy that the decision of using methane (CH_4) over ethane (C_2H_6), ethylene (C_2H_4), acetylene (C_2H_2) or other hydrocarbons, is due to the simplification of the active hydrocarbon plasma species present in the chamber only to CH_x-, which act as anion substitutions for S within the WS_2 lattice. The other listed options for hydrocarbon gases may

generate plasma species containing more than one carbon atom, which would have complicated the kinetics of the process.

2.1.4 Powder vaporization synthesis of pristine and vanadium doped WS_2 monolayers

0.05 g W precursor ammonium metatungstate ($(NH_4)_6H_2W_{12}O_{40} \cdot xH_2O$, AMT) and 0.2 g assisting salt sodium cholate ($C_{24}H_{39}NaO_5 \cdot xH_2O$) powders were dissolved in 10 mL water to form a tungsten precursor solution. 0.05g vanadyl sulfate ($VO[SO_4]$) powder were dissolved in 10mL to form vanadium precursor ($1x10^{-2}$ mol/L). The W and V with different concentrations were controlled to form solution-based cation precursors. We drop casted the precursor solution onto a SiO_2/Si substrate followed by spin-coating for 1 min with 3000 rpm. The powder vaporization synthesis process is carried out in a two-zone furnace with sulfur powder (400 mg) heated upstream at low temperature (220 ℃, heated up using a heating tape), and the cation precursor, spin-coated on the SiO_2/Si substrates, in the high temperature (825 ℃) zone. Ultrahigh purity argon was employed as the carrier gas. The furnace was then allowed to cool to room temperature naturally after 15 min synthesis.

2.1.5 Atmospheric pressure CVD synthesis of 2D Mo_2C on molten Cu

2D Mo_2C domains were grown through atmospheric pressure chemical vapor deposition (APCVD) directly onto Cu substrates as previously reported.[5] In our experiments, Ar carrier gas with a small CH_4 flow (Ar:CH_4=500:1) was controlled by enclosing the stacked Mo/Cu metal foils in a quartz tube at a temperature of 1090 ℃. A high cooling rate (~200 ℃/min) is set after 15-30 minutes of growth. The details in the growth process and effect of growth parameters on the synthesized materials are discussed at Chapter 4 in details. The 2D α-phase Mo_2C can be transferred

from the Mo-Cu assembly via a PMMA-assisted method and onto arbitrary substrates by etching in $FeCl_3$ solution for 3 hours.

2.1.6 Assembly of MoS_2/carbide heterostacks in the gas source CVD system

MoS_2/carbide heterolayers are produced via APCVD system with as-grown Mo_2C and H_2S as the precursors. The reaction was performed under H_2S flow at a rate of 5 sccm. Ultra-high purity argon gas was used as the carrier gas through the reactor to maintain a total flow rate at 35 sccm. Sulfurization was achieved at total reactor pressure of 700~1000 mTorr, after a growth time in the range of 1-20 minutes and with the substrate at a temperature of 600 ℃.

2.2 Materials characterization methods

2.2.1 Raman and photoluminescence (PL) spectroscopy

A Renishaw inVia microscope with a Coherent Innova 70C argon-krypton laser with photon energies of 488 nm and 514 nm was used for acquiring the Raman and PL spectra using a backscattering configuration with an 1800 line/mm grating. Temperature-dependent PL spectra were measured using a Linkam THMS600 optical stage as the sample holder. All the low-temperature PL spectra were acquired in liquid nitrogen environment. PL mapping was carried out using a HORIBA LabRAM HR Evolution high spectral resolution analytical Raman microscope with a laser wavelength of 532 nm.

2.2.2 Transmission electron microscopy sample preparation, imaging and spectroscopy

The as-synthesized materials are transferred onto TEM grids for further TEM investigation or onto other substrates for device fabrication or performance test by the following methods. PMMA-assisted transfer method of 2D materials are the widely used for transfer of 2D flakes and films which includes PMMA spin-coating and wet-etching of the substrate, $FeCl_3$ for Cu etching and NaOH for SiO_2 etching.[3] We improved the PMMA-assisted transfer method as an etchant-free transfer process to avoid the damage and contaminations.[6]

The cross-section TEM samples were prepared using a dual-beam focused ion beam (FIB) technique in FEI SEM Helios Nanolab 660. High resolution TEM (HRTEM) and scanning TEM/electron dispersive spectroscopy (STEM-EDS) of the cross-section of the sample was performed with a FEI Talos F200X microscope using a SuperX EDS detector, operating at 200kV. The HRTEM imaging condition for hBN surface defects and cross sectional of molybdenum carbide/disulfide interfaces were tuned to a negative Cs to provide white atom contrast at a slight over focus. Imaging of surface defects on BN carried out at the electron dose of ~5000 $e^{-}/Å^2 \cdot s$ to minimize structural damage. Aberration-corrected STEM imaging and electron energy loss spectroscopy (EELS) were performed by FEI Titan G^2 60-300 microscope, operating at 80kV with double spherical aberration correction, offering the sub-angstrom imaging resolution. A HAADF detector was used for the ADF-STEM imaging with a collection angle of 51-300 mrad, a beam current of 45pA, and beam convergence angle of 30 mrad (C2 aperture of 70 μm) for STEM image acquisition.

For the HAADF-STEM image analysis, a Gaussian blur filter (r=2.00) was applied (by the ImageJ program) to eliminate noise and enhance the visibility of structural details, while the line profiles of ADF intensity were captured by analyzing the raw STEM images. Atomic resolution

STEM image simulations were conducted by using the QSTEM package[7]. The applied parameters, acceleration voltage, convergence angle and inner/outer angle for the HAADF detector and spherical aberration (C_3 and C_5), were all adjusted according to the experimental conditions.

2.2.3 Other characterization methods

The surface morphology of the samples was analyzed by atomic force microscopy (AFM) using a Bruker Dimension Icon Atomic Force Microscope system and field emission scanning electron microscopy (FESEM) using a Zeiss Merlin instrument at 5 kV. The crystal structure of the samples was detected by X-ray Diffraction (XRD), which was taken with PANalytical Empryean X-Ray Diffractometer with a Cu source. The bandgap was estimated by UV-Vis absorption spectra, which were transformed from reflectance measurements, acquired on Perkin-Elmer Lambda 950 with a universal reflectance accessory (URA). X-ray Photoelectron Spectroscopy (XPS) experiments were done by Physical Electronics VersaProbe II facility couple with monochromated Al-Kα X-ray source, to understand the elemental composition and chemical states in the samples. Peaks were charge referenced to the CH_x band in the C 1s spectra at 284.8 eV. Measurements were made at a takeoff angle of 45° with respect to the sample surface plane. Atomic quantification was performed using instrumental relative sensitivity factors (RSFs) that account for the x-ray cross-section and inelastic mean free path of the electrons.

2.3 Materials property performance test

2.3.1 Electrical transport measurement

The electrical transport measurements were done by Prof. Saptarshi Das group at Penn State University. The WSe_2/BN heterostacks and WSe_2 films were transferred onto a 100 nm SiO_2 on p^{++} Si substrate using a PMMA assisted transfer process. The 5 μm channel regions for the WSe_2 on SiO_2 and WSe_2 on hBN on SiO_2 devices were defined using electron beam lithography (Raith EBPG-5200) and ZEP520A photoresist. The WSe_2 was etched using an SF_6/O_2 based etch in a Plasma-Therm Versalock etch tool. The resist was then removed by submersing in 85 °C JT Baker PRS3000 for 30 minutes followed by an IPA rise. The source drain contacts were patterned using a MMA/PMMA resist process and the 40 nm Ni/ 30 nm Au metal contacts were deposited via electron beam evaporation (Kurt J. Lesker Lab-18). Measurements were taken in vacuum ($<10^{-5}$ Torr) using a Lakeshore CRX-VF probe station and a Keysight B1500A. The hBN thickness was measured by AFM.[2]

The back-gated WS_2 FETs were fabricated by first transferring the undoped and carbon-doped WS_2 from the growth substrate onto a Si p^{++}/TiN/Pt substrate with a 50 nm Al_2O_3 gate dielectric grown via atomic layer deposition (ALD) using a poly(methyl methacrylate) (PMMA)-assisted transfer process. The source and drain regions were patterned using electron beam lithography with a bilayer copolymer PMMA process and developed in a 1:1 MIBK:IPA solution (methyl isobutyl ketone, isopropyl alcohol) solution. Electron beam evaporation was used to deposit the 40 nm Ni/ 30 nm Au contacts followed by a lift-off procedure in acetone and IPA. The devices were measured after sitting in high vacuum ($<10^{-5}$ Torr) for >8 hours in order to eliminate any transient effects due to adsorbed species. [4]

Pristine and V-doped WS_2 triangles were transferred from the growth substrate (Si/SiO_2) to a 50 nm thick and atomic layer deposition grown Al_2O_3 substrate with Pt/TiN/p^{++}Si as the back-

gate electrode. All FETs were fabricated with a channel length of 1 μm with 40 nm Ni/30 nm Au as the source/drain contact electrodes defined using standard electron-beam lithography process.

2.3.2 Thermal transport measurement

The thermal transport measurements were done by Prof. Patrick E. Hopkins group at University of Virginia. To examine the thermal boundary conductances (h_K) of devices contingent on the use of V-doped WS_2, we deposited a nominally 80 nm Al film via electron beam evaporation. We measured the total conductance of the Al/doped WS_2/SiO_2 interface via time-domain thermoreflectance (TDTR). The specific analyses can be found elsewhere.[8] In our implementation, the 808.5 nm output of a Ti:Sapphire oscillator is spectrally separated into high-energy pump and low-energy probe paths. The pump is electro-optically modulated at 8.4 MHz, and creates a frequency dependent heating event at the sample surface. The probe is mechanically delayed in time, and monitors the change in reflectivity due to the pump-induced heating event (i.e., thermoreflectivity) as a function of delay time. Both the pump and probe are concentrically focused through a 10x objective, yielding $1/e^2$ diameters of 14 and 11 μm, respectively. The data are fit to the radially symmetric heat diffusion equation to extract the conductances at the Al/ V-doped WS_2/SiO_2 interface.

2.3.3 Magnetic measurement

The magnetic measurements were done by Prof. Manh-Huong Phan group at University of South Florida. Physical Property Measurement System (PPMS) from Quantum Design with a vibrating sample magnetometer (VSM) magnetometer was used for Temperature- and magnetic

field-dependent magnetization measurements with a temperature range of 2 – 350 K and fields up to 9 T.

2.3.4 Superconductivity measurement

The superconductivity measurements were done by Prof. Luis Balicas group at Florida State University. To fabricate the electrical contacts standard e-beam lithography and e-beam evaporation techniques were used to deposit a 50 nm of Au on 5 nm of Ti. Measurements as a function of magnetic field and temperature were performed in a Physical Properties Measurement System using conventional electronics.

2.4 References

1. Zhang, X.; Choudhury, T. H.; Chubarov, M.; Xiang, Y.; Jariwala, B.; Zhang, F.; Alem, N.; Wang, G.-C.; Robinson, J. A.; Redwing, J. M., Diffusion-controlled epitaxy of large area coalesced WSe_2 monolayers on sapphire. *Nano letters* **2018,** *18* (2), 1049-1056.

2. Zhang, X.; Zhang, F.; Wang, Y.; Schulman, D. S.; Zhang, T.; Bansal, A.; Alem, N.; Das, S.; Crespi, V. H.; Terrones, M., Defect-Controlled Nucleation and Orientation of WSe_2 on hBN: A Route to Single-Crystal Epitaxial Monolayers. *ACS nano* **2019,** *13* (3), 3341-3352.

3. Elías, A. L.; Perea-Lopez, N.; Castro-Beltran, A.; Berkdemir, A.; Lv, R.; Feng, S.; Long, A. D.; Hayashi, T.; Kim, Y. A.; Endo, M., Controlled synthesis and transfer of large-area WS_2 sheets: from single layer to few layers. *ACS nano* **2013,** *7* (6), 5235-5242.

4. Zhang, F.; Lu, Y.; Schulman, D. S.; Zhang, T.; Fujisawa, K.; Lin, Z.; Lei, Y.; Elias, A. L.; Das, S.; Sinnott, S. B., Carbon doping of WS_2 monolayers: Bandgap reduction and p-type doping transport. *Science advances* **2019,** *5* (5), eaav5003.

5. Xu, C.; Wang, L.; Liu, Z.; Chen, L.; Guo, J.; Kang, N.; Ma, X.-L.; Cheng, H.-M.; Ren, W., Large-area high-quality 2D ultrathin Mo_2C superconducting crystals. *Nature materials* **2015,** *14* (11), 1135.

6. Zhang, F.; Erb, C.; Runkle, L.; Zhang, X.; Alem, N., Etchant-free transfer of 2D nanostructures. *Nanotechnology* **2017,** *29* (2), 025602.

7. Koch, C. T., *Determination of core structure periodicity and point defect density along dislocations*. 2002.

8. Hopkins, P. E.; Serrano, J. R.; Phinney, L. M.; Kearney, S. P.; Grasser, T. W.; Harris, C. T., Criteria for cross-plane dominated thermal transport in multilayer thin film systems during modulated laser heating. *Journal of Heat Transfer* **2010,** *132* (8), 081302.

Chapter 3

Defect-Controlled Nucleation and Orientation of WSe_2 on hBN – A Route to Single Crystal Epitaxial Monolayers

F.Z. and M.T. acknowledge Army Research Office (ARO) grant W911NF-17-1-0324. Clarification of my contribution for this work: Ideas are from both me and Dr. Xiaotian Zhang, the MOCVD growth of WSe2 are done by Dr. Xiaotian Zhang, while all TEM imaging and microscopy experiment data acquisition and analyses, BN substrate preparation and plasma treatment of the surface, Raman and PL measurements and data analyses are done by me.

3.1 Introduction and Motivation

The rapid development of device technologies based on 2D TMDs and their heterostructures presents increasing demand for synthesis of wafer-scale high quality single crystal monolayer and few layer films. To reduce the prevalence of random orientations and high-angle grain boundaries, epitaxial growth of TMD domains or films by MOCVD methods has been further investigated on various single crystal substrates such as epitaxial graphene,[1,2,3] hexagonal boron nitride (hBN),[4,5] and c-plane sapphire.[6] The epitaxial growth of TMDs has been further developed

into a wafer-scale process *via* controlled nucleation and coalescence of a high density of islands into a continuous film on c-plane sapphire.[7] However, inversion domain boundaries (IDBs) (also referred to as mirror twin grain boundaries) were still observed in these films resulting from a merging of a mixture of 0º and 180º oriented domains.[2,5,7,8] IDBs have been predicted and experimentally demonstrated to exhibit metallic character and consequently can serve as conducting channels within the monolayer that negatively impact both electrical and optical properties.[9,10,11,12] In addition, non-uniformities in the optical and transport properties of these TMD films arise from steps and surface dangling bonds at the interface between the 2D film and 3D substrate.[7,13,14] All of these factors negatively impact the properties of coalesced monolayer films and also promote undesirable multilayer growth.

In contrast to sapphire, an hBN substrate offers many potential benefits for the epitaxial growth of large TMD domains. The basal plane of hBN, in its pristine form, can be considered free of steps and dangling bonds and is expected to enable reduced nucleation density and high adatom surface diffusivity. The hexagonal crystal structure of hBN makes it compatible for epitaxial growth of most 2D TMDs.[5,15] In addition, the high dielectric constant and chemically inert surface of hBN suppresses scattering from charged impurities and substrate phonons, yielding higher mobilities[16,17,18] and increased exciton densities[19,20] in adjacent TMD monolayers.

Okada *et al.* first presented the 0º and 180º oriented domains for WS_2 grown on hBN *via* PVT,[15] followed by Yu *et al.* who demonstrated the epitaxial growth of MoS_2 on hBN *via* PVT showing these two oriented domains in approximately equal number similar to that obtained for growth on sapphire.[5] However, Fu *et al.* observed up to 98% preferred orientation for monolayer MoS_2 domains grown on hBN by molecular beam epitaxy (MBE).[21] Subsequent first-principles

calculations reported by Zhang *et al*. proposed that the orientation selectivity originates from single-atom vacancies on the hBN surface that act as nucleation sites and break the nearly degenerate 0/180º domain orientations.[22] Achieving a single preferred orientation of TMD domains on hBN is highly desired to reduce the density of IDBs in coalesced epitaxial films, however, little is known about the origin and nature of the single atom vacancies in hBN responsible for this behavior. In addition, the ability to harness these defects to control both the nucleation density and orientation of TMD monolayer domains is highly desired as a pathway to achieve high quality single crystal monolayers over large areas *via* coalescence of individual domains.

In this chapter, we investigate the mechanism of defect-controlled domain alignment of 2D TMDs on hBN using a combination of experimental studies and first-principles calculations. The results provide experimental evidence that single-atom vacancies in hBN trap W atoms and thereby act as nucleation sites that break the symmetry and selectively stabilize a single preferred WSe_2 domain orientation. Subsequent coalescence of the WSe_2 domains leads to monolayer films with reduced IDBs and enhanced photoluminescence and transport properties thereby demonstrating the significant benefits of hBN as a substrate or template layer for TMD epitaxy.

3.2 Preferential domain orientation and defect control nucleation of WSe_2 on BN

WSe_2 monolayer films were grown by a multi-step process in a gas source CVD reactor at 800 ºC using $W(CO)_6$ and H_2Se in a H_2 carrier gas.[6] Single crystal hBN flakes exfoliated from bulk crystals onto c-plane sapphire ((0001) α-Al_2O_3) were used as substrates. In this case, a short 20 min growth time was used to achieve separated WSe_2 domains. The WSe_2 triangular domains grow epitaxially on the mechanically exfoliated hBN surface with only two orientations (Fig. 3-1a), with

the majority of the domains (~84%) exhibiting a single orientation, and the remainder inversely oriented (Fig. 3-1b). This is different than previous growth outcomes of TMD monolayers on c-plane sapphire where the epitaxial domains show 0º and 180º oriented domains with nearly equal proportion.[6,7] To directly inspect the structure of laterally stitched regions, a partially-coalesced WSe_2 monolayer on an hBN flake was transferred onto a transmission electron microscopy (TEM) grid and an area with two types of merging domains – between the same (region A in Fig. 3-1c) and inverse (region B) orientations – was identified by scanning TEM (STEM). Figure 3-1d shows the high angle annular dark field (HAADF-) STEM image (top) and corresponding inverse fast Fourier transform (FFT) image (after selecting only the WSe_2 FFT spots, bottom) of region A, demonstrating a continuous WSe_2 lattice on hBN stitched seamlessly between the two domains with the same orientation. In contrast, the HAADF-STEM image (top) and corresponding inverse FFT image (bottom) of region B in Fig. 3-1e clearly shows the formation of an IDB between two domains with 0º and 180º orientation. An atomic resolution HAADF-STEM image along the IDB shows 4|8 ring motifs (Fig. 3-2), consistent with a previous report.[8] This demonstrates that the density of IDBs can be minimized by maximizing the orientational uniformity of WSe_2 on hBN, in which case stitching across same-orientation domains would not be troubled by translationally offset grain boundaries and would not leave an unclosed gap inaccessible to incoming source molecules.

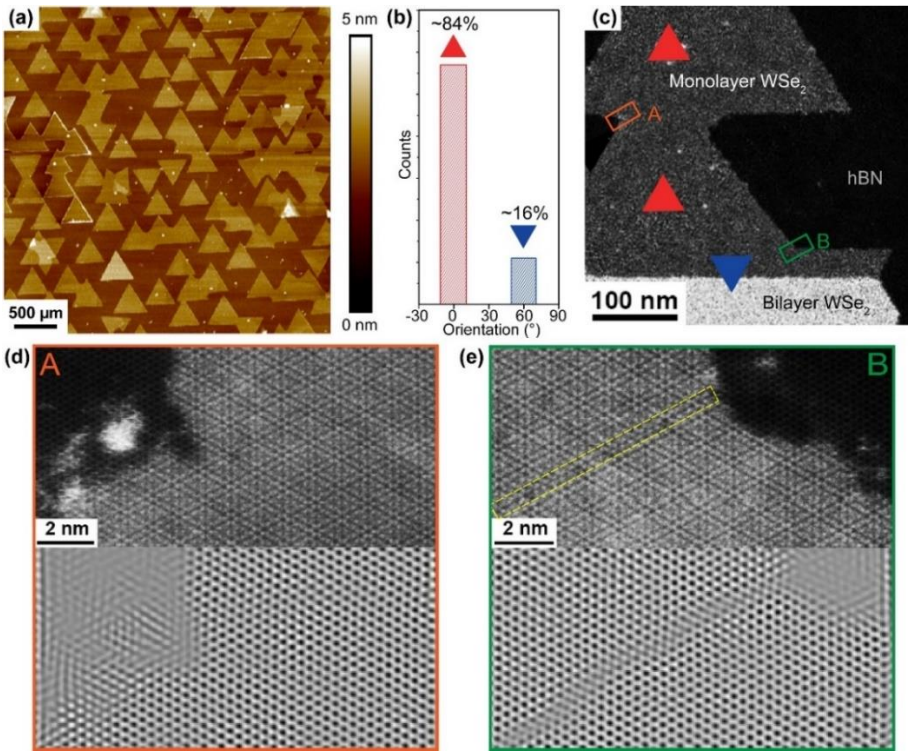

Figure 3- 1 (a) AFM image of epitaxial WSe_2 domains on hBN. (b) Orientation histogram of 0° and 180° oriented WSe_2 domains on hBN. (c) ADF-STEM image of region with two types of merging domains. (d) HAADF-STEM image (top) and corresponding inverse FFT image (bottom) of region A in (c) showing no grain boundary formed between two domains with same orientation. (e) HAADF-STEM image (top) and corresponding inverse FFT image (bottom) of region B in (c) showing inversion domain boundary formed between two domains with 0° and 180° orientation.

First-principle calculations previously carried out for MoS_2 growth on hBN suggest the preferred orientation arises from single-atom vacancies on the hBN surface that lift the 0/180° degeneracy and stabilize one orientation against its inverse.[22] In addition, this mechanism also offers a pathway to control the nucleation density of TMD domains on the surface.

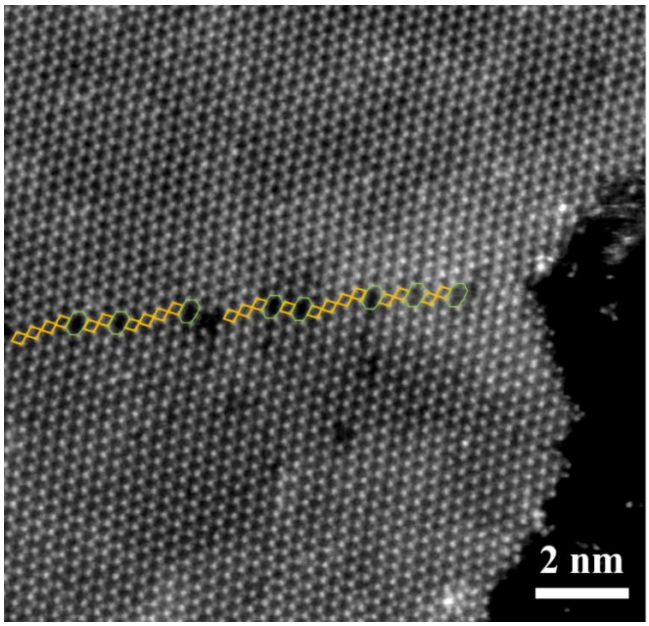

Figure 3- 2 HAADF-STEM image of WSe_2 on BN, the anti-phase grain boundary between the 0º and 60º domains contains 4|8 rings highlighted in the image. It is noted that a slight sample tilt and high contrast are applied in the imaging condition to blur the information of underlying BN and the corresponding Moiré patterns between WSe_2 and BN, which help identify the WSe_2 lattice.

3.3 Transmission electron microscopy investigation of detect controlled nucleation of WSe_2/BN heterostacks

To probe the role of defects in nucleation and orientation, samples were prepared using hBN flakes transferred directly onto the TEM grid and then exposed to W species only in the gas source CVD system using a 30 s pulse of $W(CO)_6$ at 800 ºC. The defect-assisted nucleation model described previously predicts the presence of an interstitial transition metal "glue" atom at the single atom vacancies on the hBN surface which controls the nucleation and orientation of the TMD on the point defect site.[22] The same defect-mediated distinction between 0/180º stacking in WSe_2 calculated from DFT using an 8 × 8 hBN + 6 × 6 WSe_2 supercell is 0.90 eV, where the "eclipsed" configuration[22] (top and side view in Fig. 3-3a) is more stable; the "staggered" configuration[22] that would nucleate a domain with inverse orientation is unfavorable and suppressed. Compared to Fig.

3-3b, which shows the bare ultra-thin hBN flake with surface defects of one kind (V_B or V_N), the HAADF-STEM image after W exposure in Fig. 3-3c shows a single W atom stably trapped on the hBN surface at a single vacancy site. Furthermore, direct growth of tiny WSe_2 domains on the hBN on a TEM grid was carried out under 30 s nucleation and 5 min ripening. In the corresponding STEM image shown in Fig. 3-3d, a brighter imaged defect is visible which is consistent with the glue W atom between WSe_2 and the underlying hBN. The WSe_2 domain also has inevitably formed defects such as V_{Se} and V_{Se2}. In all of the WSe_2 domains examined, the glue W atoms appear within 3-5 nm of the center of the domain. This offset from the exact domain center likely arises from the fact that during the very early stages of growth, the domain may not grow at the same rate in all directions due to differences in edge stability and variations in precursor flux. To further test if the imaged glue W atoms are interstitials trapped at substrate defects instead of adatoms on top of WSe_2, we compare the energy landscape of W atoms on WSe_2 with typical knock-on energies from the imaging electron beam. Using nudged elastic band calculations at the DFT level, the migration barrier of a surface W adatom is found to be 0.4 eV (between the ground state at the metal site and the metastable state at the hollow site, as shown in Fig. 3-3e); the migration barrier of a W adatom between WSe_2 and pristine hBN should be similar (according to similar migration barriers for metal adatoms on monolayer TMDs and inside bulk TMDs).[23] Assuming relativistic binary collisions, the 80 keV electron beam can transfer up to 1.0 eV kinetic energy to a W atom, sufficient for a surface adatom to hop between lattice sites. In addition, metal atom migration on TMDs has been previously reported under similar imaging conditions (80 keV).[24] Since hopping events were not seen over the duration of 10 min during STEM scanning, the imaged point-defects are unlikely to be mobile adatoms or interstitials and are likely trapped interstitials at vacancy sites in the hBN substrate.

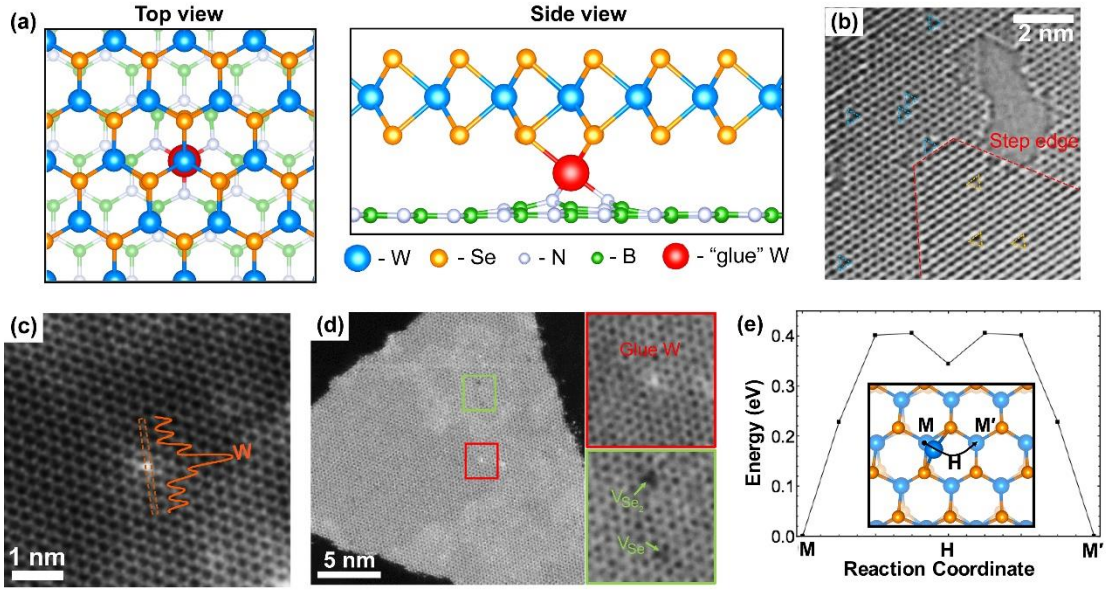

Figure 3- 3 (a) Top and side view of the relaxed DFT structure of a W interstitial atom (red) sandwiched between pristine WSe_2 and a boron vacancy in hBN. (b) HRTEM images of monolayer to multilayer pristine hBN at 80 kV with a monochromated electron source; the intrinsic vacancies in BN is mostly V_N on the surface, which is also shown at the other side of the step edge. (c) HAADF-STEM image of a single W atom trapped at hBN surface after seeding process (30 s of $W(CO)_6$ flow at 800 ºC), the overlay on the plot is the corresponding imaging intensity near the single W atom. (d) HAADF-STEM image of a brighter imaged defect indicating the glue W atom between WSe_2 and the underlying BN (red, top right). The WSe_2 domain also has inevitably formed defects such as V_{Se} and V_{Se2} (green, bottom right). (e) The migration barrier of a W adatom on a WSe_2 surface between the ground state at the (Metal) site and the metastable state at the (Hollow) site is 0.4 eV from a nudged elastic band calculation.

3.4 Coalesce WSe_2 monolayer film formation *via* defect formation and annealing.

The fact that WSe_2 nucleation is determined by point defects on the hBN surface motivates a defect-assisted growth mechanism for vdW epitaxy whereby the nucleation density can be controlled by manipulating surface defect density. In order to test this, He plasma treatment at a power energy of 50 W was employed to intentionally introduce surface defects on the hBN/sapphire substrates. Figure 3-4a shows the SEM images of WSe_2 grown with 30 s nucleation and 10 min ripening on pristine hBN, hBN treated by 1 s He plasma, and hBN treated by 15 s He plasma,

respectively. The short 1 s plasma treatment has already created a large number of defects on the hBN surface that significantly increases the WSe_2 domain density while still maintaining the epitaxial growth. Similarly, STEM results also show a consistently increasing density of glue atoms trapped at the defective surface which act as seeding sites (Fig. 3-5). Note that W atoms are always trapped at one set of BN lattices where either V_B or V_N forms, supporting the result of the single preferred orientation growth of WSe_2 domains. The WSe_2 domains also start losing the character of single preferred orientation after the 1 s plasma treatment, possibly because both B and N single atom vacancies were created simultaneously during the plasma treatment. Longer plasma treatment can further increase the nucleation density but also heavily damages the hBN surface and introduces other structural defects that results in island growth (multilayer domains) and loss of epitaxy (Fig. 3-4)

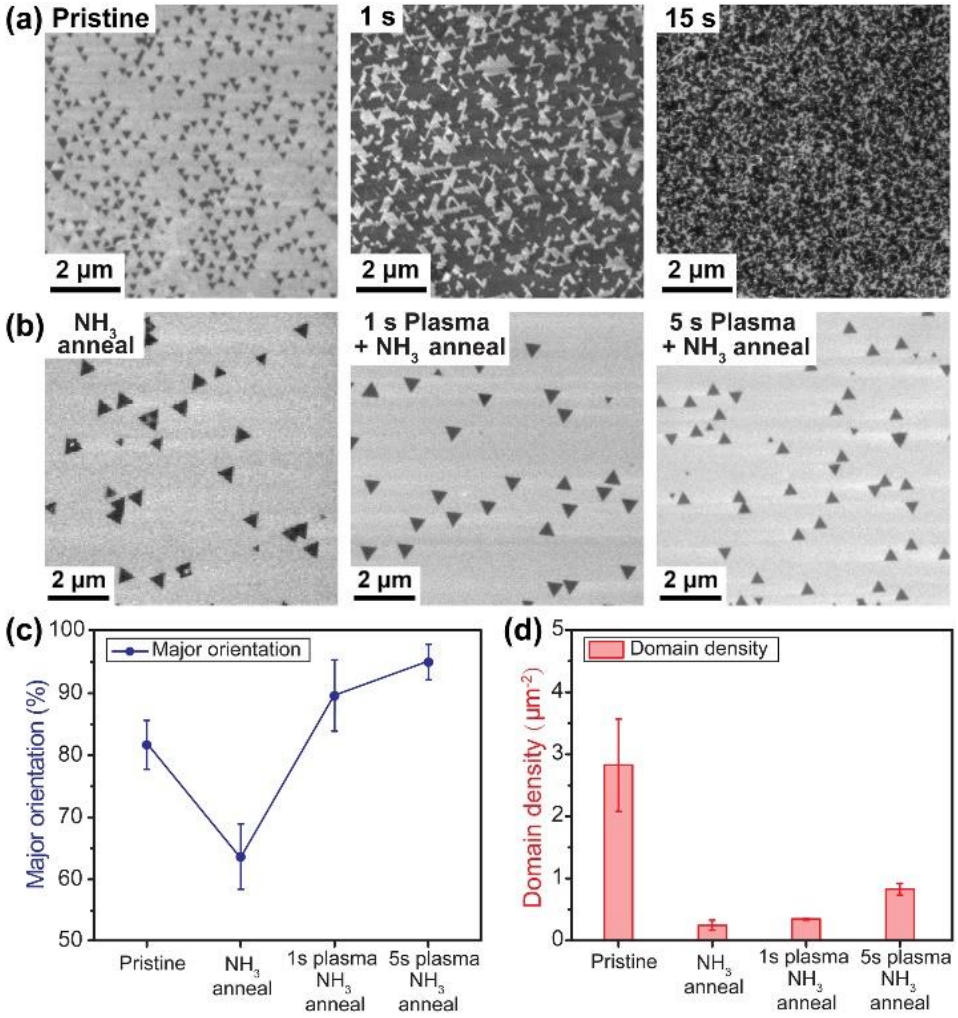

Figure 3- 4 (a) SEM images from left to right showing WSe_2 grown on pristine hBN, hBN treated by 1 s He plasma at 50 W, and hBN treated by 15 s He plasma at 50W respectively. (b) SEM images from left to right showing WSe_2 grown on hBN annealed in NH_3 at 1100 ºC for 30 min, hBN first treated by 1 s He plasma at 50 W then annealed in NH_3 at 1100 ºC for 30 min, and hBN first treated by 5 s He plasma at 50W then annealed in NH_3 at 1100 ºC for 30 min respectively. (c) Measured percentage of major domain orientation of WSe_2 domains grown on hBN surfaces under different treatment. (d) Measured nucleation density of WSe_2 domains grown on hBN surfaces under different treatment.

In order to controllably create single atom vacancies of only one element, the plasma treated hBN surfaces were further annealed in NH_3 at 1100 ºC for 30 min to reduce the concentration of N single atom vacancies. In this case, most of the N vacancies should be healed and B vacancies should be the majority on the hBN surface. Figure 3-4b shows SEM images of

WSe_2 grown with 30 s nucleation and 10 min ripening on three types of hBN: hBN annealed in NH_3, hBN first treated by 1 s He plasma at 50 W then annealed in NH_3, and hBN first treated by 5 s He plasma at 50W then annealed in NH_3. All annealing processes were performed at 1100 ºC for 30 min. When compared to WSe_2 grown on pristine hBN, both domain density and percentage of major domain orientation decrease for WSe_2 grown on the NH_3 annealed hBN surface (Figs. 3-4c and d). Native B and N vacancies should exist on pristine hBN while N single atom vacancies are expected to be the major native defects due to their lower formation energy.[25,26] By healing most of N vacancies during the NH_3 annealing, the total single atom vacancy density decreases, resulting in a decreased density of WSe_2 domains. However, not all N vacancies are expected to be healed and some N vacancies can even reform under the high temperature (800 ºC) and H_2-rich environment during the WSe_2 growth process. In this case, the similar density of N and B vacancies results in the inverse orientations and thus decreases the percentage of major domain orientation. It is also possible that N antisite defects (N sitting on B vacancy) could form under NH_3 annealing, however we do not observe a distinctive peak at ~ 623 nm in the room temperature photoluminescence spectra of the NH_3 annealed WSe_2/hBN sample which is associated with antisite defects.[27] Consequently, the decrease in nucleation density is likely not related to a decrease in B vacancies *via* formation of antisite defects during the NH_3 annealing process.

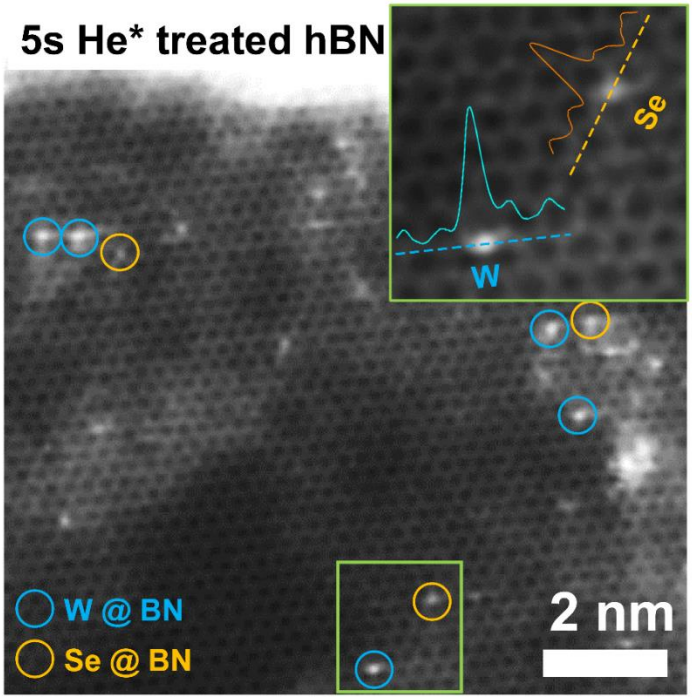

Figure 3- 5 HAADF-STEM image of W and Se atoms trapped at hBN surface after growth process (with 5 s He plasma treated BN substrate), the overlay plots are the corresponding imaging intensity near the single W (blue) and Se (orange) atoms; respectively. A large number of single atoms can be trapped at the defective surface and act as seeding sites for WSe_2 growth on BN. It is clearly shown in the image that W and Se trapped atoms can be simply distinguished by intensity due to Z-contrast imaging mechanism in STEM. We also notice that the W always trap at one set of lattices (either V_B or V_N) and Se always trap at the other. Such selectivity leads to the preferred orientation growth of WSe_2 domains.

In comparison, on the hBN surface that was first treated by 1 s He plasma then annealed in NH_3, both domain density and the percentage of major domain orientation WSe_2 increase due to the additional B single atom vacancies formed at the hBN surface from the plasma treatment (Figs. 3-4c and d). By further increasing the plasma treatment time to 5 s, a 95% major orientation (Fig. 3-4c) and ~0.9 μm^{-2} domain density can be achieved. Ideally, 100% single orientation can be approached by further removing steps, wrinkles and other defects in the hBN and suppressing N vacancy formation with in-situ NH_3 annealing. This defect-assisted nucleation introduces a useful way to control both the density and orientation of nuclei when establishing vdW epitaxial growth.

The growth rate of the WSe_2 domains on hBN can be determined for a particular set of growth conditions by varying the lateral growth time. The area of individual WSe_2 domains (Fig. 3-6a) and the overall surface coverage of WSe_2 (Fig. 3-6b) increase linearly as the lateral growth time is varied from 10, 15, 30, 60 to 90 min. This indicates that the precursors likely contribute to lateral growth of existing monolayer domains, rather than nucleating new domains.

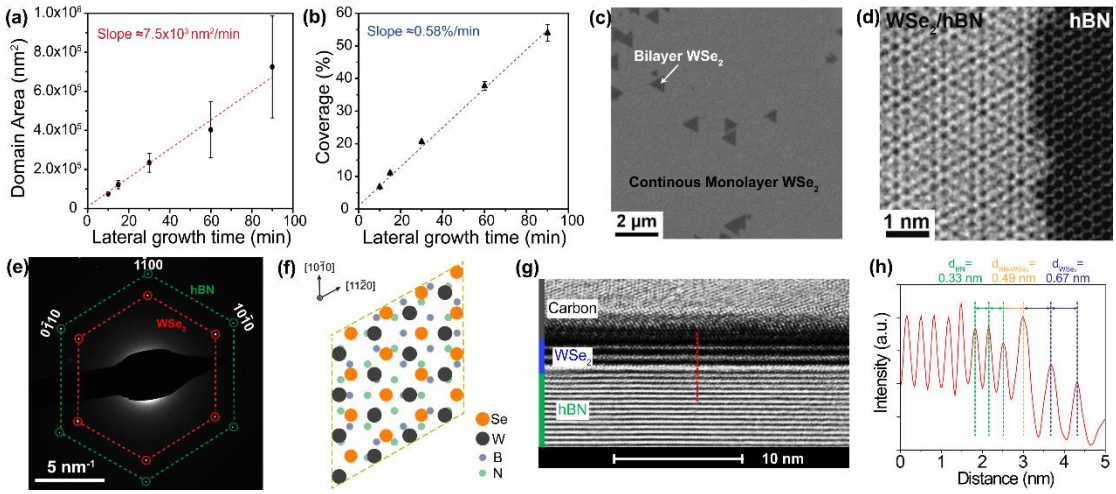

Figure 3- 6 (a) WSe_2 monolayer domain area on hBN as a function of lateral growth time. The slope shows a linear growth rate of 7.5 × 103 nm^2/min. (b) WSe_2 monolayer coverage on hBN as a function of lateral growth time. The slope shows a linear growth rate of 0.58 %/min. (c) SEM image of coalesced monolayer WSe_2 film on hBN. (d) Atomic resolution HAADF-STEM image showing the Moiré pattern of WSe_2 on hBN. (e) SAED pattern showing the epitaxial relationship between WSe_2 and hBN. (f) Schematic illustrating 3 × 3 WSe_2 unit cells on 4 × 4 hBN. (g) Cross-sectional HRTEM image of the WSe_2 film on hBN showing a clear WSe_2 and hBN interface. (h) Intensity profile of the red dot line in (e) showing the interlayer spacing of hBN-hBN, hBN-WSe_2, and WSe_2-WSe_2 are 0.33 nm, 0.49 nm, and 0.67 nm respectively.

With appropriate nucleation density of WSe_2 achieved by plasma treatment and NH_3 annealing on hBN, continued lateral growth of the initial domains eventually leads to coalescence into a continuous monolayer film. Figure 3-6c shows a SEM image of a fully coalesced monolayer WSe_2 film on an hBN flake. The dark triangular domains in Fig. 3-6c are additional bilayer domains of WSe_2. These bilayer domains possibly arise from additional nucleation at intrinsic defects in the

WSe_2 monolayer. Figure 3-6d shows an atomic resolution HAADF-STEM image of WSe_2 on hBN. The Moiré patterns of the WSe_2/hBN region and the hexagonal crystal structure of the hBN-only region at the edge indicate an epitaxial growth of monolayer WSe_2 on hBN. The selected area electron diffraction (SAED) pattern of the film shown in Fig. 3-6e identifies the in-plane epitaxial relationship as $(1\bar{1}00)$ WSe_2 ‖ $(1\bar{1}00)$ hBN with 0° misorientation. Based on the Moiré patterns and the lattice constants of WSe_2 and hBN, the mismatch can be reduced to 1.5% for 3 × 3 WSe_2 unit cells on 4 × 4 hBN (schematic in Fig. 3-6f).

Cross-sectional TEM was also performed on a coalesced WSe_2/hBN sample to further understand the interface between WSe_2 and hBN. A region that contained a tri-layer domain of WSe_2 was selected to clearly distinguish the interlayer spacing. In Fig. 3-6g, the regions of hBN, WSe_2, and the carbon protection layer can be distinguished by the crystal structure and interlayer distance. The first layer of WSe_2 shows the highest intensity since it is a fully coalesced monolayer that spans the entire sample thickness while the second and third layers which are from a portion of an isolated domain have lower intensity. A clear and sharp interface between WSe_2 and hBN indicates vdW epitaxy occurs with no additional passivating layer. This is different than growth of WSe_2 on sapphire where an extra Se passivating layer and strong WSe_2-substrate bonding at step edges on the sapphire surface were found.[31] In addition, a variation of interlayer distance at the WSe_2/hBN interface was also observed. Figure 3-6h depicts the intensity profile of the red dot line section in Fig. 3-6g. Based on the intensity profile, the interlayer spacing of hBN-hBN and WSe_2-WSe_2 were measured as 0.33 nm and 0.67 nm, respectively. The spacing between WSe_2/hBN, however, was measured as 0.49 nm, which is nearly identical to the arithmetic mean of the hBN-hBN and WSe_2-WSe_2 spacings. This is consistent with the 0.51 nm hBN-WSe_2 spacing calculated from DFT.[28,29]

3.5 Optical and electronic properties of Coalesced WSe_2 monolayer films on BN

Photoluminescence spectroscopy is an effective way to optically probe exciton-related emission and defect states in semiconducting TMDs.[30,31] Figure 3-7a shows the PL spectra of coalesced WSe_2/hBN/sapphire and WSe_2/sapphire samples grown under identical conditions using the same power of 488 nm laser excitation. The results show an over 50 × enhancement in PL response for WSe_2/hBN compared to WSe_2/sapphire. In addition, the 1.65 eV PL peak position is uniform across the 5 × 5 μm measured area from the WSe_2/hBN as shown in Fig. 3-7b. In contrast, the PL peak position varied from 1.58 eV to 1.64 eV across the WSe_2/sapphire sample. This improvement can be attributed to the screening effect of the hBN substrate which suppresses the effects of charged impurities and substrate phonons thereby preserving the intrinsic properties of WSe_2.[13,32,33] In comparison, the WSe_2 film on sapphire is affected by several factors including strain and substrate steps, which lead to non-uniformity in PL peak position and a decrease in PL intensity.

To further investigate and compare the optical properties of monolayer WSe_2/hBN and WSe_2/sapphire, we acquired a series of temperature-dependent PL spectra from 300 K to 80 K (Figs. 3-7c and d, respectively). At higher temperature (above 200 K for WSe_2/hBN, and above 240 K for WSe_2/sapphire), the PL spectra exhibit a symmetrical single-peak, indicating the dominance of neutral exciton (X^0) emission in the higher temperature regime.[34] With the decrease of temperature, a low-energy shoulder emerges in the PL spectra for both samples, which can be assigned as negative trion (X^-) emission with a trion binding energy (E_{X-}) ~ 30 meV. Remarkably, in the case of WSe_2/hBN, the X^0 and X^- peaks significantly sharpen and enhance at low

temperatures, resulting in clearly resolved exciton emission (FWHM = 18.6 meV) and trion emission (FWHM = 38.5 meV) at 80 K (Fig. 3-8). The FWHM values of both the exciton and trion emission are comparable to the emission spectra at 77 K[30] and 4 K[35] reported for WSe_2/hBN heterostructures formed by exfoliation from bulk single crystals. This indicates that the optical properties of monolayer WSe_2 grown by gas source CVD on hBN in this work are comparable to that of single crystal flakes, especially considering that the reported samples either consisted of WSe_2 encapsulated in between two hBN flakes (removing the impact of the environment)[51] or were characterized at lower temperature (further reducing linewidth broadening by reducing phonon scattering).[35,36] In addition, no obvious defect-bound exciton (X^B) emission was observed in the monolayer WSe_2/hBN sample, indicating that the crystalline quality of WSe_2 was high when compared to other CVD processes.[30]

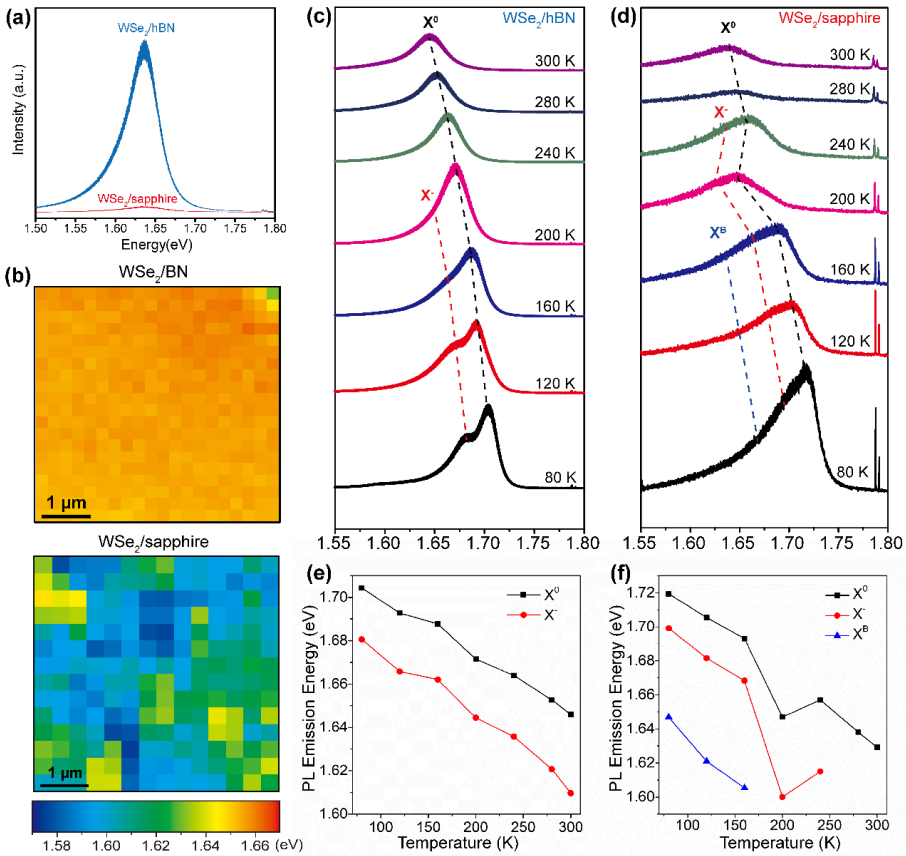

Figure 3- 7 (a) PL spectra showing an over 50 × enhancement in intensity for WSe_2/hBN compared to WSe_2/sapphire. (b)5 µm × 5 µm PL maps of coalesced WSe_2/hBN showing a uniform PL peak position at 1.65 eV (top) compared to varied peak positions ranging from 1.58-1.64 eV for coalesced WSe_2/sapphire (bottom). (c)-(d) Temperature-dependent PL spectra of WSe_2/hBN and WSe_2/sapphire under 488 nm laser excitation, respectively. The measured temperature ranges for both samples are from 80 K to 300 K. (e)-(f) Plots of fitted PL emission peak energy of WSe_2/hBN and WSe_2/sapphire versus temperature, respectively.

In contrast, the WSe_2 film grown on sapphire exhibits broader PL emission at temperatures ranging from 80 K to 300 K. A broad X^B peak emerges in WSe_2/sapphire at temperatures below 160 K, causing the asymmetrical line-shape of PL emission. The fitting results of temperature-dependent PL emission peak position for both samples are plotted in Figs. 3-7e and f, which also indicate the consistent X^0 and X^- emissions of WSe_2 on hBN at different temperatures, and the emergence of X^B emissions from WSe_2 on sapphire at low temperature.

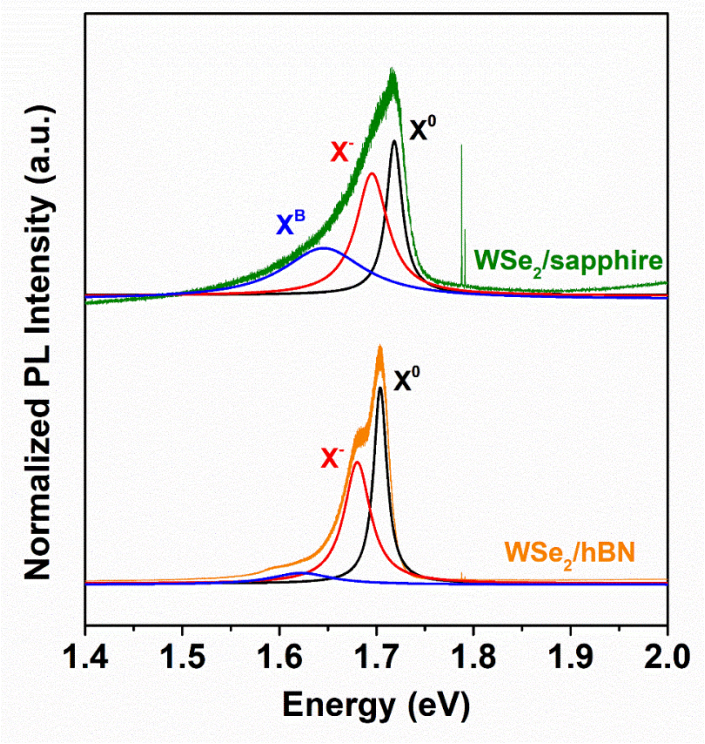

Figure 3- 8 Deconvoluted PL spectra of WSe_2/hBN and WSe_2/sapphire at 80 K. The deconvoluted spectra were acquired by performing multipeak Lorentzian fitting using three peak components: neutral exciton (X^0), trion (X^-) and defect-bound exciton (X^B).

The narrower PL linewidths and negligible X^B emission for WSe_2/hBN compared to WSe_2/sapphire may be attributed to two factors: (1) The direct synthesis on the atomically-flat hBN surface which leads to a higher crystal quality monolayer WSe_2 film that contains less defects and IDBs, thus decreasing emission from optically-active defect states; and (2) WSe_2 grown on sapphire suffers from the substrate-induced charge doping,[36] which leads to the inhomogeneous broadening of excitonic emissions. By in-situ synthesizing WSe_2 on hBN, the interaction between charged sapphire and WSe_2 can be isolated by the hBN flake, allowing access to the intrinsic optical quality of as-grown WSe_2 films.[37,38]

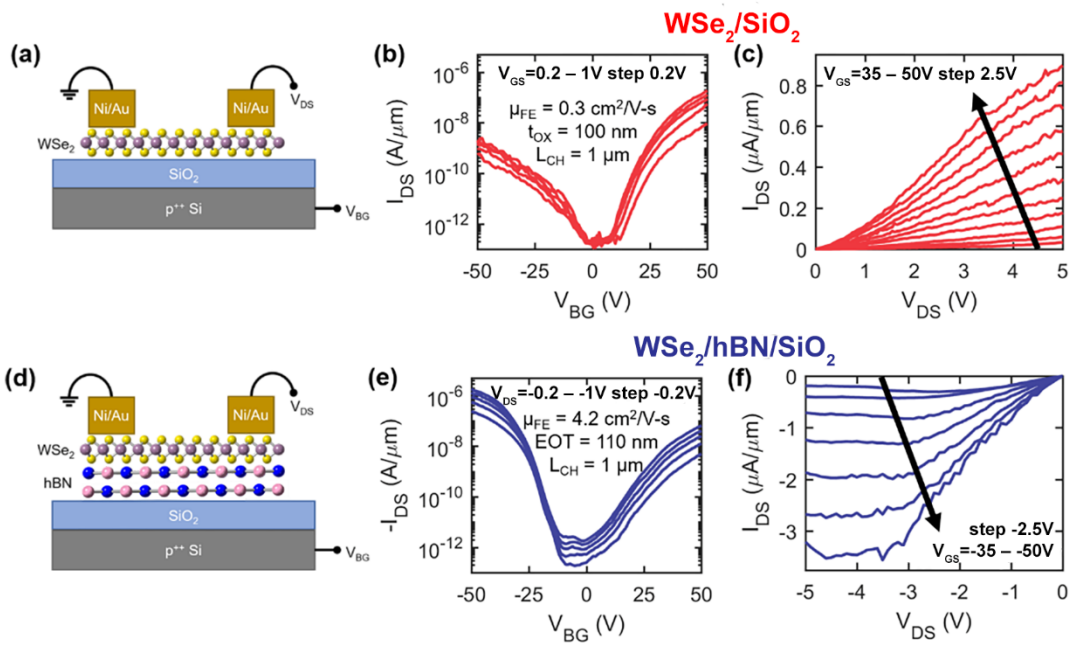

Figure 3- 9 Electrical FET characterization of transferred WSe_2 and transferred WSe_2/hBN on SiO_2/p^{++} Si. Schematic showing a back gated WSe_2 FETs (a) directly on 100 nm SiO_2 and (d) on 10 nm hBN on 100 nm SiO_2 on p^{++} Si with Ni contacts. (b, e) Drain current (I_{DS}) *versus* back gate voltage (V_{BG}) at various drain voltages (V_{DS}) with step of 0.2 V and (c, f) I_{DS} *versus* V_{DS} at various V_{BG} with step of 2.5 V for WSe_2 on SiO_2 and on hBN/SiO_2, respectively.

To characterize the electrical properties of both the WSe_2 grown on sapphire and on hBN, the films were removed from the sapphire substrates and transferred onto 100 nm SiO_2 on p^{++} Si

substrates. Back gated FETs (BGFETs) with a channel length (L_{CH}) of 1 µm and width (W) of 5 µm were fabricated as shown schematically in Figs. 3-9a and d, respectively. Note that for the growth on hBN, the entire WSe_2/hBN stack was subsequently transferred. In this case, the hBN thickness has been verified as ~10 nm by AFM. Figure 3-9b and e, show the transfer characteristics *i.e.* drain current (I_{DS}) *versus* back gate voltage (V_{BG}) for different drain voltages (V_{DS}) and Figs. 3-9c and f show the output characteristics *i.e.* I_{DS} *versus* V_{DS} for different V_{BG} for BGFETs based on WSe_2 grown on sapphire and hBN, respectively. Clearly, ambipolar transport *i.e.* the presence of a prominent electron branch current for $V_{BG} > 0$ V and hole branch current for $V_{BG} < 0$ V are observed for BGFETs based on WSe_2 grown on sapphire as seen in Fig. 3-9b. This ambipolar transport is a result of the contact metal (in this case Ni) Fermi level being pinned near the center of the WSe_2 bandgap allowing injection of electrons and holes into the conduction and the valence band, respectively, through the corresponding Schottky barriers.[39] However, since carriers must tunnel through relatively large Schottky barrier heights which are almost half the bandgap energy of WSe_2, the corresponding contact resistances for both electron and hole injections are large, limiting the ON state current as seen in the rectifying type behavior in Figure 7b. The field effect mobility extracted in the ON state from the peak transconductance, $\mu_{FE} = \frac{\partial I_{DS}}{\partial V_{GS}} \frac{L_{CH}}{C_G\, W\, V_{DS}}$, is severely underestimated in devices with Schottky barrier contacts.[40] For WSe_2 grown on sapphire, a contact limited electron μ_{FE} of ~0.3 cm^2/Vs was extracted (Fig. 3-10a).[40] The devices are slightly n-type with an electron to hole current ratio of ~100:1 indicative of Ni Fermi level pinning closer to the conduction band. Note that although in the literature there are reports of WSe_2 FETs with higher ON state currents and larger electron and hole μ_{FE}, these tend to use contact strategies engineered towards achieving primarily n-type or p-type devices at the expense of ambipolar characteristics which is achieved with the Ni contacts used in this work.[41,42,43]

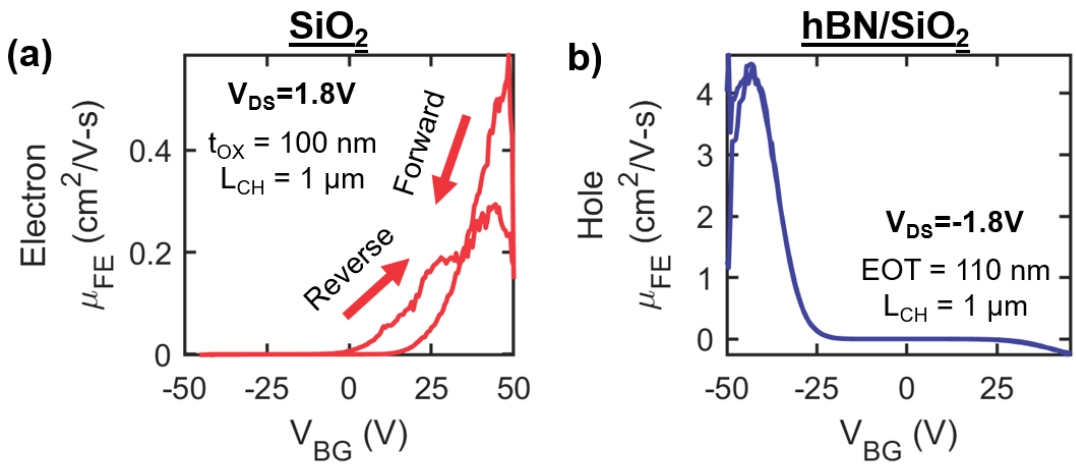

Figure 3- 10 Mobility extraction for WSe_2 on SiO_2 and hBN/SiO_2. (a,b) The field effect mobility (μ_{FE}) *versus* V_{BG} at V_{DS} = 1.8 V and V_{DS} = -1.8 V for WSe_2 on SiO_2 and on hBN/SiO_2, respectively. The mobility is derived from the peak transconductance method where $\mu_{FE} = \frac{\partial I_{DS}}{\partial V_{GS}} \frac{L_{CH}}{C_G\, W\, V_{DS}}$. For WSe_2 on SiO_2, the mobility ($\mu_{FE} \approx 0.2$ cm^2/V-s) is extracted from the reverse sweep direction (negative to positive V_{BG}) since interface trap discharging obscures the forward sweep characteristics. For WSe_2 on hBN/SiO_2, the large contact resistance causes the extracted μ_{FE} to decrease when V_{BG} < -43 V. Hence, the peak mobility of 4.2 cm^2/V-s is contact limited, underestimating the true hole mobility of the material.

For BGFETs based on WSe_2 grown on hBN, there is no observable threshold shift, confirming the growth on hBN has not induced any significant substrate doping effect. While the electron branch currents are similar to those on SiO_2, a dramatic 3 orders of magnitude increase in the hole branch currents is observed. This cannot be attributed to a simple change in the Fermi level pinning since an increase in the hole branch current would be accompanied by a decrease in the electron branch current. We hypothesize this hole branch improvement is due to a combination of factors. Part of the current increase can be attributed to an increase in the hole mobility, due to both a reduction in the IDBs as well as reduced interface scattering from the hBN *versus* SiO_2 interface. It is well known that hBN encapsulation of 2D materials improves the mobility, often by orders of magnitude, and reduces the interface states which can cause device hysteresis and degraded subthreshold slopes. [44,45,46] Second, since the WSe_2 is monolayer, the hBN substrate may influence

how the WSe_2 hybridizes with the Ni contact in such a way that hole injection has been facilitated. The charge injection from the contact into the WSe_2 can occur through a combination of many mechanisms and strongly depends on interface with the metal contact.[47] We notice these results are contrary to recent reports which show devices on hBN have reduced hole branch currents compared to on SiO_2.[48] The hole μ_{FE} extracted from these devices was 4.2 cm^2/V-s (Fig. 3-10b); however, this is likely contact limited since the I_{DS} *versus* V_{DS} characteristics in Fig. 3-9f show rectifying type behavior.[40] These results demonstrate that WSe_2 growth on hBN is an effective means to improve the hole transport characteristics and tune FET devices to be ambipolar or p-type.

3.6 Chapter Summary

In this chapter, we demonstrated a defect-controlled nucleation and orientation process for controllable epitaxial growth of single crystal WSe_2 monolayers on single crystal hBN flakes. By appropriate plasma treatment and NH_3 annealing, the density of single atom vacancies on the hBN surface, and consequently the nucleation density of single oriented WSe_2, can be controlled. The mechanism of this defect-controlled 2D heterostructure growth was investigated through first principles calculations and TEM characterization. A single crystal monolayer film was eventually achieved *via* coalescence of the initial domains with extended growth time. PL and electrical measurements show enhanced optical and transport properties, respectively, for the monolayer WSe_2 film grown on hBN compared to sapphire. Considering that wafer-scale single crystalline hBN has recently been demonstrated through a CVD method employing a liquid gold substrate,[49] our results clearly show the potential of hBN as a substrate or template layer for epitaxial growth of high quality single crystal monolayer TMD films.

3.7 References

1. Shi, Y.; Zhou, W.; Lu, A.-Y.; Fang, W.; Lee, Y.-H.; Hsu, A. L.; Kim, S. M.; Kim, K. K.; Yang, H. Y.; Li, L.-J., van der Waals epitaxy of MoS_2 layers using graphene as growth templates. *Nano letters* **2012,** *12* (6), 2784-2791.

2. Bianco, G.; Losurdo, M.; Giangregorio, M.; Sacchetti, A.; Prete, P.; Lovergine, N.; Capezzuto, P.; Bruno, G., Direct epitaxial CVD synthesis of tungsten disulfide on epitaxial and CVD graphene. *RSC Advances* **2015,** *5* (119), 98700-98708.

3. Eichfeld, S. M.; Hossain, L.; Lin, Y.-C.; Piasecki, A. F.; Kupp, B.; Birdwell, A. G.; Burke, R. A.; Lu, N.; Peng, X.; Li, J., Highly scalable, atomically thin WSe_2 grown via metal–organic chemical vapor deposition. *ACS nano* **2015,** *9* (2), 2080-2087.

4. Yan, A.; Velasco Jr, J.; Kahn, S.; Watanabe, K.; Taniguchi, T.; Wang, F.; Crommie, M. F.; Zettl, A., Direct growth of single-and few-layer MoS_2 on h-BN with preferred relative rotation angles. *Nano letters* **2015,** *15* (10), 6324-6331.

5. Yu, H.; Yang, Z.; Du, L.; Zhang, J.; Shi, J.; Chen, W.; Chen, P.; Liao, M.; Zhao, J.; Meng, J., Precisely Aligned Monolayer MoS_2 Epitaxially Grown on h-BN basal Plane. *Small* **2017,** *13* (7), 1603005.

6. Dumcenco, D.; Ovchinnikov, D.; Marinov, K.; Lazic, P.; Gibertini, M.; Marzari, N.; Sanchez, O. L.; Kung, Y.-C.; Krasnozhon, D.; Chen, M.-W., Large-area epitaxial monolayer MoS_2. *ACS nano* **2015,** *9* (4), 4611-4620.

7. Zhang, X.; Choudhury, T. H.; Chubarov, M.; Xiang, Y.; Jariwala, B.; Zhang, F.; Alem, N.; Wang, G.-C.; Robinson, J. A.; Redwing, J. M., Diffusion-controlled epitaxy of large area coalesced

WSe_2 monolayers on sapphire. *Nano letters* **2018,** *18* (2), 1049-1056.

8. Van Der Zande, A. M.; Huang, P. Y.; Chenet, D. A.; Berkelbach, T. C.; You, Y.; Lee, G.-H.; Heinz, T. F.; Reichman, D. R.; Muller, D. A.; Hone, J. C., Grains and grain boundaries in highly crystalline monolayer molybdenum disulphide. *Nature materials* **2013,** *12* (6), 554.

9. Zou, X.; Liu, Y.; Yakobson, B. I., Predicting dislocations and grain boundaries in two-dimensional metal-disulfides from the first principles. *Nano letters* **2012,** *13* (1), 253-258.

10. Ly, T. H.; Perello, D. J.; Zhao, J.; Deng, Q.; Kim, H.; Han, G. H.; Chae, S. H.; Jeong, H. Y.; Lee, Y. H., Misorientation-angle-dependent electrical transport across molybdenum disulfide grain boundaries. *Nature communications* **2016,** *7*, 10426.

11. Du, L.; Yu, H.; Xie, L.; Wu, S.; Wang, S.; Lu, X.; Liao, M.; Meng, J.; Zhao, J.; Zhang, J., The Effect of Twin Grain Boundary Tuned by Temperature on the Electrical Transport Properties of Monolayer MoS_2. *Crystals* **2016,** *6* (9), 115.

12. Zhou, S.; Wang, S.; Shi, Z.; Sawada, H.; Kirkland, A. I.; Li, J.; Warner, J. H., Atomically sharp interlayer stacking shifts at anti-phase grain boundaries in overlapping MoS_2 secondary layers. *Nanoscale* **2018,** *10* (35), 16692-16702.

13. Man, M. K.; Deckoff-Jones, S.; Winchester, A.; Shi, G.; Gupta, G.; Mohite, A. D.; Kar, S.; Kioupakis, E.; Talapatra, S.; Dani, K. M., Protecting the properties of monolayer MoS_2 on silicon based substrates with an atomically thin buffer. *Scientific reports* **2016,** *6*, 20890.

14. Lin, Y.-C.; Jariwala, B.; Bersch, B. M.; Xu, K.; Nie, Y.; Wang, B.; Eichfeld, S. M.; Zhang, X.; Choudhury, T. H.; Pan, Y., Realizing large-scale, electronic-grade two-dimensional semiconductors. *ACS nano* **2018,** *12* (2), 965-975.

15. Okada, M.; Sawazaki, T.; Watanabe, K.; Taniguch, T.; Hibino, H.; Shinohara, H.; Kitaura, R., Direct chemical vapor deposition growth of WS_2 atomic layers on hexagonal boron nitride. *ACS nano* **2014,** *8* (8), 8273-8277.

16. Kretinin, A.; Cao, Y.; Tu, J.; Yu, G.; Jalil, R.; Novoselov, K.; Haigh, S.; Gholinia, A.; Mishchenko, A.; Lozada, M., Electronic properties of graphene encapsulated with different two-dimensional atomic crystals. *Nano letters* **2014,** *14* (6), 3270-3276.

17. Mayorov, A. S.; Gorbachev, R. V.; Morozov, S. V.; Britnell, L.; Jalil, R.; Ponomarenko, L. A.; Blake, P.; Novoselov, K. S.; Watanabe, K.; Taniguchi, T., Micrometer-scale ballistic transport in encapsulated graphene at room temperature. *Nano letters* **2011,** *11* (6), 2396-2399.

18. Ma, N.; Jena, D., Charge scattering and mobility in atomically thin semiconductors. *Physical Review X* **2014,** *4* (1), 011043.

19. Wierzbowski, J.; Klein, J.; Sigger, F.; Straubinger, C.; Kremser, M.; Taniguchi, T.; Watanabe, K.; Wurstbauer, U.; Holleitner, A. W.; Kaniber, M., Direct exciton emission from atomically thin transition metal dichalcogenide heterostructures near the lifetime limit. *Scientific reports* **2017,** *7* (1), 12383.

20. Hoshi, Y.; Kuroda, T.; Okada, M.; Moriya, R.; Masubuchi, S.; Watanabe, K.; Taniguchi, T.; Kitaura, R.; Machida, T., Suppression of exciton-exciton annihilation in tungsten disulfide monolayers encapsulated by hexagonal boron nitrides. *Physical Review B* **2017,** *95* (24), 241403.

21. Fu, D.; Zhao, X.; Zhang, Y.-Y.; Li, L.; Xu, H.; Jang, A.-R.; Yoon, S. I.; Song, P.; Poh, S. M.; Ren, T., Molecular beam epitaxy of highly crystalline monolayer molybdenum disulfide on hexagonal boron nitride. *Journal of the American Chemical Society* **2017,** *139* (27), 9392-9400.

22. Zhang, F.; Wang, Y.; Erb, C.; Wang, K.; Moradifar, P.; Crespi, V. H.; Alem, N., Full orientation control of epitaxial MoS_2 on hBN assisted by substrate defects. *Physical Review B* **2019,** *99* (15), 155430.

23. Komsa, H.-P.; Krasheninnikov, A. V., Native defects in bulk and monolayer MoS_2 from first principles. *Physical Review B* **2015,** *91* (12), 125304.

24. Lin, Y. C.; Dumcenco, D. O.; Komsa, H. P.; Niimi, Y.; Krasheninnikov, A. V.; Huang, Y.

S.; Suenaga, K., Properties of individual dopant atoms in single-layer MoS_2: atomic structure, migration, and enhanced reactivity. *Advanced materials* **2014,** *26* (18), 2857-2861.

25. Zobelli, A.; Ewels, C.; Gloter, A.; Seifert, G., Vacancy migration in hexagonal boron nitride. *Physical Review B* **2007,** *75* (9), 094104.

26. Wong, D.; Velasco Jr, J.; Ju, L.; Lee, J.; Kahn, S.; Tsai, H.-Z.; Germany, C.; Taniguchi, T.; Watanabe, K.; Zettl, A., Characterization and manipulation of individual defects in insulating hexagonal boron nitride using scanning tunnelling microscopy. *Nature nanotechnology* **2015,** *10* (11), 949.

27. Tran, T. T.; Bray, K.; Ford, M. J.; Toth, M.; Aharonovich, I., Quantum emission from hexagonal boron nitride monolayers. *Nature nanotechnology* **2016,** *11* (1), 37.

28. Zhang, X.; Al Balushi, Z. Y.; Zhang, F.; Choudhury, T. H.; Eichfeld, S. M.; Alem, N.; Jackson, T. N.; Robinson, J. A.; Redwing, J. M., Influence of carbon in metalorganic chemical vapor deposition of few-layer WSe_2 thin films. *Journal of Electronic Materials* **2016,** *45* (12), 6273-6279.

29. Goodisman, J., *Diatomic interaction potential theory: applications*. Academic Press: 2013.

30. Hünenberger, P. H.; van Gunsteren, W. F., Empirical classical force fields for molecular systems. In *Potential Energy Surfaces*, Springer: 1999; pp 177-214.

31. Carozo, V.; Wang, Y.; Fujisawa, K.; Carvalho, B. R.; McCreary, A.; Feng, S.; Lin, Z.; Zhou, C.; Perea-López, N.; Elías, A. L., Optical identification of sulfur vacancies: Bound excitons at the edges of monolayer tungsten disulfide. *Science advances* **2017,** *3* (4), e1602813.

32. Li, X.; Puretzky, A. A.; Sang, X.; KC, S.; Tian, M.; Ceballos, F.; Mahjouri-Samani, M.; Wang, K.; Unocic, R. R.; Zhao, H., Suppression of defects and deep levels using isoelectronic tungsten substitution in monolayer $MoSe_2$. *Advanced Functional Materials* **2017,** *27* (19), 1603850.

33. Wang, L.; Chen, Z.; Dean, C. R.; Taniguchi, T.; Watanabe, K.; Brus, L. E.; Hone, J.,

Negligible environmental sensitivity of graphene in a hexagonal boron nitride/graphene/h-BN sandwich structure. *ACS nano* **2012,** *6* (10), 9314-9319.

34. Jin, C.; Kim, J.; Suh, J.; Shi, Z.; Chen, B.; Fan, X.; Kam, M.; Watanabe, K.; Taniguchi, T.; Tongay, S., Interlayer electron–phonon coupling in WSe_2/hBN heterostructures. *Nature Physics* **2017,** *13* (2), 127.

35. Huang, J.; Hoang, T. B.; Mikkelsen, M. H., Probing the origin of excitonic states in monolayer WSe_2. *Scientific reports* **2016,** *6*, 22414.

36. Lippert, S.; Schneider, L. M.; Renaud, D.; Kang, K. N.; Ajayi, O.; Kuhnert, J.; Halbich, M.-U.; Abdulmunem, O. M.; Lin, X.; Hassoon, K., Influence of the substrate material on the optical properties of tungsten diselenide monolayers. *2D Materials* **2017,** *4* (2), 025045.

37. Dey, P.; Paul, J.; Wang, Z.; Stevens, C.; Liu, C.; Romero, A.; Shan, J.; Hilton, D.; Karaiskaj, D., Optical coherence in atomic-monolayer transition-metal dichalcogenides limited by electron-phonon interactions. *Physical review letters* **2016,** *116* (12), 127402.

38. Yu, Y.; Yu, Y.; Xu, C.; Cai, Y. Q.; Su, L.; Zhang, Y.; Zhang, Y. W.; Gundogdu, K.; Cao, L., Engineering Substrate Interactions for High Luminescence Efficiency of Transition-Metal Dichalcogenide Monolayers. *Advanced Functional Materials* **2016,** *26* (26), 4733-4739.

39. Cadiz, F.; Courtade, E.; Robert, C.; Wang, G.; Shen, Y.; Cai, H.; Taniguchi, T.; Watanabe, K.; Carrere, H.; Lagarde, D., Excitonic linewidth approaching the homogeneous limit in MoS_2-based van der waals heterostructures. *Physical Review X* **2017,** *7* (2), 021026.

40. Das, S.; Appenzeller, J., WSe_2 field effect transistors with enhanced ambipolar characteristics. *Applied physics letters* **2013,** *103* (10), 103501.

41. Nasr, J. R.; Schulman, D. S.; Sebastian, A.; Horn, M. W.; Das, S., Mobility Deception in Nanoscale Transistors: An Untold Contact Story. *Advanced Materials* **2019,** *31* (2), 1806020.

42. Zhou, H.; Wang, C.; Shaw, J. C.; Cheng, R.; Chen, Y.; Huang, X.; Liu, Y.; Weiss, N. O.;

Lin, Z.; Huang, Y., Large area growth and electrical properties of p-type WSe_2 atomic layers. *Nano letters* **2014,** *15* (1), 709-713.

43. Fang, H.; Chuang, S.; Chang, T. C.; Takei, K.; Takahashi, T.; Javey, A., High-performance single layered WSe_2 p-FETs with chemically doped contacts. *Nano letters* **2012,** *12* (7), 3788-3792.

44. Liu, W.; Kang, J.; Sarkar, D.; Khatami, Y.; Jena, D.; Banerjee, K., Role of metal contacts in designing high-performance monolayer n-type WSe_2 field effect transistors. *Nano letters* **2013,** *13* (5), 1983-1990.

45. Wang, J. I.-J.; Yang, Y.; Chen, Y.-A.; Watanabe, K.; Taniguchi, T.; Churchill, H. O.; Jarillo-Herrero, P., Electronic transport of encapsulated graphene and WSe_2 devices fabricated by pick-up of prepatterned hBN. *Nano letters* **2015,** *15* (3), 1898-1903.

46. Illarionov, Y. Y.; Rzepa, G.; Waltl, M.; Knobloch, T.; Grill, A.; Furchi, M. M.; Mueller, T.; Grasser, T., The role of charge trapping in MoS_2/SiO_2 and MoS_2/hBN field-effect transistors. *2D Materials* **2016,** *3* (3), 035004.

47. Dean, C. R.; Young, A. F.; Meric, I.; Lee, C.; Wang, L.; Sorgenfrei, S.; Watanabe, K.; Taniguchi, T.; Kim, P.; Shepard, K. L., Boron nitride substrates for high-quality graphene electronics. *Nature nanotechnology* **2010,** *5* (10), 722.

48. Schulman, D. S.; Arnold, A. J.; Das, S., Contact engineering for 2D materials and devices. *Chemical Society Reviews* **2018,** *47* (9), 3037-3058.

49. Wang, F.; Tu, B.; He, P.; Wang, Z.; Yin, L.; Cheng, R.; Wang, J.; Fang, Q.; He, J., Uncovering the Conduction Behavior of van der Waals Ambipolar Semiconductors. *Advanced Materials* **2019,** *31* (1), 1805317.

50. Lee, J. S.; Choi, S. H.; Yun, S. J.; Kim, Y. I.; Boandoh, S.; Park, J.-H.; Shin, B. G.; Ko, H.; Lee, S. H.; Kim, Y.-M., Wafer-scale single-crystal hexagonal boron nitride film via self-collimated grain formation. *Science* **2018,** *362* (6416), 817-821.

Chapter 4

Enhancing the Superconducting Transition Temperature of Molybdenum Carbide via the Formation of Carbide/Disulfide Heterostacks

This work was mainly supported by the Basic Office of Science of the Department of Energy under award DE-SC0018025.

4.1 Introduction and Motivation

2D superconductivity is now emerging as a scientific frontier addressing a number of unanswered questions, such as the disparate evolution of the superconducting transition temperature as a function of the number of layers and different stackings within different compounds.[1,2] It is interesting to notice that the different phases of molybdenum carbide, that is the α, β, and γ phases were recently predicted to display topologically non-trivial electronic bulk bands that lead to unconventional topological surface states.[3,4] These bulk and related surface states could be harvested to induce unconventional superconductivity through the proximity effect[5] with a superconductor such as α-Mo_2C. Moreover, nearly 2D transition metal carbides (TMCs) crystals, such as α-phase Mo_2C, have been recently synthesized *via* chemical vapor deposition (CVD). As-grown high quality 2D α-Mo_2C displays thickness dependent superconducting transition temperatures (T_C) up to 4K. Therefore, metal carbides stand as promising parent materials for studying the intrinsic properties of superconductivity in two dimensions.[6]

Multiple phases are observed in molybdenum carbide, as identified through their crystallographic structures (orthorhombic α-phase, hexagonal η-phase and a cubic δ-phase), their Mo:C composition ratios (α-Mo_2C, γ'-MoC_{1-x}, γ-MoC, and η-MoC), and by the observed order or disorder related to interstitial carbon atoms within the Mo metal matrix (α- and β-phase Mo_2C).[7] The different phases display distinct superconducting properties, which open up the possibility of manipulating the superconductivity in carbide systems via phase-transitions or fabrication of vertical carbide heterostructures with inducing strain and different stack rotations. Multilayer $W_xMo_{1-x}C_yS_2$ has already been synthesized through mixing, oxidation and sulfurization of mixtures of Mo and WC at high temperatures (800-1100 °C) by Terrones *et al.* in 2000.[8] Consequently, these multilayer systems offer the possibility of tuning their superconductivity properties via sulfur incorporation.

4.2 CVD synthesis of 2D α-Mo_2C flakes

In this chapter, we report the synthesis of layered molybdenum carbide/sulfide vertical heterostructures, through a two-step approach, involving the CVD growth of thin α-Mo_2C, and low-pressure sulfurization treatments at high temperature (details in Chapter 2 Experimental Section).[6] 2D Mo_2C domains were grown by atmosphere pressure CVD directly on the molten Cu substrate as reported.[9] The resulting morphology is shown in the optical image in Fig. 4-1a, different regular shapes (a large portion is hexagon) with lateral sizes around 20 μm can be formed on top of the Cu surface.

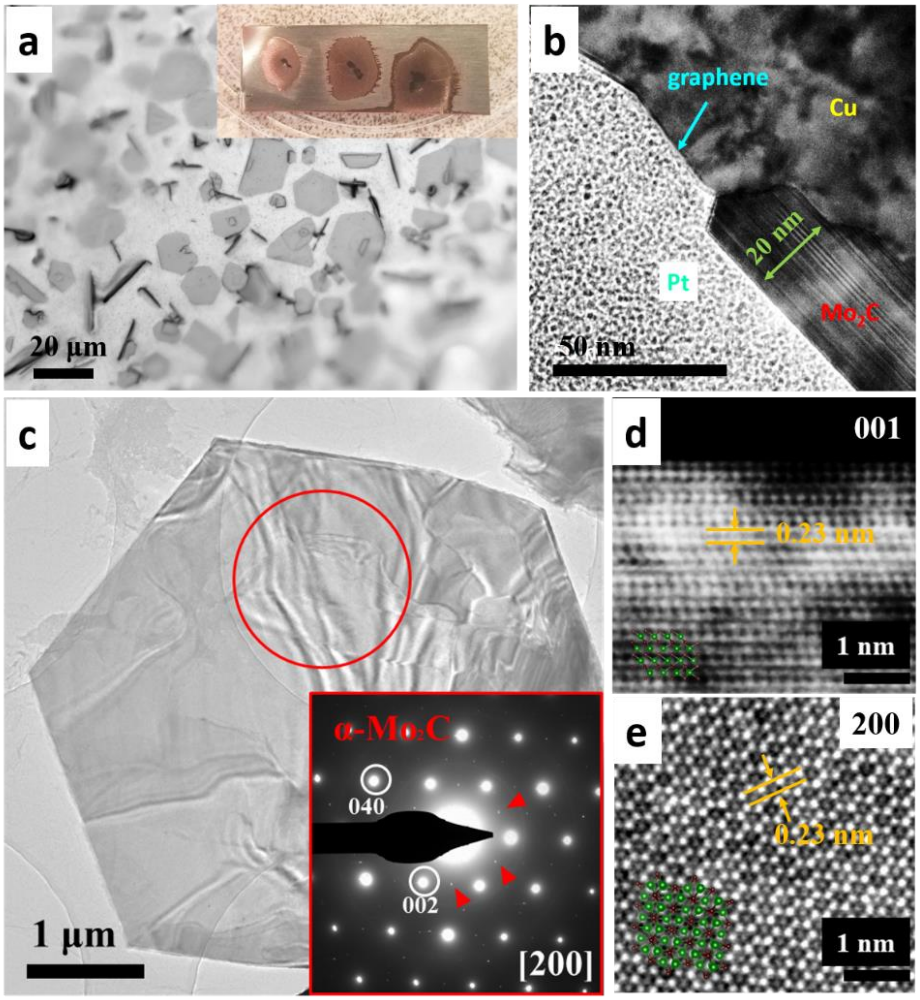

Figure 4- 1 (a) Optical image of 2D Mo_2C domains grown on Cu (inset shows picture of the molten Cu foil on Mo foil after the growth). (b) TEM characterization of as-grown Mo_2C crystals through a cross-sectional TEM image of the Mo_2C. The thickness is around 20nm. (c) TEM image from a perspective perpendicular to the plane. Inset: SAED of the α-Mo_2C (red). (d) HAADF-STEM image showing a cross-sectional and (e) a planar view of α-Mo_2C crystals revealing the lattice spacing.

The Mo_2C lateral size, thickness and coverage can be controlled by tuning the experimental protocols such as methane flow rate, growth temperature and time (the Mo_2C lateral size, thickness and coverage as the function of growth time are discussed in Fig. 4-2). The cross-section TEM image of the interface between Mo_2C and Cu (Fig. 4-1b) clearly shows that the as-grown Mo_2C were embedded in-situ within the molten copper surface, and the rapid cooling concreted the whole

structure, the thickness of the as-grown Mo_2C is around 20 nm for 15 minutes growth at 1090°. Atomic resolution high angle annular dark field scanning TEM (HAADF-STEM) image of the (001) cross-section of a Mo_2C domain shows that it displays an atomic-flat surface with an interlayer spacing of ~0.23nm.

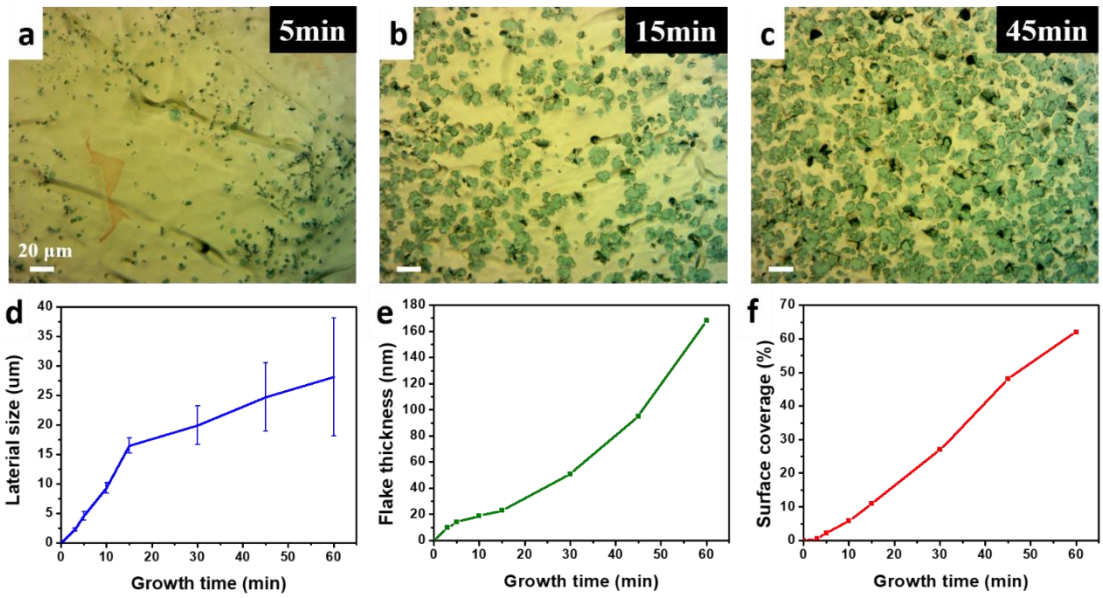

Figure 4- 2 The lateral size, thickness and coverage of pristine 2D Mo_2C with different synthesis time (3, 5, 10, 15, 30, 45 and 60 min, respectively) (a)-(c) Optical images of 2D Mo_2C on Cu with growth time of 5, 15 and 45 minutes, respectively; Plots of (d) The lateral size, (e) flake thickness and (f) surface coverage of pristine 2D Mo_2C with different synthesis time. It is noted that the thickness measurement is done by cross-sectional TEM samples (sample preparation is on the averaged size flake on different growth time).

We also found there were simultaneous growth of graphene when Mo_2C crystals formed (Figs. 4-3a and b), such phenomenon are reported in the recent literatures due to higher methane flow (higher than 1sccm).[10,11] Graphene around the Mo_2C crystals is indicated by the electron diffraction patterns (Fig. 4-3c). The elemental fingerprints of Mo_2C and graphene are also shown by electron energy loss spectroscopy (EELS) in Figs. 4-3d and e. As-grown Mo_2C/graphene heterostructures show great potentials in hydrogen evolution reaction (HER) catalysis[10] and superconductivity[11] applications.

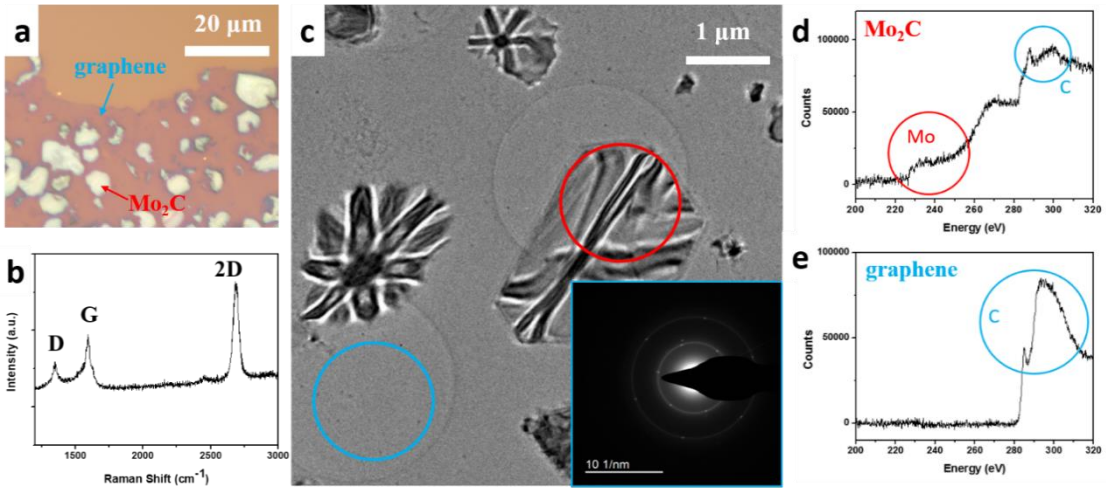

Figure 4- 3 Simultaneous formation of graphene during Mo_2C synthesis. (a) Optical image of graphene/Mo_2C assembly transferred onto SiO_2/Si, the contrast indicates graphene around Mo_2C crystals; (b) Raman of defective graphene formed around Mo_2C, the ratio of I_{2D}/I_G indicates the monolayer nature of the graphene, the emergence of D peak reveals the defects on the graphene; (c) Low magnification TEM image of freestanding graphene/Mo_2C assembly, inset shows the SAED of defective graphene; (d) and (e) EELS edge of as-prepared Mo_2C crystal (from red-circled region in (c)) and defective graphene (from blue-circled region in (c)), respectively.

The obtained morphologies for the initial α-Mo_2C flakes are shown in the scanning electron microscopy (SEM) image inset in Fig. 4-4a and in the optical image in Fig. 4-1a. α-Mo_2C crystals exhibit different faceted shapes (frequently hexagonal) with lateral sizes of around 20 µm. X-ray diffraction (XRD) studies were conducted to identify the phase and orientation of the synthesized material (Fig. 4-4c), which was confirmed as α-Mo_2C, which has an orthorhombic crystalline lattice with the Mo atoms positioned in a slightly distorted HCP arrangement. The α-Mo_2C crystals preferentially grew along the (200) direction (corresponding to the peak at 38.1°). In addition, the small diffraction shoulder peak next to (200) and the small peak located at 47.8° in the pattern correspond to (001) and (201) orientations of α-Mo_2C, respectively.[12]

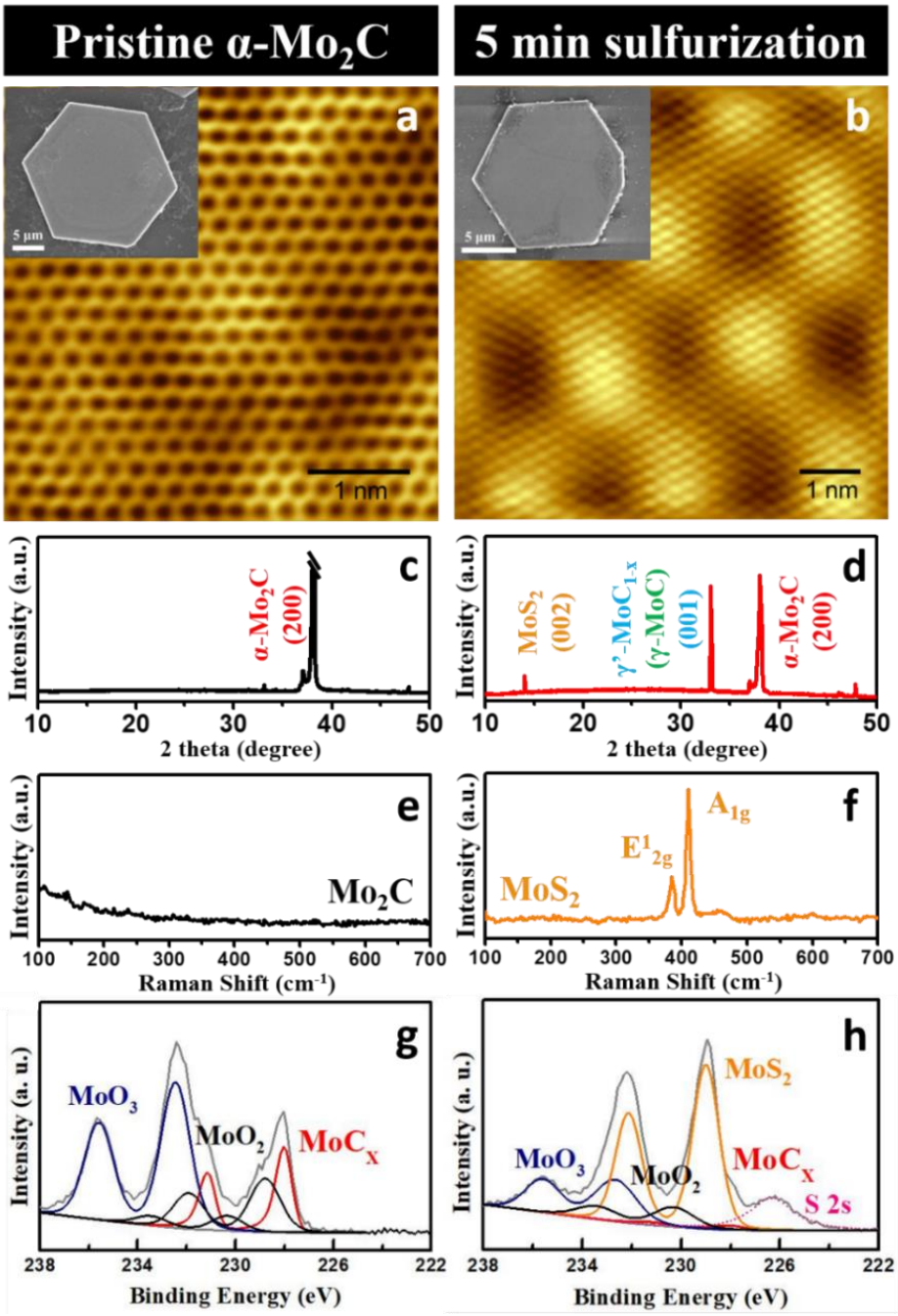

Figure 4- 4 Characterization of α-Mo_2C and molybdenum carbide/disulfide heterostructures. STM images of crystals (insets depict SEM) of as grown α-Mo_2C (a) and a molybdenum carbide/disulfide heterostructure (b) obtained after a 5 min H_2S treatment of Mo_2C. XRD patterns (c, d) and Raman spectra (e, f) of pristine Mo_2C and a molybdenum carbide/disulfide heterostructure on Si/SiO_2, respectively. **g-h,** Representative XPS Mo 3d high resolution line scans obtained from the structures depicted in (a) and (b), respectively.

X-ray photoelectron spectroscopy (XPS) analyses were used to further investigate the chemical composition and valence states in the material. The Mo 3d line scan of pristine Mo_2C shown in Fig. 4-4g is dominated by molybdenum carbide (MoC_x), oxide (MoO_3 at 232.5 eV and 235.6 eV, MoO_2 at 229.1 eV and 232.3 eV) and oxycarbide (MoO_xC_y) signals.[13] Doublets of MoO_3 (Mo^{6+}) and MoO_2 (Mo^{4+}) can be observed due to surface oxidation. The doublets appear at 227.5 and 231.1 eV, corresponding to Mo^{2+} $3d_{5/2}$ and Mo^{2+} $3d_{3/2}$ of α-Mo_2C, respectively.[14] The crystalline structure of the as-grown Mo_2C was also confirmed to be the α-phase, by analyzing planar TEM images (Fig. 4-1), lateral atomic resolution scanning transmission microscopy images (Fig. 4-1e) and selected area diffraction patterns (SAED, Fig. 4-1c) of the α-Mo_2C. The ordered carbons that fill in the octahedral voids[10], are responsible for the formation of superlattices[15] (associated Bragg peaks are indicated by the red-arrows in Fig. 4-1c). Additional SAED patterns and electron energy loss spectroscopy (EELS) analyses can be found in Fig. 4-3, all data in good agreement with the determined α-Mo_2C phase.

We also observe some stacking faults occurring during the high temperature growth and during the postgrowth rapid cooling of the Mo_2C, as indicated in Figs. 4-1b and d (also in the planar view in Figs. 4-5c and d). Such stacking faults were also reported for CVD grown and plasma-enhanced pulsed-laser deposited single-crystalline Mo_2C films[16,17]. Stacking faults affect the termination of the Mo_2C surface perpendicular to the (200) direction making it possible to stabilize the orthorhombic phase of Mo_2C in the 2D limit. It is believed that the stacking faults affect the termination of the Mo_2C surface vertical to (200) direction and make the orthorhombic Mo_2C possible 2D limit, and provide active site besides surface for sulfur incorporation.

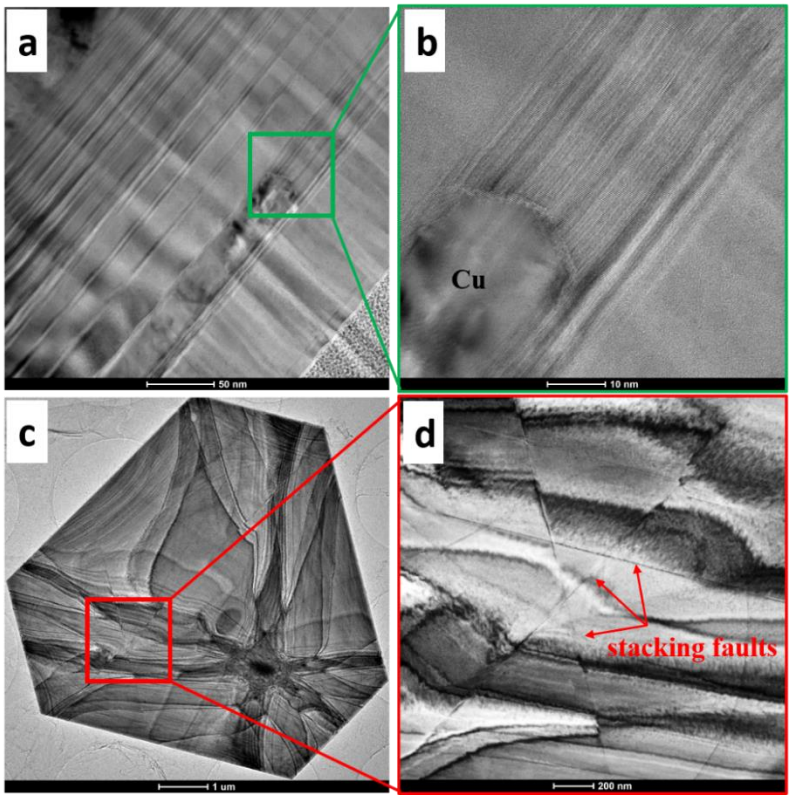

Figure 4- 5 Stacking faults in the CVD synthesized 2D α-Mo_2C crystal. (a) and (b) Cross-sectional TEM image of 2D α-Mo_2C crystal on copper, the contrast difference in parallel to the surface indicates the stacking faults; (c) and (d) Planar-view TEM image of freestanding 2D α-Mo_2C crystal, stacking faults can be distinguished by diffraction contrast.

4.3 Formation of molybdenum carbide/disulfide heterostack

The synthesis method of molybdenum carbide/disulfide heterolayers is described detailed in Chapter 2, the as-prepared heterolayers (Fig. 4-4b) created superlattices with well-defined moiré patterns, which were identified by atomic resolution STM. Figure 1b shows a lattice overlap between MoS_2 and molybdenum carbide with a 0° stacking angle (see also Fig. 4-6).

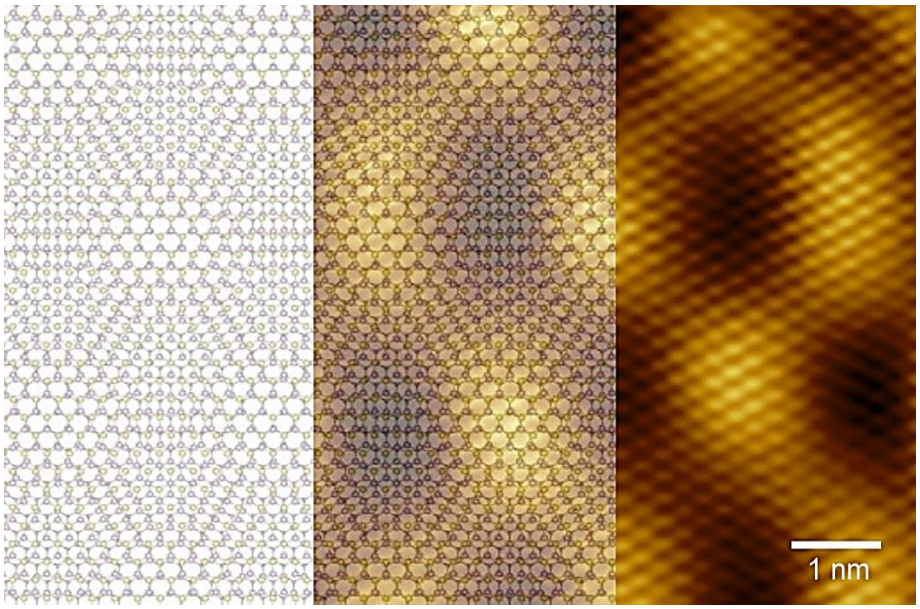

Figure 4- 6 Moiré pattern at MoS_2/carbide heterostacks fitted by schematics and STM image.

XRD analyses (Fig. 4-4d) confirm the 2H-MoS_2 formation (~14.1° peak in Fig. 1d corresponding to the (002) plane of MoS_2) and provide evidence of a phase transition experienced by the molybdenum carbide. We noted that the original Mo_2C in the α-phase (orthorhombic) is transformed to MoC γ-phase (hexagonal, with a AAAA stacking sequence), as indicated by the emergence of a reflection located at 33.0°, which corresponds to the (001) plane of γ-MoC. The α-phase (Mo_2C) and γ-phase (MoC) are the only two thermodynamically stable phases of molybdenum carbide at room temperature, according to the Mo-C phase-diagram.[18] However, the formation of a ternary intermediate carbide phase molybdenum-carbon-sulfur may stabilize the metastable γ'-phase MoC_{1-x}.[7] Similar to the γ-MoC phase, the sub-stoichiometric γ'-MoC_{1-x} phase also crystallizes in a hexagonal structure but with a slightly different stacking in the Mo matrix and distinct carbon occupancies (hexagonal, AABB stacking sequence).[19] It is noteworthy that such a phase transition does not happen through a simple annealing of the α-Mo_2C phase at high temperature (XRD shown in Fig. 4-7). It is believed that sulfur incorporation can form ternary solid solutions based on Mo-C-S, while excessive chalcogen and internal strain would trigger phase

segregation between the carbide and the disulfide. Sulfur will consequently extract the Mo atoms from α-Mo_2C, thus leading to the Mo:C atomic ratio gradually decreasing from 2:1 to 1:1, and resulting in the α-γ'-γ phase transitions, responsible of forming the MoC/MoS_2 vertical heterostructures. The MoC_{1-x} phase (γ') was reported to display higher Debye temperatures and a stronger electron-phonon coupling when compared to the α-Mo_2C phase, which could lead to a higher superconducting transition temperature.[20,21] In fact, an increase in T_c is indeed observed in the carbide upon sulfur incorporation, as described by the detailed measurements shown below.

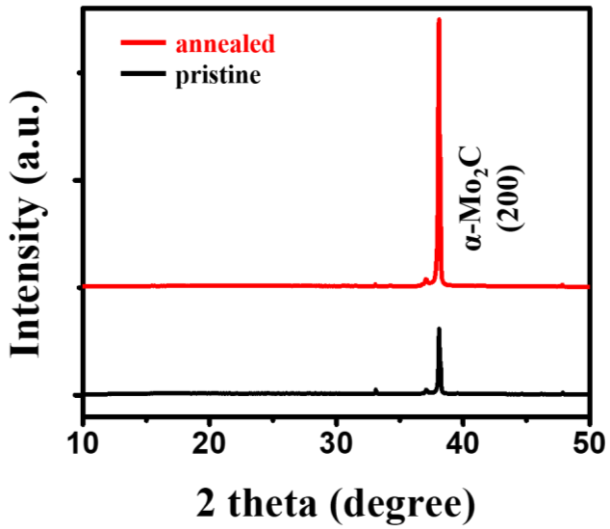

Figure 4- 7 XRD plots of (a) 2D α-Mo_2C crystals transferred onto Si/SiO_2 substrate and (b) after annealing at 800°C for 30 minutes in vacuum. Results support that no phase transition is triggered by high temperature annealing.

XPS analysis carried out in molybdenum carbide/disulfide vertical heterostructures (Fig. 4-4h) exhibits peaks corresponding to binding energies of molybdenum carbide (MoC_x) and also oxides (MoO_2 and MoO_3). Additionally, the spectrum displays a small bump located at 226.4 eV, which is associated to elemental S in the 2s region after a short sulfurization time. Moreover, the characteristic doublet peaks at 228.7 eV and 232.0 eV (Fig. 4-4h) correspond to the Mo^{4+} $3d_{5/2}$ and Mo^{4+} $3d_{3/2}$ binding energies of MoS_2, respectively. In the S 2p line scan (Fig. 4-8), the doublet 162 and 163.2 eV peaks are found, corresponding to $2p_{3/2}$ and $2p_{1/2}$, respectively. Their energy

separation is ~1.2 eV, which is consistent with the fingerprint of S^{2-} in MoS_2.[13] Raman spectra demonstrate the emergence of the two main peaks identified as the 2H-MoS_2 E^1_{2g} and the A_{1g} phonon modes, after sulfurization of α-Mo_2C (Figs. 4-4e and 1f). The frequency difference between these two phonon modes is $\Delta k \sim 23$ cm^{-1} in the spectra obtained from heterostructures after a 5 min sulfurization, thus indicating the presence few layers of MoS_2 (which is confirmed in Fig. 4-9g).

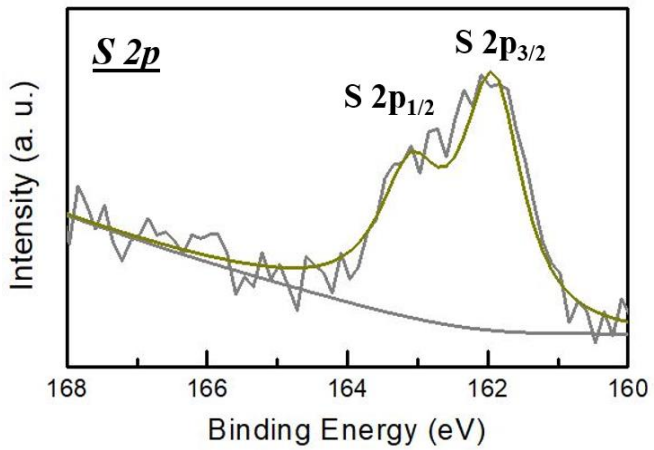

Figure 4- 8 XPS spectra of S 2p obtained from MoS_2/carbide heterostructures (@H_2S 5 min).

Sulfurization treatments performed on thin α-Mo_2C during different times lead to different vertical heterostructures with various crystallographic correspondences between carbide and sulfide. Crystallographic phase's schematics and corresponding cross-sectional TEM images of α-Mo_2C and various synthesized heterostructures (obtained after 1 min, 5 min and 20 min sulfurization) are depicted in Fig. 4-9. The α-Mo_2C HAADF-STEM images display an atomically flat surface with an interlayer spacing of ~0.23 nm (Figs. 4-9e, 4-1b and 4-1d). High resolution TEM images revealed the presence of the metastable γ'-MoC_{1-x} stacked together with α-Mo_2C (Figs. 4-9b and f). γ'-MoC_{1-x} is possibly stabilized by a thin layer of sulfur. The carbide surface was found to be covered by a single-layer of MoS_2 after a 5 min-sulfurization treatment (Figs. 4-9c and g) exhibiting a mixture of γ'(γ) and α phases underneath. The stacking between MoS_2 and molybdenum carbide phases create the moiré pattern exhibited in Fig. 4-4b.

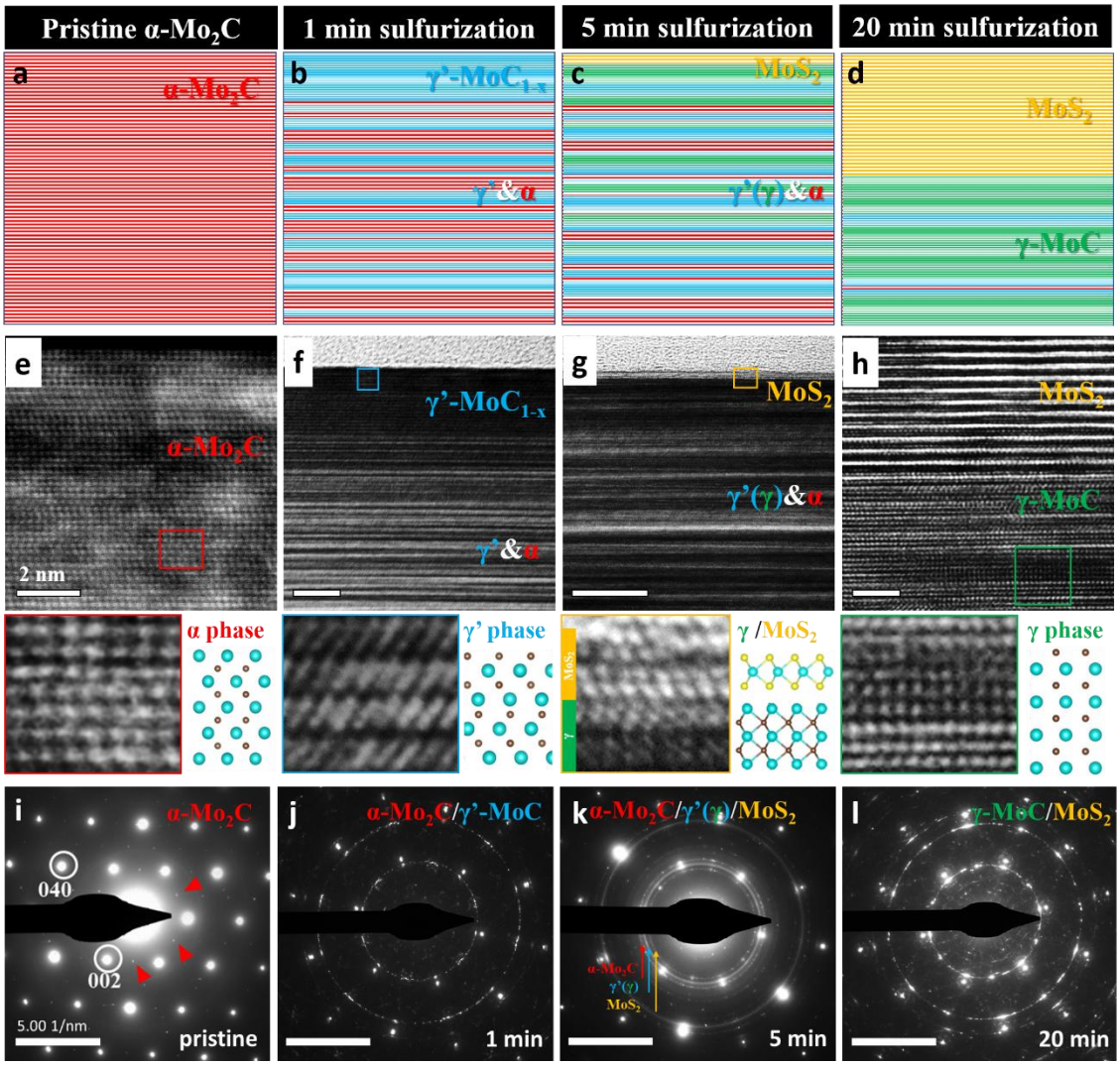

Figure 4- 9 TEM analyses of the molybdenum carbide/disulfide. a-d, Crystallographic phase's schematics of α-Mo_2C (a) and molybdenum carbide/disulfide heterostructures in the cross-sectional view (H_2S treatment of 1 min, (b); 5 min (c); and 20 min (d)). e, Cross sectional HAADF-STEM images of pristine Mo_2C (e) and (f)-(h) HRTEM images of molybdenum carbide/sulfide heterostructures after 1 min, 5 min and 20 min sulfurization, respectively; atomic resolution TEM images reveal the phase transitions induced by the sulfurization process (see insets). Planar view SAED analyses of pristine Mo_2C (i) and molybdenum carbide/sulfide heterostructures for H_2S reaction times of 1 min (j), 5 min (k) and 20 min (l).

Elemental EDS mapping results of the cross-sectional interface were acquired slice-by-slice, providing compositional information (Fig. 4-10). The elemental mappings clearly revealed that the Mo:C ratio gradually decreases from 2:1 to 1:1 while moving towards the side of the carbide

exposed to sulfur, indicating a phase transition induced by the chalcogen incorporation. Heterostructure interfaces plays a crucial role in the electronic and catalytical property of the hybrid materials.[22]

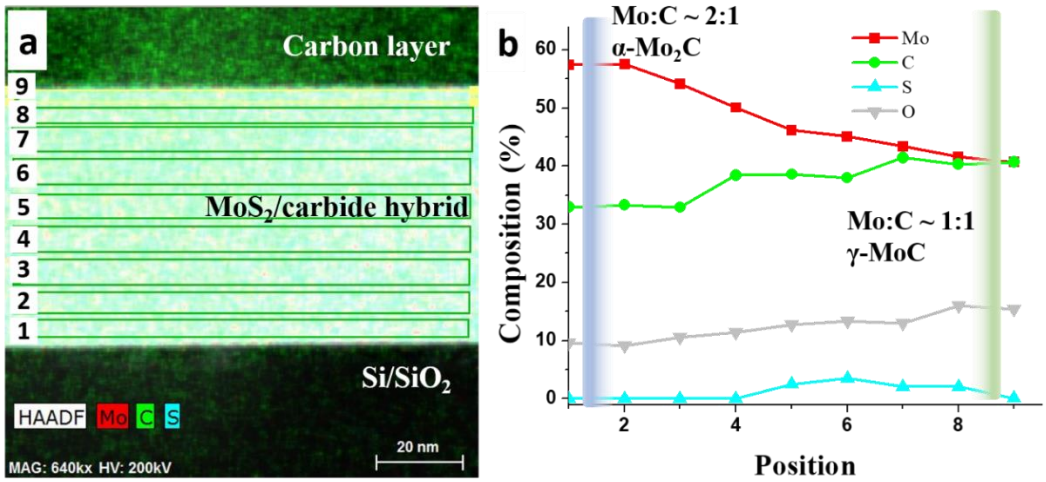

Figure 4- 10 STEM/EDS composition analysis of MoS_2/carbide vertical heterostructure (@H_2S 5 min) (a)EDS mapping graph of the heterostructure, the cross-sectional view has been divided into nine regions to collect composition information; the elemental composition (atomic percentage) analysis results are plotted in (b) including four main elements, Mo, C, S and O; it clearly shows that the Mo:C ratio is gradually decrease from 2:1 to 1:1 from the bottom to the top through the carbide, which indicates the phase transition during the chalcogen incorporation.

High resolution TEM images of samples obtained after 20 min of H_2S treatment, display 10-15 layers of MoS_2 forming a heterostructure with the γ-MoC (Figs. 4-9d, h, l). The HRTEM image of the interface at the MoS_2/carbide heterostructure (@ 20min sulfurization) with the intensity profile plotted in Fig. 4-11. The measured interlayer distance of MoS_2 is ~0.67 nm, in good agreement with a previously reported value.[23] The carbide interlayer spacing changes from 0.23 nm (as-grown α-Mo_2C) to 0.28 nm, corresponding to the γ-MoC (001) interplanar distance, which also is in good agreement with the XRD results in Fig. 1d. The interface between $MoSe_2$ and γ-MoC was measured as ~ 0.58 nm, which is slightly larger than the distance between TMD materials vdW epitaxial grown on the 2D BN (~ 0.50 nm) as reported.[24] Therefore, we can conclude that the thickness of the MoS_2 layers is dependent on the H_2S treatment time. Moreover, the

disulfide formation does not only happen in the basal plane of the carbide, but it also selectively formed through stacking faults at edge sites (Fig. 4-12).[25] Such hybrid sulfide stackings hold a great promise as catalysts for energy conversion and as Josephson junction assemblies[26].

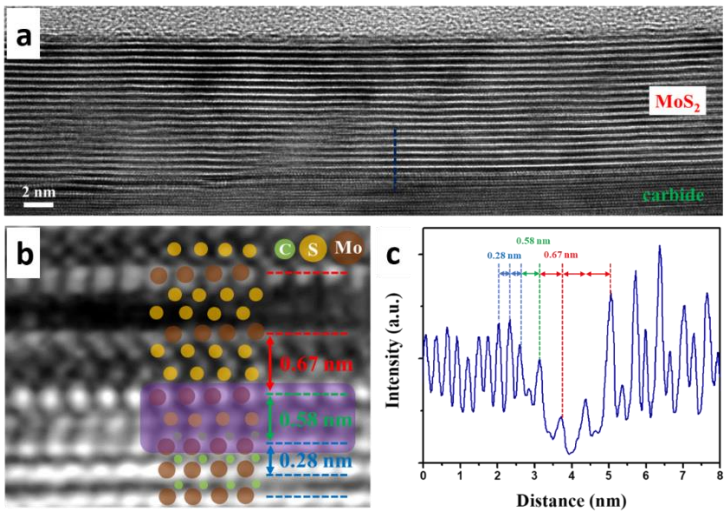

Figure 4- 11 HRTEM image of MoS_2/carbide vertical heterostack with multilayer MoS_2 covered on carbide surface (@H_2S 20 min). (a) Zoom-out region of Figure 4-9h; (b) atomic schematics on the HRTEM image of the interface at the MoS_2/carbide heterostructure with (c) the intensity profile plot of measured interlayer spacings.

The planar-view TEM/SAED patterns of the molybdenum carbide/sulfide stacks as a function of sulfurization time are displayed in Figs. 4-9i-l. A series of shifts can be found in the diffraction patterns upon sulfurization, indicating that the α-Mo_2C phase (red) undergoes a phase-transition towards the γ'-MoC_{1-x} phase (blue) and/or γ-MoC phase (green), which exhibit hexagonal patterns/rings within a plane perpendicular to the [001] axis. Diffraction rings (indicated by the yellow arrow in Fig. 4-9k) result from the formation of a polycrystalline thin film of MoS_2. Moreover, the diffraction pattern reveals that a large portion of the MoS_2 film displays a preferred orientation with a nearly 0° misorientation with respect to γ-MoC, thus supporting the epitaxial growth of MoS_2 on the underlying hexagonal γ-MoC.

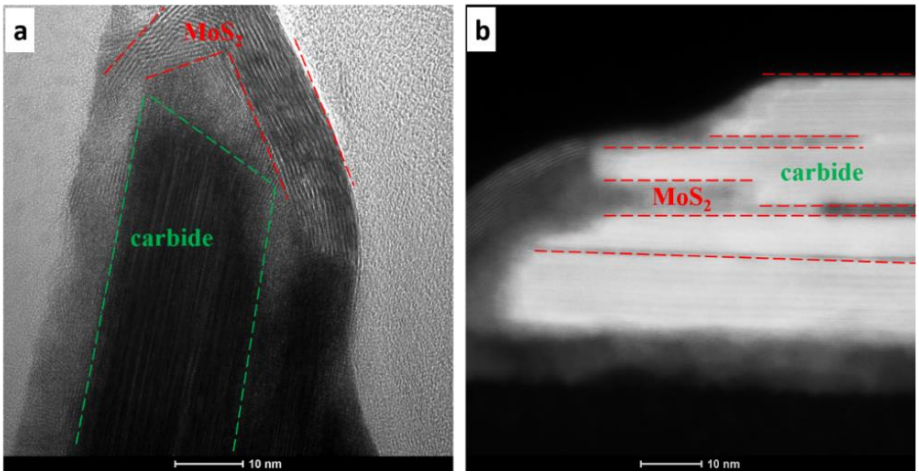

Figure 4- 12 (a) HRTEM and (b) HAADF-STEM image of MoS_2/carbide vertical heterostructure (@H_2S 5 min) at crystal edge, dotted-line shows the region of carbide/dichalcogenide interfaces. MoS_2 not only forms on the basal plane of the carbide, but also form and propagate inside the carbide through the stacking faults.

4.4 Growth Mechanism of molybdenum carbide/dichalcogenide heterostructures and computational studies at carbide/dichalcogenide interface

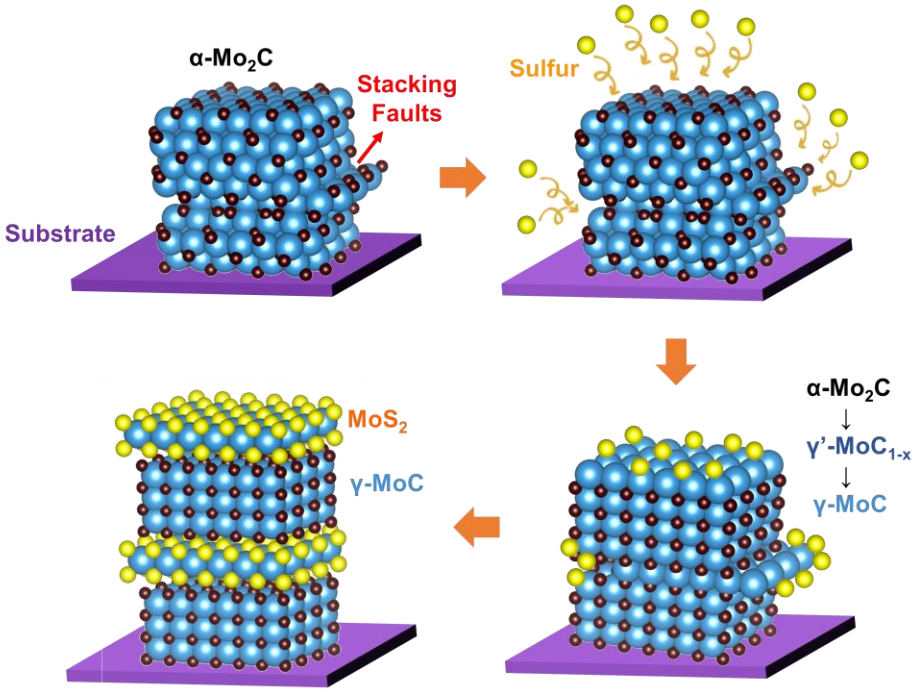

Figure 4- 13 Growth model schematics of molybdenum carbide/dichalcogenide heterostructures. (a) 2D α-Mo_2C transferred onto a chalcogen-resistant substrate, (b) chalcogen (sulfur) incorporation into Mo_2C, and (c) as the chalcogen is incorporated, the system undergoes phase segregation to form hexagonal MoS_2 the γ'-MoC_{1-x} (chalcogen stabilized) phase, as *x* is reduced to zero one stabilizes the γ-MoC phase. (d) The formation of the sandwiched "quasi-intercalated" heterostructure is stabilized by stacking faults.

To better understand the heteroepitaxial growth of MoS_2 on molybdenum carbide, the α-γ'-γ phase transition, and the sandwiched "quasi-intercalated" heterostructure, we propose a model for chalcogen incorporation in 2D molybdenum carbide (Fig. 4-13). When chalcogens are incorporated into Mo_2C, a ternary solid solution would form between the chalcogen and molybdenum carbide. As the chalcogen amount increases, α-Mo_2C undergoes the extraction of Mo atoms from the orthorhombic structure to stabilize the γ'-MoC_{1-x} (chalcogen stabilized) phase. As the incorporation of chalcogen increases, the fraction x drops to zero to form hexagonal MoS_2 and stable γ-MoC phase. The MoS_2 nucleates at the step edges of the (001) surface at the basal plane of the γ-MoC, forming in-plane heterostructures with carbide surfaces, while growing along the vertical direction with respect to this (001) surface of γ-MoC. Chalcogen incorporation can also occur at energetically favorable positions such as defects or stacking faults. As a result, a "quasi-intercalated" hybrid structure is built through this synthesis method.

Various epitaxial possibilities of heterostructures confining MoS_2 inside molybdenum carbide layers were studied using DFT calculations. The interfacial structure between γ-MoC and MoS_2 was predicted to be in two possible stable configurations, which are strained-epitaxial heterostructure (Figs. 4-14 a-h) and moiré heterostructure (Fig. 4-14 i-l). The side views of both possible vertical heterostructures are overlapped with the HRTEM images in Figs. 4-14b, f, and j. The density of states (DOS) of the interfaces between MoS_2 and γ-MoC was analyzed to calculate the bandgap of each MoS_2 layer, and determine the electronic contributions to the adjustment of bandgaps (Figs. 4-14d, h, and l). In the strained-epitaxial vertical heterostructure, when one layer

of MoS_2 and 6 layers of MoC were stacked (Figs. 4-14 a-d), the MoS_2 underwent a -6.5% in epitaxial strain with a bandgap of 0.25 eV, which represents a 1.44 eV reduction when compared to the bandgap of a relaxed MoS_2 monolayer. A comparison between the DFT calculated DOS and the experimental dI/dV curve obtained by STS measurements on a MoS_2/carbide heterostructure (5 min-sulfurized) indicates a good agreement in the bandgap of around 250 meV for strained-epitaxial MoS_2 embedded in the carbide (Fig. 4-15). When three layers of MoS_2 and six layers of MoC were stacked (Figs. 4-14 e-h), the MoS_2 layers were under a -5.7% epitaxial strain, and the bandgaps of the interfacial layer and middle layer were 0.81 eV and 1.12 eV, respectively. However, in moiré heterostructures, the comparable electron densities at the γ-MoC interface and between the MoS_2 layers, indicate that the atomic interaction is almost the same as the vdW interaction between the MoS_2 layers (Figs. 4-14 i-l).

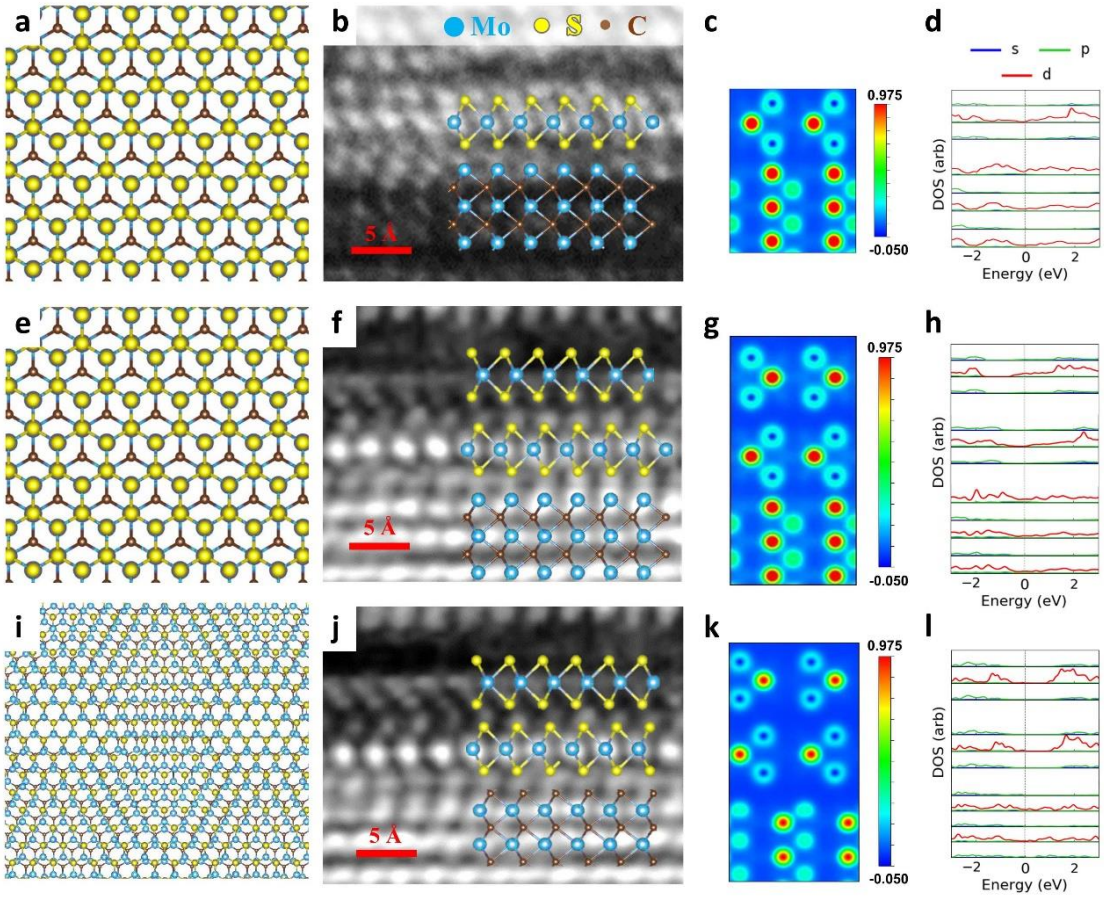

Figure 4- 14 Electronic properties of different heterostructures. a-d, one-layer MoS_2 and γ-MoC in a strained-epitaxial state. a, Planar schematic view of the heterostructure. b, Schematic side view of the heterostructure overlapped with the TEM image. c, Electron density map corresponding to the side view crystal structure shown in (b). d, Density of states (DOS) in s, p and d orbitals at each atomic layer corresponding to the side view crystal structure shown in (b). Schematic view, TEM, electron density map and DOS of (e)-(h) three-layer MoS_2 sandwiched by γ-MoC in a strained-epitaxial state and (i-l) three-layer MoS_2 sandwiched by γ-MoC, forming a moiré superlattice, respectively.

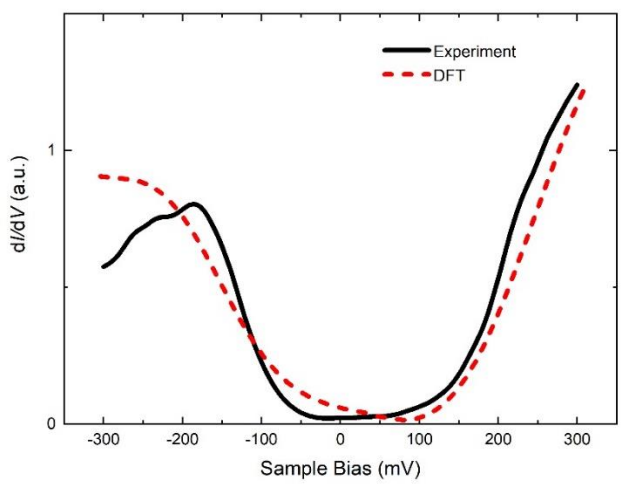

Figure 4- 15 Comparison between the theoretically DFT calculated density of states and experimentally obtained dI/dV curve by STS measurements on MoS_2/carbide heterostructure sample treated for 5min by H_2S. Both the curves show indicate a matching bandgap of around 250 meV for monolayer strained epitaxial MoS_2 on carbide. The STS curve is taken with a set point tunneling current of 100pA and sample bias of 300mV.

4.5 Superconducting state in molybdenum carbide/sulfide vertical heterostructures

We studied the transport properties of pristine α-Mo_2C, chosen as reference, and of the molybdenum carbide/sulfide heterostructure in order to detect superconductivity in the latter. Figure 4-16a shows the resistivity as a function of temperature for a 60 nm thick pristine α-Mo_2C crystal. The inset clearly indicates that the sample becomes superconducting at $T_c \cong 4$ K, as previously reported.[6] The finite resistivity observed below T_c results from the physical or electrical

connection between the α-Mo_2C crystal and the graphene layer resulting from the synthesis process (see Fig. 4-3). As seen, the transition is very sharp, displaying a width inferior to 0.2 K. This, combined with the low residual resistivity ρ(4K) ≈ 1 μΩ cm and the large residual resistivity ratio ρ(300K)/ ρ(4K) = 22, indicates a high quality single-crystal.

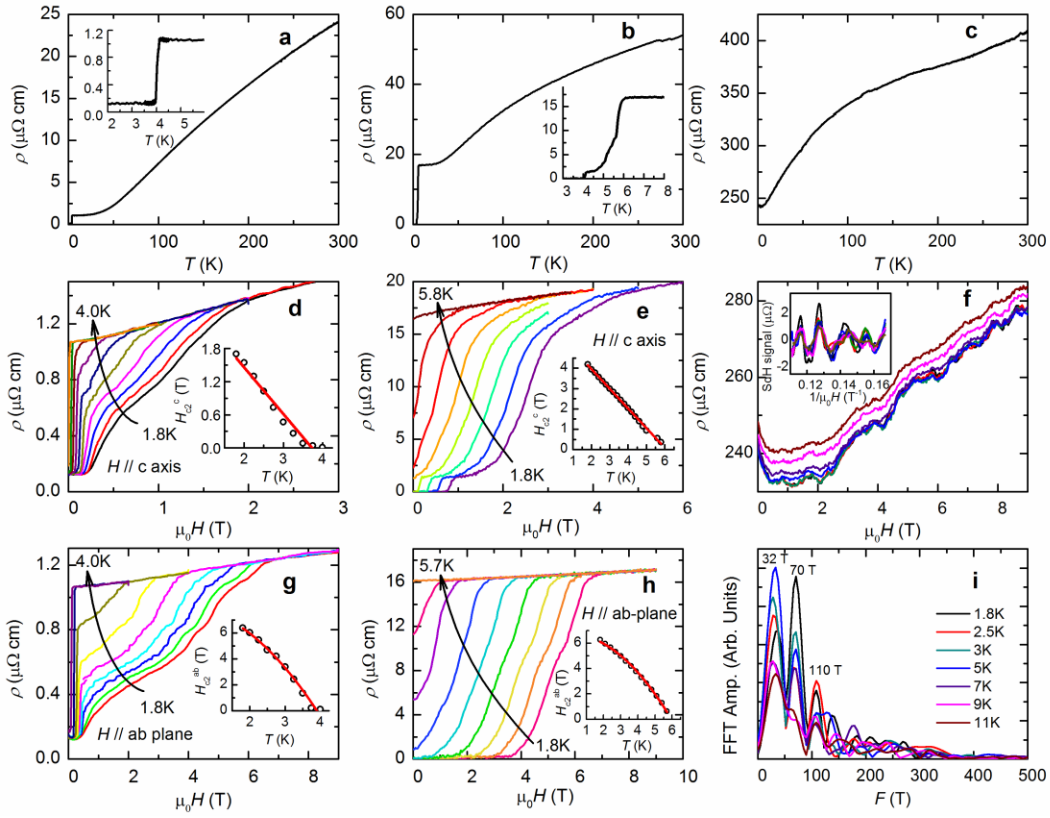

Figure 4- 16 Evolution of the superconducting state in molybdenum carbide/sulfide vertical heterostructures subjected to different sulfurization times. (a)-(c), Resistivity ρ as a function of the temperature T for pristine α-Mo_2C (a) and for molybdenum carbide/sulfide heterostructures subjected to5 min (b), and 20 min (c) sulfurization treatments. Insets in (a) and (b) display ρ as a function of T in the low temperature region where the superconducting transitions, starting at T_c = 4 K and 6 K respectively, become clearly visible. (d)-(f) Temperature dependent ρ as a function of the external magnetic field $\mu_0 H$ applied along the inter-layer c-axis for pristine α-Mo_2C (d) and heterostructures after a 5 min (e) and 20 min (f) sulfurization. Insets in (d) and in (e) show the upper critical fields H_{c2}^c for fields along the c-axis as function of T, where red lines are fits to the conventional Ginzburg-Landau expression. Inset in (f) shows the Shubnikov de Haas (SdH) signal after subtraction of a background polynomial. (g)-(h) Same as in (d)-(e) but for fields along the ab-plane. Insets in (g) and in (h) display H_{c2}^{ab} for $\mu_0 H$ // ab-plane as a function of T. Notice the marked anisotropy between fields along the ab-plane and along the c-axis. (i) Fast Fourier transform of the oscillatory signal superimposed onto the magnetoresistivity of the MoS_2/γ-MoC heterostructure, showing three main peaks at frequencies, $F_\alpha \cong 30$ T, $F_\beta \cong 70$ T and $F_\gamma \cong 110$ T.

Figures 4-16b and c display ρ as a function of T for two samples sulfurized for 5 and 20 minutes (analysis from 1 min sulfurized sample is discussed in Fig. 4-17), respectively. The onset of the resistive transition for the sample sulfurized for 5 minutes (thickness ~ 40nm) is $T \cong 6$ K, which is 50 % higher than the onset of the superconducting transition for pristine α-Mo_2C. As seen in the inset of Fig. 4-16b, the resistive transition reveals multiple steps, indicating an inhomogeneous material, or the coexistence of multiple crystallographic phases. The lowest resistive step occurs at around 4 K, which corresponds to the T_c of pristine α-Mo_2C. Based on our structural analysis we argue that the observation of a higher T_c is associated with the γ'-MoC_{1-x} phase. Figure 4-16c shows the resistivity as a function of temperature for a 40 nm thick MoS_2/γ-MoC heterostructure resulting from a 20 min sulfurization process. The heterostructure clearly displays a metallic behavior over the entire temperature range, although no superconductivity is observed down to $T = 1.8$ K, as expected for γ-MoC. The incorporation of the MoS_2 layer leads to a rather high residual resistivity. Given that most of the current should be carried by the γ-MoC layers sandwiched between the MoS_2 layers, such a high residual resistivity would point to either a significant density of defects in the γ-MoC layers, or to a low density of carriers, or to both in addition to an effective cross-sectional area smaller than the thickness used to calculate the resistivity.

Figures 4-16d and 4e display the resistivity as a function of the magnetic field $\mu_0 H$ at various constant temperatures, unveiling the superconducting to metallic phase-transitions for fields oriented perpendicularly to the planes of pristine α-Mo_2C and γ'-MoC_{1-x}, respectively. The insets in both figures display the upper critical field H_{c2}^{c} for fields along the c-axis as a function of the temperature, where red lines are linear fits. Here, to define the value of H_{c2}^{c} we chose the 90% criteria or the field value where the resistivity reaches 90 % of its value in the normal state just

above the transition. The linear temperature behavior is consistent with the two-dimensional Ginzburg-Landau formalism for fields perpendicular to the planes: $\mu_0 H_{c2}^{c} = \Phi_0(1 - T/T_c)/\ 2\pi\xi_{ab}^2$, where Φ_0 is the magnetic flux quantum, μ_0 the permeability of free space, and ξ_{ab} is the in-plane coherence length. This supports the 2D nature of the superconducting state in these crystals despite their sizeable thicknesses. Figure 4-16f displays the isothermal ρ for the sample sulfurized for 20 min as a function of $\mu_0 H$. A negative magnetoresistivity is observed for $\mu_0 H < 1$ T and for all temperatures, which we tentatively attribute to weak anti-localization.[27] An oscillatory signal, which can be suppressed by increasing the temperature, emerges when $\mu_0 H > 5$T. These oscillations turn out to be periodic in inverse fields, indicating that these would correspond to Shubnikov-de Haas oscillations. The inset reveals the oscillatory component once the background magnetoresistivity is subtracted through a polynomial fit. The observation of quantum oscillations is rather surprising given the very large residual resistivity observed in the MoS_2/γ-MoC heterostructure, and suggests that small regions of the γ-MoC should be well-ordered from a crystallographic perspective.

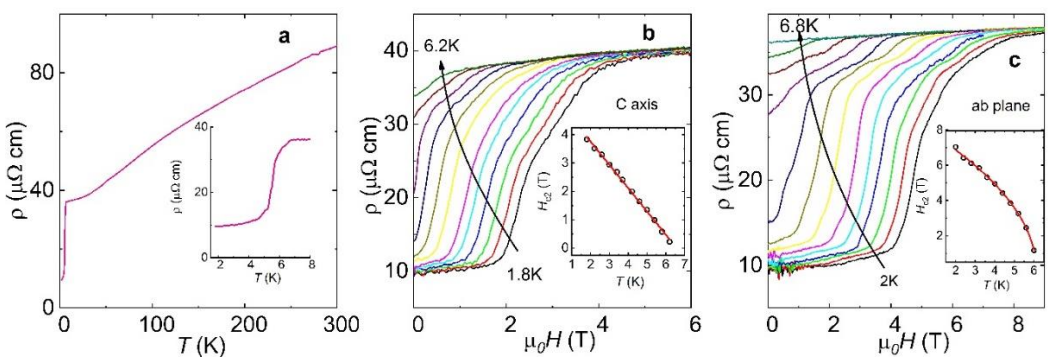

Figure 4- 17 (a) Resistivity ρ as a function of the temperature T for MoS_2/carbide heterostructures subjected to H_2S gas phase reaction 1 min. Insets in (a) display ρ as a function of T in the low temperature region where the superconducting transitions starting at T_c = 6 K, become clearly visible. (b) ρ as a function of the external magnetic field $\mu_0 H$ applied along the inter-layer c-axis for 1 min sulfurizing sample at several temperatures. Insets in (b) show the upper critical fields H_{c2} as functions of T where red lines are fits to the conventional Ginzburg-Landau expression. (c) Same as in (b) but for fields along the ab-plane. Insets in (c) display H_{c2} for $\mu_0 H$ // ab-plane as a function of T. Notice the marked anisotropy between fields along the ab-plane and along the c-axis.

Figures 4-16g and 4h display the temperature dependence of the resistive transition for fields along the conducting planes. There is anisotropy in upper-critical fields for both field orientations (by comparing with panels 4-16d and 4e, respectively), and the superconducting transition is inhomogeneous. This inhomogeneity probably results from a combination of vortex physics, crystallographic heterogeneity or variations in composition. In both panels, the insets show the upper critical fields as a function of temperature, which is consistent with the conventional Ginzburg-Landau (GL) behavior. Red lines are fits to the conventional GL expression:

$$H_{C2}^{ab}(T) = \Phi_0\left(1 - \left(\frac{T}{Tc}\right)^2\right)/2\pi\xi_{ab}\xi_c$$

Where is ξ_c the interplanar coherence-length. The good fit to a conventional three-dimensional GL expression contradicts the behavior observed for fields applied perpendicularly to the planes that, instead, suggests 2D superconductivity. Instead, the 2D GL formalism predicts a $T^{1/2}$ dependence for H_{c2}^{ab} near T_c. Perhaps, one way to reconcile both observations is to assume that one is in an intermediate regime, that is approaching the 2D superconducting limit, but still in a three-dimensional regime due to the thicknesses of these crystals, which are multilayered.

Finally, Figure 4-16i displays the Fourier transform of the oscillatory signal shown in the inset of Fig. 4-16f. Two main frequencies F are observable in the range up to 400 T, F_α =30 T, F_β = 70 T and $F\gamma$= 110 T, respectively. Such peaks indicate that the observed oscillations correspond to the Shubnikov-de Haas-effect resulting from the Landau quantization of the electronic orbits. These small frequencies indicate small Fermi surface extremal cross-sectional areas[28]. These oscillations are observable up to high temperatures, indicating light effective masses[29] as seen in semimetallic systems. Indeed, through the Lifshitz-Kosevich formalism, we extract fairly light effective masses, that is $m_\alpha = (0.3 \pm 0.3)\ m_0$, $m_\beta = (0.13 \pm 0.05)\ m_0$ and $m_\gamma = (0.7 \pm 0.3)\ m_0$, where

m_0 is the bare electron mass. Recent DFT calculations indicate that γ-MoC might display non-trivial electronic topology, being a Dirac nodal line semimetal, which could become superconducting upon hole doping.[3] The same calculations indicate that the Fermi surface should be composed of additional, larger Fermi surface sheets not detected in this study, probably because the measurements should be performed under higher fields. The associated surface states are proposed to be good candidates to host unconventional superconductivity upon doping.[4]

4.6 Chapter Summary

In this chapter, we have established a two-step route to synthesize a completely novel TMC/TMD hetero-layered material, comprising γ-MoC and MoS_2. Extensive characterization has been carried out to elucidate the structural details and formation mechanism of TMC/TMDs vertical heterostructures. We have found that the molybdenum carbide undergoes a series of phase transitions between the α-γ'-γ phases during synthesis, which are mainly driven by the induced chalcogen incorporation into α-Mo_2C. The overall result leads to a highly controlled tunable superconductivity in vertical heterostructures and moiré patterns. Moreover, we can increase the Tc by 50% when compared to that of the starting material. Thus, we have developed a novel sulfurization route for inducing strained phase transitions in metal carbide systems, alternative to the established approach of carbon incorporation,[19] which provides a platform to investigate the superconducting properties of different crystallographic phases at their interfaces. Notice that α-MoC (not α-Mo_2C) was recently predicted to display a non-trivial Z_2 invariant, implying that its surface states could be harvested to induce $p + ip$ triplet superconductivity, for instance, through the use of an external gate.[4] Similarly, topological surface bands (drumhead states) in γ-MoC (with C termination) are predicted to lie around the Fermi level.[30] Therefore, nontrivial superconducting pairing might also occur in γ-MoC upon doping or gating.[4] Notice that β-MoC crystallizes in the

same structure as WC, or P-6m2 (or No. 187), which is predicted to display type-II triply-degenerate fermions, also making this compound a good candidate for unconventional topological behavior.[4] Therefore, the precise control achieved in the growth of molybdenum carbide/sulfide vertical heterostructures could open unique opportunities, not only for research in topological materials and related surface states, but also in unconventional superconductivity with implications for quantum information sciences. Moreover, we envisage that the superconductor/semiconductor heterojunctions will play a key role in tunneling experiments, when evaluating the pairing symmetry of these compounds and resulting heterostructures through Cooper pair tunneling, and also in functional electronic components and applications in catalysis. Ultimately, the designed route for engineering the various phases of molybdenum carbide embedded in the created vertical heterostructures could also be applied to tungsten-based carbides, metal nitrides and their different stacked combinations.

4.7 References

1. Sergio, C.; Sinko, M. R.; Gopalan, D. P.; Sivadas, N.; Seyler, K. L.; Watanabe, K.; Taniguchi, T.; Tsen, A. W.; Xu, X.; Xiao, D., Tuning Ising superconductivity with layer and spin–orbit coupling in two-dimensional transition-metal dichalcogenides. *Nature communications* **2018,** *9*.

2. Peng, J.; Liu, Y.; Luo, X.; Wu, J.; Lin, Y.; Guo, Y.; Zhao, J.; Wu, X.; Wu, C.; Xie, Y., High Phase Purity of Large-Sized 1T′-MoS_2 Monolayers with 2D Superconductivity. *Advanced Materials* **2019,** *31* (19), 1900568.

3. Huang, A.; Smith, A. D.; Schwinn, M.; Lu, Q.; Chang, T.-R.; Xie, W.; Jeng, H.-T.; Bian, G., Multiple topological electronic phases in superconductor MoC. *Physical Review Materials* **2018,** *2* (5), 054205.

4. Chang, G.; Xu, S.-Y.; Huang, S.-M.; Sanchez, D. S.; Hsu, C.-H.; Bian, G.; Yu, Z.-M.; Belopolski, I.; Alidoust, N.; Zheng, H., Nexus fermions in topological symmorphic crystalline metals. *Scientific reports* **2017,** *7* (1), 1688.

5. Fu, L.; Kane, C. L., Superconducting proximity effect and Majorana fermions at the surface of a topological insulator. *Physical review letters* **2008,** *100* (9), 096407.

6. Xu, C.; Wang, L.; Liu, Z.; Chen, L.; Guo, J.; Kang, N.; Ma, X.-L.; Cheng, H.-M.; Ren, W., Large-area high-quality 2D ultrathin Mo_2C superconducting crystals. *Nature materials* **2015,** *14* (11), 1135.

7. Hugosson, H. W.; Eriksson, O.; Nordström, L.; Jansson, U.; Fast, L.; Delin, A.; Wills, J. M.; Johansson, B., Theory of phase stabilities and bonding mechanisms in stoichiometric and substoichiometric molybdenum carbide. *Journal of applied physics* **1999,** *86* (7), 3758-3767.

8. Hsu, W.; Zhu, Y.; Boothroyd, C.; Kinloch, I.; Trasobares, S.; Terrones, H.; Grobert, N.; Terrones, M.; Escudero, R.; Chen, G., Mixed-Phase $W_xMo_yC_zS_2$ Nanotubes. *Chemistry of materials* **2000,** *12* (12), 3541-3546.

9. Xu, C.; Wang, L.; Liu, Z.; Chen, L.; Guo, J.; Kang, N.; Ma, X.-L.; Cheng, H.-M.; Ren, W., Large-area high-quality 2D ultrathin Mo_2C superconducting crystals. *Nature materials* **2015,** *14* (11), 1135-1141.

10. Geng, D.; Zhao, X.; Chen, Z.; Sun, W.; Fu, W.; Chen, J.; Liu, W.; Zhou, W.; Loh, K. P., Direct Synthesis of Large-Area 2D Mo_2C on In Situ Grown Graphene. *Advanced Materials* **2017,** *29* (35).

11. Qiao, J.-B.; Gong, Y.; Zuo, W.-J.; Wei, Y.-C.; Ma, D.-L.; Yang, H.; Yang, N.; Qiao, K.-Y.; Shi, J.-A.; Gu, L., One-step synthesis of van der Waals heterostructures of graphene and two-dimensional superconducting $\alpha-Mo_2C$. *Physical Review B* **2017,** *95* (20), 201403.

12. García, G.; Roca-Ayats, M.; Guillén-Villafuerte, O.; Rodríguez, J.; Arévalo, M.; Pastor, E., Electrochemical performance of α-Mo2C as catalyst for the hydrogen evolution reaction. *Journal*

of Electroanalytical Chemistry **2017,** *793*, 235-241.

13. Tang, C.; Wang, W.; Sun, A.; Qi, C.; Zhang, D.; Wu, Z.; Wang, D., Sulfur-decorated molybdenum carbide catalysts for enhanced hydrogen evolution. *ACS Catalysis* **2015,** *5* (11), 6956-6963.

14. Jeon, J.; Park, Y.; Choi, S.; Lee, J.; Lim, S. S.; Lee, B. H.; Song, Y. J.; Cho, J. H.; Jang, Y. H.; Lee, S., Epitaxial synthesis of molybdenum carbide and formation of a Mo_2C/MoS_2 hybrid structure via chemical conversion of molybdenum disulfide. *ACS nano* **2018,** *12* (1), 338-346.

15. Liu, Z.; Fei, Z.; Xu, C.; Jiang, Y.; Ma, X.-L.; Cheng, H.-M.; Ren, W., Phase transition and in situ construction of lateral heterostructure of 2D superconducting α/β Mo_2C with sharp interface by electron beam irradiation. *Nanoscale* **2017,** *9* (22), 7501-7507.

16. Geng, D.; Zhao, X.; Li, L.; Song, P.; Tian, B.; Liu, W.; Chen, J.; Shi, D.; Lin, M.; Zhou, W., Controlled growth of ultrathin Mo_2C superconducting crystals on liquid Cu surface. *2D Materials* **2016,** *4* (1), 011012.

17. Zhang, F.; Zhang, Z.; Wang, H.; Chan, C. H.; Chan, N. Y.; Chen, X. X.; Dai, J.-Y., Plasma-enhanced pulsed-laser deposition of single-crystalline Mo_2C ultrathin superconducting films. *Physical Review Materials* **2017,** *1* (3), 034002.

18. Velikanova, T. Y.; Kublii, V.; Khaenko, B., Solid state transformations and phase equilibria in the molybdenum-carbon system. *Soviet powder metallurgy and metal ceramics* **1988,** *27* (11), 891-896.

19. Lu, J.; Hugosson, H.; Eriksson, O.; Nordström, L.; Jansson, U., Chemical vapour deposition of molybdenum carbides: aspects of phase stability. *Thin Solid Films* **2000,** *370* (1-2), 203-212.

20. Morton, N.; James, B.; Wostenholm, G.; Pomfret, D.; Davies, M.; Dykins, J., Superconductivity of molybdenum and tungsten carbides. *Journal of the Less Common Metals* **1971,** *25* (1), 97-106.

21. Meissner, W., W. Meissner and H. Franz, Z. Physik 65, 30 (1930). *Z. Physik* **1930,** *65*, 30.

22. Lei, Y.; Pakhira, S.; Fujisawa, K.; Wang, X.; Iyiola, O. O.; Perea López, N. s.; Laura Elías, A.; Pulickal Rajukumar, L.; Zhou, C.; Kabius, B., Low-temperature Synthesis of Heterostructures of Transition Metal Dichalcogenide Alloys ($W_xMo_{1-x}S_2$) and Graphene with Superior Catalytic Performance for Hydrogen Evolution. *ACS nano* **2017,** *11* (5), 5103-5112.

23. Zhang, F.; Momeni, K.; AlSaud, M. A.; Azizi, A.; Hainey Jr, M. F.; Redwing, J. M.; Chen, L.-Q.; Alem, N., Controlled synthesis of 2D transition metal dichalcogenides: from vertical to planar MoS_2. *2D Materials* **2017,** *4* (2), 025029.

24. Zhang, F.; Wang, Y.; Erb, C.; Wang, K.; Moradifar, P.; Crespi, V.; Alem, N., Full orientation control of epitaxial MoS_2 on hBN assisted by substrate defects. *arXiv preprint arXiv:1801.00487* **2018**.

25. Cambaz, G. Z.; Yushin, G. N.; Gogotsi, Y.; Lutsenko, V. G., Anisotropic etching of SiC whiskers. *Nano letters* **2006,** *6* (3), 548-551.

26. Klemm, R. A., Pristine and intercalated transition metal dichalcogenide superconductors. *Physica C: Superconductivity and its Applications* **2015,** *514*, 86-94.

27. Hikami, S.; Larkin, A. I.; Nagaoka, Y., Spin-orbit interaction and magnetoresistance in the two dimensional random system. *Progress of Theoretical Physics* **1980,** *63* (2), 707-710.

28. SPRINGFORD, M., MAGNETIC OSCILLATIONS IN METALS-SHOENBERG, D. MACMILLAN MAGAZINES LTD PORTERS SOUTH, 4 CRINAN ST, LONDON, ENGLAND N1 9XW: 1984.

29. Armitage, N.; Mele, E.; Vishwanath, A., Weyl and Dirac semimetals in three-dimensional solids. *Reviews of Modern Physics* **2018,** *90* (1), 015001.

Chapter 5

Carbon Doping of WS_2 Monolayers: Band Gap Reduction and P-type Doping Transport

This work was mainly supported by the Basic Office of Science of the Department of Energy under award DE-SC0018025. Clarification of my contribution for this work: Ideas and all the experimental parts except the device fabrication and test are done by me.

5.1 Introduction and Motivation

Extensive research has been directed to the exploration of TMDs' applications for tunable electronics and catalysts. Carbon has been commonly used as an acceptor anion dopant for bulk semiconductors such as GaAs[15] and its alloys (e.g. AlGaAs and InGaAs)[16], using liquid carbon tetrachloride (CCl_4) as a source, due to its low activation energy, low diffusivity, high solid solubility, attractive electrical and optical properties. Previous work has been reported on the incorporation of carbon into several TMDs. For example, rather severe reactions between carbon precursors and MoS_2 have been reported by high temperature (or long period) treatments of MoS_2 in a carbon-rich environment (C_2H_2[17] or degreasing cotton[18]). Those reported mixed phases of

TMDs and transition metal carbides (TMCs) can be used for electro- or photo-catalysis applications[17,18]. On the other hand, MoS_2 can be directly converted into molybdenum carbide via high temperature annealing in a methane environment, thus providing a low resistance and small Schottky barrier height for the Mo_2C/MoS_2 hybrid structures.[19] Theoretical simulations have predicted that tunability of the electronic structure of the MoS_2 can be achieved through substitutional carbon doping, which will have a profound effect on their optical and electronic properties.[20,21]

Here in this chapter, and to the best of our knowledge, we demonstrate for the first time a plasma-assisted strategy to incorporate carbon species as substitutional dopants within the lattice of WS_2 monolayers, which leads to significant changes in the optical band gap and progressively transforms the electronic transport characteristics of WS_2 monolayers. In this context, plasma treatments have been demonstrated as an efficient way to incorporate foreign atoms such as hydrogen[22,23], nitrogen[14], fluorine[24], and phosphorus[12] in MoS_2, via anion substitutional doping. Based on that strategy, we have now developed a plasma-assisted approach to effectively introduce substitutional carbon atoms within WS_2 monolayers. Interestingly, these carbon-doped WS_2 monolayers exhibit tunable optical and electronic properties, as revealed by both experimental measurements and theoretical simulations. Additionally, first principle calculations also indicate the most energetically favorable configurations of carbon-hydrogen species present within the WS_2 lattice, along with their corresponding contribution to the electronic structure of the system. Aberration corrected high-resolution scanning transmission electron microscopy (AC-HRSTEM) is used to identify the presence of substitutional carbon within the WS_2 lattice. Electrical characterization of these doped TMD layers, confirm that carbon can act as a p-type dopant in WS_2.

5.2 Carbon doping of WS_2 by plasma-assisted CVD process

Monolayers of WS_2 were synthesized by atmospheric pressure chemical vapor deposition (CVD), using precursors in a powder form (see Methods section for details). Carbon doping (schematically shown in Fig. 5-1a) was achieved through an inductively coupled plasma enhanced chemical vapor deposition (PECVD) process, in which the plasma was generated by radio frequency (13.56 MHz) at a power of 50-70 W. The dopant precursor used was methane (CH_4), and the carrier gas was a mixture of Ar/H_2 (85/15 %). There is no significant structural degradation of the WS_2 samples after the PECVD process, as demonstrated by a representative SEM micrograph depicted in Fig. 5-1b. Control experiments in which the pristine WS_2 samples were heated up at 400°C with or without the presence of Ar/H_2 plasma (in the absence of CH_4), were also carried out, and those samples were studied and compared against the synthesized carbon-doped WS_2. The advantage of the plasma-assisted route is that it leads to the decomposition of CH_4 into reactive radicals (possibly carbon and hydrocarbons), at a temperature much lower than the decomposition temperature.[14,21,22, 25]

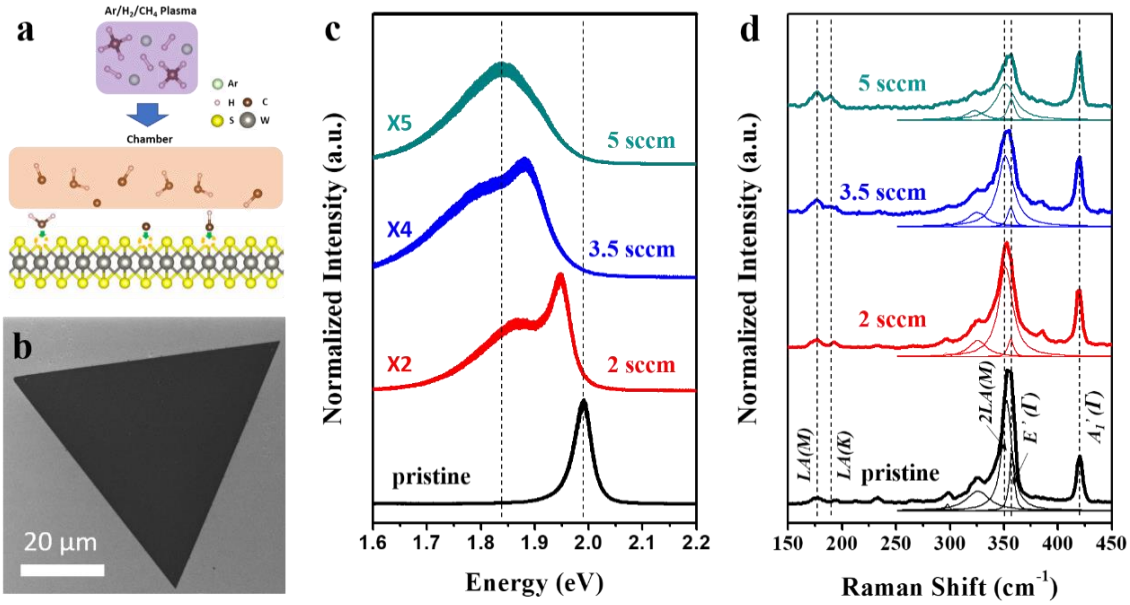

Figure 5- 1 Doping schematics and optical properties. (a) Schematics of the plasma-assisted doping experiment; (b) SEM image of the carbon-doped monolayer WS_2. (c) Photoluminescence and (d) Raman spectra of the undoped and carbon-doped monolayered WS_2 islands, with different methane flow during the plasma treatment (2, 3.5, and 5 sccm, respectively) obtained with a laser excitation of 488 nm and of 514 nm, respectively.

The optical properties of pristine (undoped) and carbon-doped WS_2 monolayers were studied by photoluminescence (PL) and Raman spectroscopies (Fig. 5-1c and d). For pristine monolayers of WS_2, a single PL peak at 1.98 eV was detected (corresponding to the A exciton[26]; see Fig. 5-1c). PL spectra of control pristine samples heat treated at 400°C under an Ar/H_2 atmosphere (in the absence of plasma), were obtained and the spectra were similar to that of pristine WS_2, with a slight decrease in intensity (see Fig. 5-2). When WS_2 was treated only with Ar/H_2 plasma at 400°C, a slight red-shift in the PL was observed and the PL intensity decreased significantly. This decrease in the PL constitutes an indirect evidence of the presence of defects (such as sulfur vacancies) within the WS_2 lattice caused by the plasma bombardment, which could assist carbon doping. WS_2 samples treated with plasma with a different CH_4 flow (2 sccm, 3.5 sccm and 5sccm, Ar/H_2 as carrier gas at a flow of 100 sccm), exhibit significant changes in their PL spectra, as seen in Fig. 5-1c. The PL intensity decreased progressively as the CH_4 gas flow increased. Moreover, the PL peak shifted progressively towards lower energy values and it broadened as new emissions were detected. For the WS_2 sample treated under a CH_4 flow of 5 sccm, the center of the PL emission was located at 1.83 eV, which represents a shift of 150 meV, when compared to the pristine WS_2. It is noted that the full width half maxima of PL enlargement observed after introducing carbon atoms, is possibly due to the generation of additional sulfur vacancies and more random doping of CH- units within WS_2 during the PECVD process. The uniformity of the modulated PL emission was probed by PL mappings, which clearly show a uniform intensity throughout the carbon-doped WS_2 monolayer (see Fig. 5-3a and b).

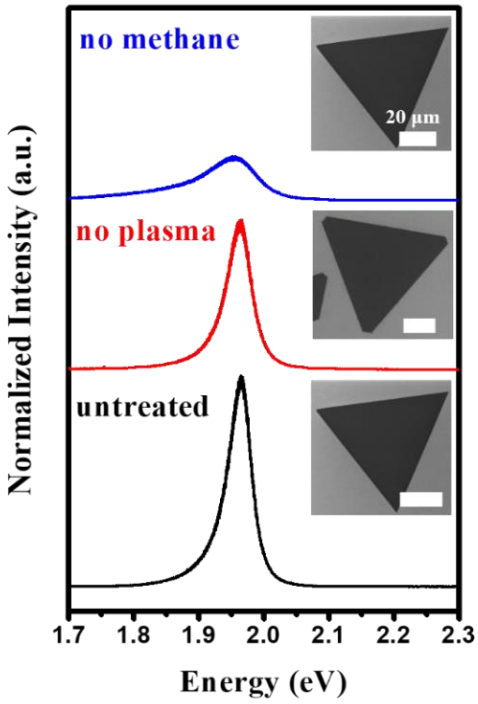

Figure 5- 2 Photoluminescence (PL) responses of reference samples. Pristine WS_2 (bottom), WS_2 annealed at 400°C in a CH_4 environment (middle), and Ar/H_2 plasma treated WS_2 in the absence of CH_4 (top). As CH_4 cannot be thermally decomposed at 400°C in the absence of plasma, the spectra from heat treated and pristine samples are very similar. Ar/H_2 plasma treatment (without CH_4) causes sulfur atoms to be sputtered away from WS_2, therefore the top panel shows both a quenching and a defect related shoulder in the PL response, as expected. In all panels, insets exhibit the corresponding scanning electron microscopy (SEM) images of the WS_2, showing no morphology changes among these three different samples.

Representative Raman spectra of the pristine and carbon-doped samples are shown in Fig. 5-1d. Besides the two first order characteristic Raman signatures of pristine WS_2 monolayers, the E'(Γ) and A_1'(Γ) located at 355 and 417 cm^{-1}, respectively, a high-intensity second-order double resonance peak involving two longitudinal acoustic phonons (2LA(M) mode) was detected when exciting the samples with a 514 nm laser.[27] To our surprise, such a double resonant process was progressively suppressed when increasing the CH_4 flow, as observed in the spectra obtained from all of the carbon-doped samples (see Fig. 5-1d). We believe that carbon dopants induced changes in the WS_2 electronic structure, which drive the system out of resonance for both the electron-phonon and hole-phonon mediated processes.[27] In particular, one LA phonon and one-defect elastic

scattering are involved in the double resonance process that give rise to the LA(M) and the LA(K) modes at 176 cm^{-1} and 188 cm^{-1}, respectively.[28] Both defect activated modes are present in the doped samples, which provides further evidence of lattice deformation induced by either vacancies or dopants.[28] It is noteworthy that samples treated in the presence of 8 sccm of CH_4 (the highest flow used in this study) preserves the characteristic Raman signature of WS_2 and exhibits the highest intensity for the LA(M) and LA(K) bands among all of the samples. Moreover, the PL on this heavily-doped sample is quenched (Fig. 5-3c and d).

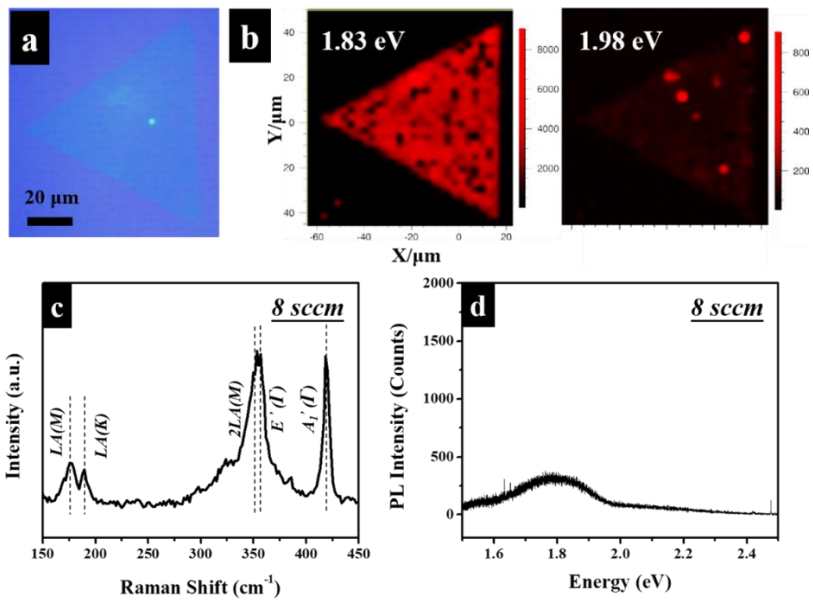

Figure 5- 3 (a) and (b) show the uniformity of the PL of the carbon-doped WS_2 @ 5sccm, measured with a 488 nm laser. (a) Optical image of a WS_2 triangular monolayer. (b) PL mappings showing the intensity of the response at 1.83 eV and 1.98eV, respectively. The mapping at 1.83 exhibits a mostly uniform PL signal, with the exception a few areas with local structural defects (such as holes in the triangles) or undoped parts (that emit at 1.98 eV). (c) Raman and (d) PL of heavily-carbon-doped WS_2 (@ 8sccm). Extra carbon doping may result in severe PL quenching but the characteristic Raman signatures of WS_2 are preserved.

The chemical bonding environment of carbon in monolayer WS_2 was also investigated by X-ray photoelectron spectroscopy (XPS, see Fig. 5-4). Survey scans and high-resolution C1s and W4f spectra were obtained from pristine and carbon-doped WS_2 monolayers. The high-resolution line scans were used to estimate the total atomic percentage of carbon in the samples and it was

found to increase from 1.98 at.% to *c.a.* 5.33 at.% for the carbon-doped WS_2 sample (@ 5sccm). Assuming that undoped WS_2 has only adventitious carbon, we estimate the carbon atomic percentage incorporated in the WS_2 sample to be *c.a.* 3.3 at.%. As the carbon content of the doped samples increases, we also observed a reduction in both the oxygen content and S/W ratio (composition table shown in Fig. 5-4). The carbon incorporation also reduces the energy of the valence band maximum (VBM) to the Fermi level (FL), as indicated in Fig. 5-5. The red shifts in the A excitonic transition observed in the ultraviolet–visible spectra (UV-vis, Fig. 5-6), further support the bandgap reduction due to carbon doping.

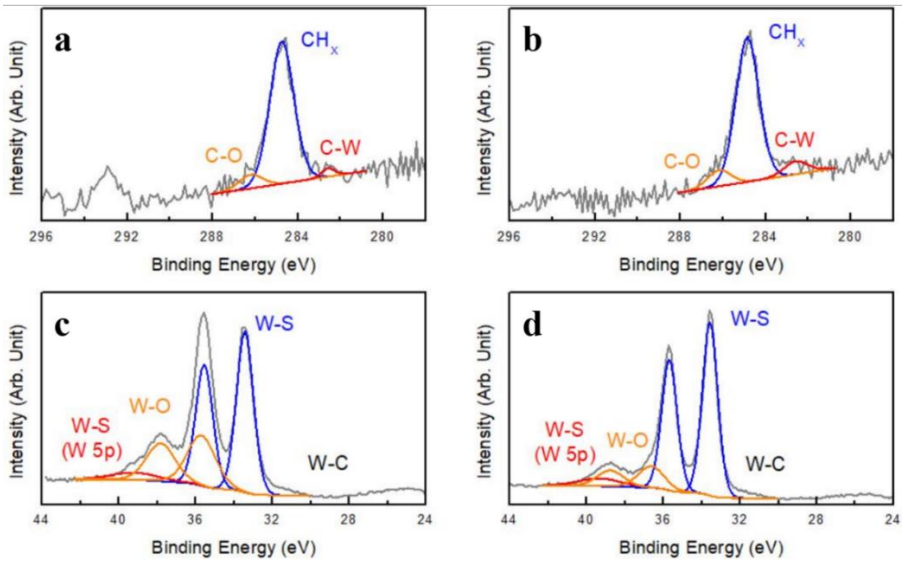

at. %	Si	O	S	W as WS_2	W as WO_3	C	C as W-C	C in WS_2
Pristine	23.5	50.0	11.1	4.9	2.1	8.0	0.22	1.98
Doped	21.9	43.2	15.0	8.0	1.3	10.4	0.80	5.33

Figure 5- 4 X-ray photoelectron spectroscopy (XPS) elemental analyses of pristine WS_2 (a) C 1s, (c) W 4f, and carbon-doped WS_2 (b) C 1s and (d) W 4f core levels. The table list shows elemental compositions in both the pristine and carbon-doped WS_2. The carbon exists on the material surface mostly in the form of CH_X and CO_X (intense peak centered at ~ 284.8 eV). The C 1s line scans show that the carbon in the form of carbide bonding (red curve at around 282.5 eV) increased three times after doping, which indicates the formation of the new W-C bonds that substitute sulfur atoms in the WS_2 lattice. We have also characterized and compared the pristine WS_2 and carbon-doped WS_2 samples by ToF-SIMS (Time of Flight Secondary Ion Mass Spectrometry), and FTIR (Fourier Transform Infrared Spectroscopy). The low signal to noise ratio lead to difficulties in detecting the characteristic features from doped carbon species.

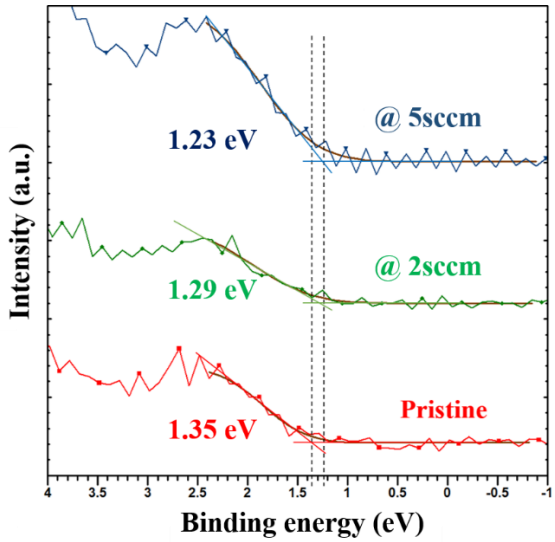

Figure 5- 5 Valence band maximum of the carbon-doped WS_2. The carbon incorporation into WS_2 gradually saturates the sulfur vacancies, thus decreasing the energy of the valence band maximum (VBM) to the Fermi level (FL), as shown in the figure, from 1.35 eV (pristine) to 1.29 eV (doped @2 sccm) and 1.23 eV (doped @5 sccm). All three spectra show similar valence band signatures of WS_2 that indicate that the binding energy shift was induced by carbon doping in WS_2.

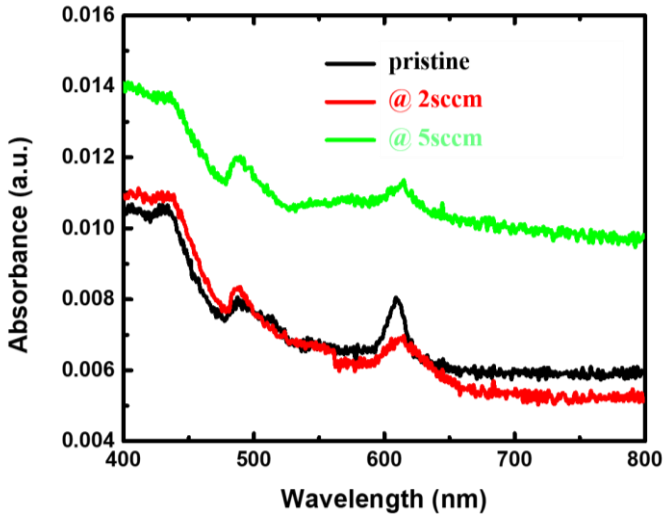

Figure 5- 6 UV-Vis spectra of the carbon-doped WS_2 samples transferred onto quartz substrates. The A exciton can be observed at 608 nm (2.039 eV) in the as grown WS_2, which corresponds to the excitonic absorption at the K point of the Brillouin zone. This is one of the characteristic absorption peaks of the monolayered WS_2. As the percentage of C in WS_2 increases, the A excitonic transition gradually shifts from 2.039 eV (608 nm) to 2.020 eV (614 nm) in lightly-doped WS_2 (@2 sccm), and 2.016 eV (615 nm) in medium-doped WS_2(@5 sccm). The red shifts in the A excitonic transitions further support the bandgap reduction via C doping.

5.3 Density functional theory calculations understanding of carbon doped WS_2

Density functional theory (DFT) calculations were performed in order to further investigate the bonding environment of the carbon dopants, the associated electronic structure of the carbon doped WS_2 systems and the mechanism responsible for the changes observed in the optical band gap. We only considered the V_S case for our DFT calculations, assuming that carbon and hydrocarbon radicals are present during the WS_2 plasma treatment, carbon atoms, CH or CH_2 molecules are introduced into the WS_2 in the V_S positions. correspond to placing the carbon at the sulfur position (α position), placing it at the preferred W-C bond length in bulk tungsten carbide of 2.12 Å (γ position), and placing the carbon at a vertical location that is intermediate between α and γ (β position), depicted in Fig. 5-7. The cohesive energy of the systems for each type of carbon dopant in every vertical position (α, β or γ) are provided in Table 5-1. Our results indicate that the lowest cohesive energy results when the CH species are located in the β position of the WS_2 followed closely by WS_2 with CH_2 species introduced in the α and β positions.

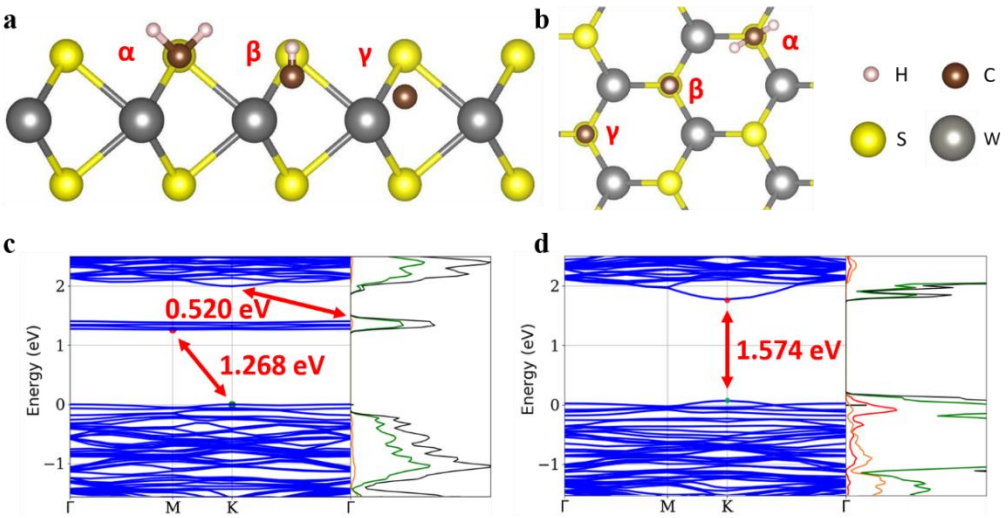

Figure 5- 7 Simulations of possible doping positions and band structures. Side (a) and top (b) views of α, β, and γ doping position for the proposed carbon species: C, CH and CH_2. The band structure and density of states of (c) WS_2 with 2.67 at% single-vacancies, (d) CH-doped WS_2 with the dopant at the β position. In the density of states, the p-orbitals of the carbon atom and the tungsten atom, the d-orbital of the tungsten atom, and total density of states are illustrated in different colors.

Premade Vacancy Type	Type of Doping Group	Cohesive Energy Comparison (eV/atom)		
		Doped C Position		
		α	β	γ
Single Vacancy	C	0.185	0.124	0.134
	CH	0.119	0.088	0.146
	CH_2	0.090	0.090	0.196

Table 5- 1 Relative cohesive energies of defective, doped WS_2 systems. The reference cohesive energy state is that of the pristine WS_2, the α, β, and γ doping position for the proposed carbon species: C, CH and CH_2 are schematically shown in Fig. 5-7.

The calculated band gap of pristine WS_2 was 1.791 eV. Thus, V_S behaves like an n-type dopant in agreement with a previous report.[31] Figure 5-7d exhibits the band structure of carbon-doped WS_2 with the CH-dopant occupying the β position. When compared to pristine WS_2, the band gap of the carbon-doped WS_2 was predicted to remain a direct band gap system, which energy value decreased by 0.217 eV. Moreover, the density of states (DOS) further indicates that the acceptor level rose above the original valence band for carbon-doped WS_2, so that extra holes moved up to higher energy levels, thus shrinking the band gap. In this instance, the doping group CH acted as a p-type dopant. The d-orbital of W and p-orbital of C dominated the contribution of the energy level of the top valence band, indicating an emerging bond between W and C to be the main reason for the band gap reduction.

5.4 Transmission electron microscopy study of carbon doped WS_2

High angle annular dark field (HAADF)-STEM imaging was used to confirm the presence of carbon dopants at the V_S sites (shown in Fig. 5-8). The experimental atomic resolution HAADF-

STEM image of a carbon-doped WS_2 monolayer (show in large area Fig. 5-8a, Vs in 5-8d and carbon doping (@ 5sccm) in 5-8e, respectively), reveals the existence of V_S in the hexagonal lattice, due to the growth process and/or post-growth plasma treatment. A portion of sulfur single-vacancies were occupied by one CH unit (CH@V_S, consistent with simulations). According to our STEM simulations, a slight yet clear intensity contrast difference can be generated after a CH unit occupies a V_S, due to the Z-contrast imaging mechanism of STEM[32], (Figs. 5-8f-h). The intensity profiles in Figs. 5-8b and c, depict the contrast difference between the V_S and CH@V_S, and are in good agreement with simulations. As the samples were transferred using a polymer film as a support layer, some areas had contamination and the intensity profile line-scan and analyses avoid the contaminated polymer residue regions (which can be easily distinguished from the background), in order to preserve atomic cleanness of the selected experimental images areas. When comparing these experimental images and our STEM image calculation results (Fig. 5-8h), there is a slight difference in the intensity (for both W and S) that originates from aberrations and astigmatism in TEM; such mismatch between STEM simulation and experimental direct measurements is inherent to the thermal and beam induced vibration of the atoms and it is, therefore, unavoidable.

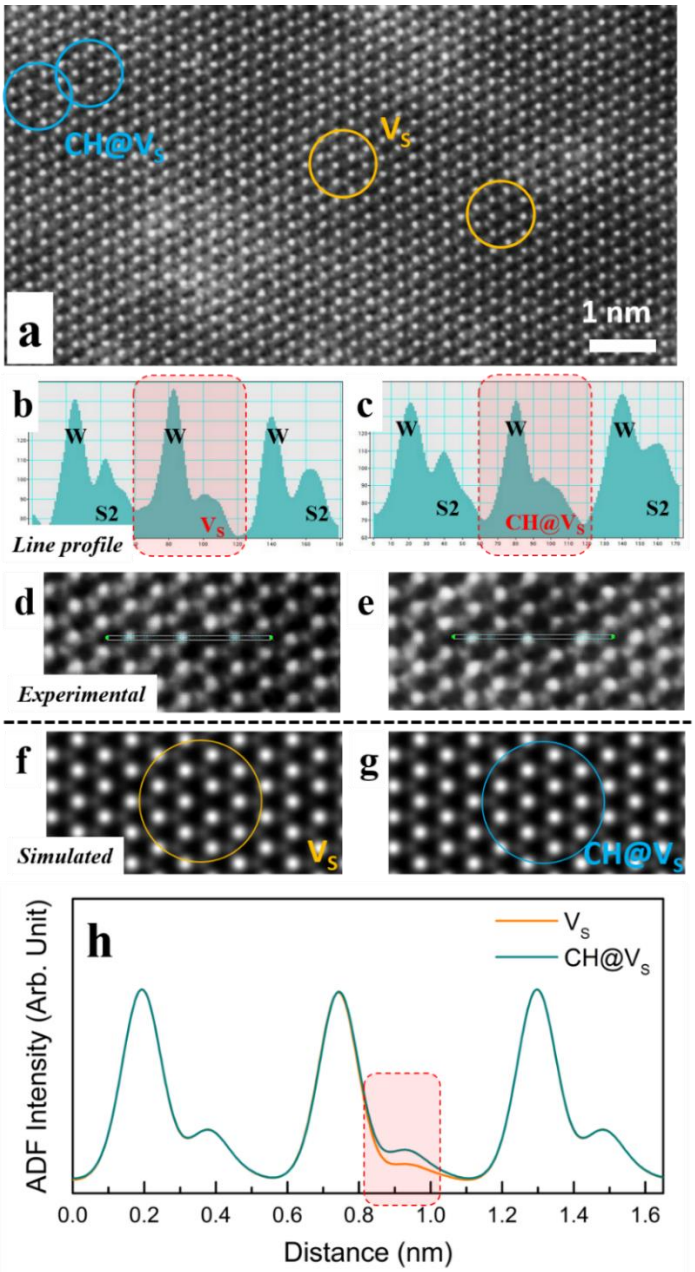

Figure 5- 8 TEM evidence of carbon doping in WS_2. Comparison between simulated and experimental high angle annular dark field (HAADF)-STEM images (the case of sulfur vacancies, and a CH dopant occupying a sulfur vacancy). Experimental atomic resolution HAADF-STEM image of the carbon-doped monolayer WS_2 (a) shows an area with both sulfur vacancies (V_S, yellow circles) and the CH dopant occupied sulfur single-vacancies (CH@V_S, blue circles) in the carbon-doped monolayer WS_2 (b) and (d) show the sulfur vacancies and its corresponding intensity line profiles, (c) and (e) the CH@V_S and its corresponding intensity line profiles; Simulated HAADF-STEM image of the carbon-doped monolayer WS_2 with (f) V_S, and (g) the CH@V_S in the hexagonal lattice; (h) Intensity line profile of the STEM image simulations with V_S, and CH@V_S in the doped monolayer WS_2.

5.5 Transport characteristics of carbon doped WS_2

Pristine and WS_2 monolayers with varying levels, lightly-, medium- and heavily-doped respectively, were integrated in back-gated field effect transistors (FETs) in order to investigate their transport characteristics. Figure 5-9a depicts a SEM image of a FET device, with a 50 nm Al_2O_3 gate dielectric, a channel length of 1 µm and a channel width equal to the width of the triangular flake (~50-100 µm). Drain currents (I_{DS}) *versus* back gate voltages (V_{BG}) at a drain voltage (V_{DS}) of 1V are shown in Figs. 5-9b-e for all 10 pristine, 13 lightly-doped, 13 medium-doped and 10 heavily-doped WS_2 devices, respectively. The mobility cannot properly be extracted since most of the devices do not consistently reach the full ON state, i.e. there is no linear region of the I_{DS} vs. V_{BG}. However, the electron mobility is estimated to be between ~0.1-1 cm^2/V-s from the few which exhibit a linear behavior.

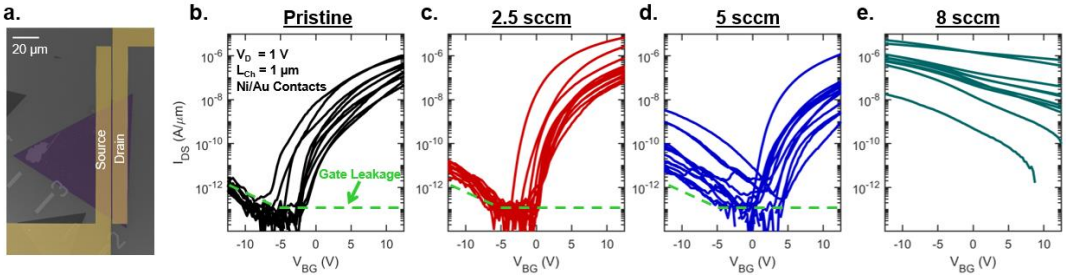

Figure 5- 9 FET characteristics of pristine and carbon-doped monolayer WS_2. (a) False-colored SEM image of a representative FET with a channel length (LCh) of 1 µm with 40 nm Ni/ 30 nm Au contacts on a 50 nm ALD Al_2O_3/Pt/TiN/Si substrate. Drain voltage (I_{DS}) versus back gate voltage (V_{BG}) with a drain voltage (V_D) of 1 V for FETs fabricated with (b) pristine, (c) lightly-doped (2.5 sccm), (d) medium-doped (5 sccm), and (e) heavily-doped (8 sccm) WS_2, respectively. Each curve corresponds to a different device. The green dashed line indicates the gate leakage current level and any drain current below this level is not the true I_{DS}. The pristine, lightly- and medium-doped (b-d) are primarily n-type indicating the contact Fermi level pinning is preventing hole injection into the channel. The medium-doped samples (d) begin to show some ambipolar p-type conduction. The heavily-doped device (e) reveals entirely p-type behavior and enhanced hole injection from the contacts.

The pristine WS_2 devices exhibited unipolar n-type behavior with an ON/OFF ratio $>10^6$ for the n-branch ($V_{BG}>0$), indicating that the metal Fermi level (E_F) pins closer to the WS_2

conduction band (E_C) than the valence band (E_V), thus resulting in a smaller electron Schottky barrier height (Φ_{SB-n}) than hole Schottky barrier height (Φ_{SB-p}).[33] Note that green dashed lines in Figs. 5-9b-e denote the approximate gate leakage current. For the pristine samples in Fig. 5-9b, the current seen at V_{BG}<-5 is not the true device current and thus is not an indication of hole conduction. However, a low current p-branch corresponding to hole conduction begins to emerge as the carbon doping is gradually introduced, as observed in the lightly- and medium-doped devices shown in Figs. 5-9c and d, respectively. For the medium-doped samples shown in Fig. 5-9d, significant device to device variation (due to variation of plasma power) is observed but many devices have nearly symmetric n-branches and p-branches. The ambipolar characteristics thus indicate that as the degree of doping increases, the tunnel barrier height for the holes, and thus Φ_{SB-p}, decreases as shown schematically in Fig. 5-10. This arises from one or a combination of two mechanisms. The sum of the electron and hole Schottky barriers equals the band gap (Φ_{SB-n}+ Φ_{SB-p}=E_G). As E_G decreases, either Φ_{SB-n}, Φ_{SB-p}, or both can decrease. Moreover, the energy level at which the metal Fermi level pins relative to the WS_2 conduction and valence band can change. For a given E_G, a decrease in Φ_{SB-p} will accompany an increase Φ_{SB-n}, and a reduction in the n-branch current. The emergence of the p-branch when comparing the pristine, lightly-doped and medium-doped devices is difficult to attribute to either single mechanism. Any changes in Φ_{SB-n} that affect the n-branch ON current are easily obscured upon variation in the subthreshold slope (SS), which is heavily affected by the interface quality and potentially the doping procedure.

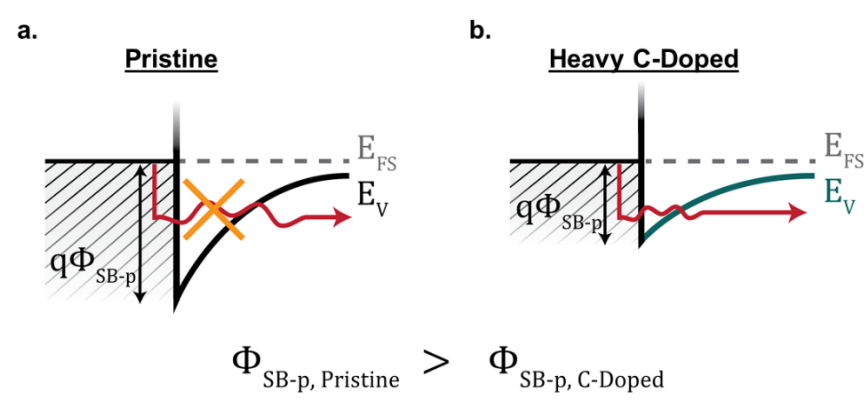

Figure 5- 10 Band diagram showing the change in Fermi level pinning. Schematic of the valence band position (E_V) near the source for a (a) pristine and (b) carbon-doped FET (@ 8sccm), respectively. For the pristine devices, a tall and wide Schottky tunnel barrier (Φ_{SB-p}) prevents any hole conduction and hence no p-branch is observed. Conversely, after heavy doping (@ 8sccm), the metal Fermi level pins closer to the WS_2 valence band. Thus, heavily-doped samples have a smaller Schottky barrier height for hole injection and, therefore, exhibit significant hole conduction.

The heavily carbon-doped devices exhibit an entirely p-type hole when compared to lower-doped samples. At V_{BG} = 0V, the devices are now in the ON state since the doping has now pushed the Fermi level close to the valence band. This heavy doping accompanied by the realignment of the metal-WS_2 Fermi level pinning results in a significantly decreased Φ_{SB-p}. The hole injection is no longer blocked by a large Schottky tunnel barrier. This is evident in the linear I_{DS} vs. V_{DS} characteristics shown in Fig. 5-11. Although the currents are relatively large, ~1 µA/µm, at V_{BG} = -12 V, the device cannot be turned off at positive V_{BG}. This indicates that the CH_4 plasma treatment using 8 sccm CH_4 flow rate, decreased the WS_2/Al_2O_3 coupling, slowing the band movement due to the creation of interface trap states. This degradation only appears at the highest doping level. In fact, the samples treated with 2.5 sccm CH_4 flow rate have shown an improved SS when compared to the pristine samples, possibly due to an annealing effect occurring during the 400°C doping treatment. A true post growth substitutional doping scheme such as the novel carbon doping presented here is required in order to achieve such doping profiles in TMD-based FETs, as a traditional surface electrostatic doping approach would be insufficient.

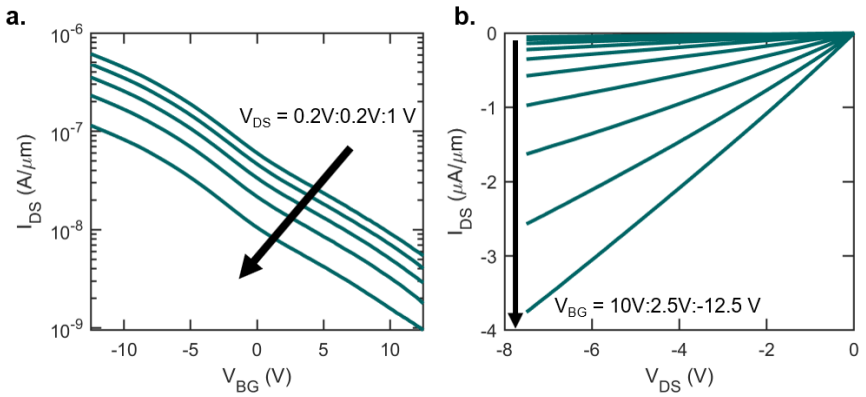

Figure 5- 11 Transfer and output characteristics of a doped WS_2–based FET (@8 sccm CH_4). (a) Drain voltage (I_{DS}) versus back gate voltage (V_{BG}) and (b) I_{DS} versus drain voltage (V_{DS}). The device shows heavy p-doping and linear I_{DS} versus V_{DS} characteristics, indicating the metal-WS_2 Fermi level is pinned relatively close to the valence band.

5.6 Chapter Summary

In this chapter we have successfully incorporated carbon-hydrogen groups within sulfur single-vacancies of WS_2 following a novel plasma-assisted approach. This two-step strategy does not involve high temperatures for the doping step (only 400°C). Moreover, we have clearly demonstrated that the carbon-doped monolayers of WS_2 exhibit optical and electronic properties that could be tuned depending on the carbon content. The PL measurements indicated that the band gap could be reduced by 150 meV, when compared to that of the pristine WS_2 monolayer. Additionally, AC-HRSTEM imaging and DFT calculations confirmed the presence of covalently bonded carbon-hydrogen groups within the WS_2 lattice. Furthermore, we performed a detailed electrical characterization, which indicates that the carbon-hydrogen groups within WS_2 lead to a p-type doping conductor. CMOS devices are engineered to be unipolar, and require n-type and p-type carrier transport for the N-MOS and P-MOS transistors using n+/p/n+ and p+/n/p+ substitutional doping schemes, respectively. Therefore, the demonstrated substitutional p-doping

presented here constitutes a significant step towards complementary metal-oxide semiconductor (CMOS) logic circuits based on TMD materials.

5.7 References

1. Wang, Q. H.; Kalantar-Zadeh, K.; Kis, A.; Coleman, J. N.; Strano, M. S., Electronics and optoelectronics of two-dimensional transition metal dichalcogenides. *Nature nanotechnology* **2012,** *7* (11), 699-712.

2. Ma, Y.; Dai, Y.; Guo, M.; Niu, C.; Lu, J.; Huang, B., Electronic and magnetic properties of perfect, vacancy-doped, and nonmetal adsorbed $MoSe_2$, $MoTe_2$ and WS_2 monolayers. *Physical Chemistry Chemical Physics* **2011,** *13* (34), 15546-15553.

3. Koppens, F.; Mueller, T.; Avouris, P.; Ferrari, A.; Vitiello, M.; Polini, M., Photodetectors based on graphene, other two-dimensional materials and hybrid systems. *Nature nanotechnology* **2014,** *9* (10), 780.

4. Sreeprasad, T.; Nguyen, P.; Kim, N.; Berry, V., Controlled, defect-guided, metal-nanoparticle incorporation onto MoS_2 via chemical and microwave routes: electrical, thermal, and structural properties. *Nano letters* **2013,** *13* (9), 4434-4441.

5. Komsa, H.-P.; Krasheninnikov, A. V., Two-dimensional transition metal dichalcogenide alloys: stability and electronic properties. *The journal of physical chemistry letters* **2012,** *3* (23), 3652-3656.

6. Kang, J.; Tongay, S.; Li, J.; Wu, J., Monolayer semiconducting transition metal dichalcogenide alloys: Stability and band bowing. *Journal of Applied Physics* **2013,** *113* (14), 143703.

7. Klee, V.; Preciado, E.; Barroso, D.; Nguyen, A. E.; Lee, C.; Erickson, K. J.; Triplett, M.; Davis, B.; Lu, I.-H.; Bobek, S., Superlinear Composition-Dependent Photocurrent in CVD-Grown

Monolayer $MoS_{2(1-x)}Se_{2x}$ Alloy Devices. *Nano letters* **2015,** *15* (4), 2612-2619.

8. Azizi, A.; Wang, Y.; Lin, Z.; Wang, K.; Elias, A. L.; Terrones, M.; Crespi, V. H.; Alem, N., Spontaneous formation of atomically thin stripes in transition metal dichalcogenide monolayers. *Nano letters* **2016,** *16* (11), 6982-6987.

9. Xia, B.; Liu, P.; Liu, Y.; Gao, D.; Xue, D.; Ding, J., Re doping induced 2H-1T phase transformation and ferromagnetism in MoS_2 nanosheets. *Applied Physics Letters* **2018,** *113* (1), 013101.

10. Laskar, M. R.; Nath, D. N.; Ma, L.; Lee, E. W.; Lee, C. H.; Kent, T.; Yang, Z.; Mishra, R.; Roldan, M. A.; Idrobo, J.-C., p-type doping of MoS_2 thin films using Nb. *Applied Physics Letters* **2014,** *104* (9), 092104.

11. Chua, X. J.; Luxa, J.; Eng, A. Y. S.; Tan, S. M.; Sofer, Z. k.; Pumera, M., Negative electrocatalytic effects of p-doping niobium and tantalum on MoS_2 and WS_2 for the hydrogen evolution reaction and oxygen reduction reaction. *ACS Catalysis* **2016,** *6* (9), 5724-5734.

12. Nipane, A.; Karmakar, D.; Kaushik, N.; Karande, S.; Lodha, S., Few-layer MoS_2 p-type devices enabled by selective doping using low energy phosphorus implantation. *ACS nano* **2016,** *10* (2), 2128-2137.

13. Tongay, S.; Zhou, J.; Ataca, C.; Liu, J.; Kang, J. S.; Matthews, T. S.; You, L.; Li, J.; Grossman, J. C.; Wu, J., Broad-range modulation of light emission in two-dimensional semiconductors by molecular physisorption gating. *Nano letters* **2013,** *13* (6), 2831-2836.

14. Azcatl, A.; Qin, X.; Prakash, A.; Zhang, C.; Cheng, L.; Wang, Q.; Lu, N.; Kim, M. J.; Kim, J.; Cho, K., Covalent nitrogen doping and compressive strain in MoS_2 by remote N_2 plasma exposure. *Nano letters* **2016,** *16* (9), 5437-5443.

15. Yang, L. W.; Wright, P.; Eu, V.; Lu, Z.; Majerfeld, A., Heavily doped p-GaAs grown by low-pressure organometallic vapor phase epitaxy using liquid CCl_4. *Journal of applied physics* **1992,** *72* (5), 2063-2065.

16. Lian, P.; Yin, T.; Xu, Z.; Zhao, H.; Zou, D.; Gao, G.; Du, J.; Chen, C.; Tao, C.; Chen, J. In *High-quality carbon-doped GaAs/AlGaAs material growth in MOCVD and its application for optoelectronic devices*, Semiconductor Lasers III, International Society for Optics and Photonics: 1998; pp 278-285.

17. Wu, J.; Ma, L.; Samanta, A.; Liu, M.; Li, B.; Yang, Y.; Yuan, J.; Zhang, J.; Gong, Y.; Lou, J., Growth of Molybdenum Carbide–Graphene Hybrids from Molybdenum Disulfide Atomic Layer Template. *Advanced Materials Interfaces* **2017,** *4* (4).

18. Hai, Z.; Du, J.; Akbari, M. K.; Xue, C.; Xu, H.; Zhuiykov, S., Carbon-doped MoS_2 nanosheet photocatalysts for efficient degradation of methyl orange. *Ionics* **2017**, 1-5.

19. Jeon, J.; Park, Y.; Choi, S.; Lee, J.; Lim, S. S.; Lee, B. H.; Song, Y. J.; Cho, J. H.; Jang, Y. H.; Lee, S., Epitaxial synthesis of molybdenum carbide and formation of a Mo_2C/MoS_2 hybrid structure via chemical conversion of molybdenum disulfide. *ACS nano* **2018**.

20. Yue, Q.; Chang, S.; Qin, S.; Li, J., Functionalization of monolayer MoS_2 by substitutional doping: a first-principles study. *Physics Letters A* **2013,** *377* (19), 1362-1367.

21. Hu, A.-M.; Wang, L.-l.; Xiao, W.-Z.; Xiao, G.; Rong, Q.-Y., Electronic structures and magnetic properties in nonmetallic element substituted MoS_2 monolayer. *Computational Materials Science* **2015,** *107*, 72-78.

22. Pierucci, D.; Henck, H.; Ben Aziza, Z.; Naylor, C. H.; Balan, A.; Rault, J. E.; Silly, M. G.; Dappe, Y. J.; Bertran, F.; Le Fèvre, P., Tunable Doping in Hydrogenated Single Layered Molybdenum Disulfide. *ACS nano* **2017,** *11* (2), 1755-1761.

23. Ma, K. Y.; Yoon, S. I.; Jang, A.-R.; Jeong, H. Y.; Kim, Y.-J.; Nayak, P. K.; Shin, H. S., Hydrogenation of monolayer molybdenum diselenide via hydrogen plasma treatment. *Journal of Materials Chemistry C* **2017,** *5* (43), 11294-11300.

24. Chen, M.; Nam, H.; Wi, S.; Ji, L.; Ren, X.; Bian, L.; Lu, S.; Liang, X., Stable few-layer MoS_2 rectifying diodes formed by plasma-assisted doping. *Applied Physics Letters* **2013,** *103* (14),

142110.

25. Hamedani, Y.; Macha, P.; Bunning, T. J.; Naik, R. R.; Vasudev, M. C., Plasma-Enhanced Chemical Vapor Deposition: Where we are and the Outlook for the Future. In *Chemical Vapor Deposition-Recent Advances and Applications in Optical, Solar Cells and Solid State Devices*, InTech: 2016.

26. Cong, C.; Shang, J.; Wu, X.; Cao, B.; Peimyoo, N.; Qiu, C.; Sun, L.; Yu, T., Synthesis and Optical Properties of Large-Area Single-Crystalline 2D Semiconductor WS_2 Monolayer from Chemical Vapor Deposition. *Advanced Optical Materials* **2014,** *2* (2), 131-136.

27. Berkdemir, A.; Gutiérrez, H. R.; Botello-Méndez, A. R.; Perea-López, N.; Elías, A. L.; Chia, C.-I.; Wang, B.; Crespi, V. H.; López-Urías, F.; Charlier, J.-C., Identification of individual and few layers of WS_2 using Raman Spectroscopy. *Scientific reports* **2013,** *3*.

28. Carvalho, B. R.; Wang, Y.; Mignuzzi, S.; Roy, D.; Terrones, M.; Fantini, C.; Crespi, V. H.; Malard, L. M.; Pimenta, M. A., Intervalley scattering by acoustic phonons in two-dimensional MoS_2 revealed by double-resonance Raman spectroscopy. *Nature communications* **2017,** *8*, 14670.

29. Carozo, V.; Wang, Y.; Fujisawa, K.; Carvalho, B. R.; McCreary, A.; Feng, S.; Lin, Z.; Zhou, C.; Perea-López, N.; Elías, A. L., Optical identification of sulfur vacancies: Bound excitons at the edges of monolayer tungsten disulfide. *Science advances* **2017,** *3* (4), e1602813.

30. Lin, Z.; Carvalho, B. R.; Kahn, E.; Lv, R.; Rao, R.; Terrones, H.; Pimenta, M. A.; Terrones, M., Defect engineering of two-dimensional transition metal dichalcogenides. *2D Materials* **2016,** *3* (2), 022002.

31. Alexeev, E. M.; Catanzaro, A.; Skrypka, O. V.; Nayak, P. K.; Ahn, S.; Pak, S.; Lee, J.; Sohn, J. I.; Novoselov, K. S.; Shin, H. S., Imaging of interlayer coupling in van der Waals heterostructures using a bright-field optical microscope. *Nano letters* **2017,** *17* (9), 5342-5349.

32. Williams, D. B.; Carter, C. B., The transmission electron microscope. In *Transmission electron microscopy*, Springer: 1996; pp 3-17.

33. Schulman, D. S.; Arnold, A. J.; Das, S., Contact engineering for 2D materials and devices. *Chemical Society Reviews* **2018,** *47* (9), 3037-3058.

Chapter 6

One-Step Synthesis of Monolayer Vanadium-doped Tungsten Disulfide: An Emerging Room-Temperature Diluted Magnetic Semiconductor

This work was mainly supported by the Air Force Office of Scientific Research (AFOSR) through grant No. FA9550-18-1-0072 and the NSF-IUCRC Center for Atomically Thin Multifunctional Coatings (ATOMIC).

6.1 Introduction and Motivation

Diluted magnetic semiconductors (DMSs) have been realized in bulk III-V semiconductors such as GaAs by doping with magnetic ions (e.g. Mn[1]), with long efforts towards achieving room-temperature operation in the face of dopant clustering and phase segregation.[2,3] Pursuit of DMS behavior in two-dimensional (2D) transition metal dichalcogenides has recently burgeoned through the introduction of magnetic transition metal ions such as V[4], Ni[5], Co[6] and Mn[7] within the host lattice[8]. While density functional theory predicts tunable magnetism in V-doped MoS_2[9] and WS_2[10,11] monolayers at V concentrations as high as 9at.%., researchers have been unable to realize this experimentally[4]. Therefore, it is attractive to develop scalable and controllable synthesis routes for monolayer DMSs with intrinsic ferromagnetic ordering at room temperature. Understanding how spins order in such systems is the key to unlock the door to novel 2D magnets, with unprecedented magneto-electric and magneto-optical effects.[12,13,16]

Monolayer tungsten disulfide is a direct-gap transition metal dichalcogenide (TMD) with high photoluminescence yield[14] that can also achieve high on/off current ratio ($>10^5$) in field-effect transistor geometries[15]. Reliable substitutional cation doping of WS_2 (and its sister material MoS_2) can induce degenerate n-type (rhenium doping[16]) and p-type conduction (carbon[17] and niobium[18]

doping). Beyond simply introducing charge carriers, a judicious choice of dopant may also achieve qualitatively new functionalities such as spin polarization – this prospect is particularly enticing in the transition metal dichalcogenides, since the magnetic dopants typically used in diluted magnetic semiconductors are chemically similar to the cation species in TMDs.

We report the single-step powder vaporization synthesis of high-quality V-doped WS_2 monolayers with room-temperature ferromagnetism. Aberration-corrected high-resolution scanning transmission electron microscopy (AC-HRSTEM) and X-ray photoelectron spectroscopy (XPS) reveal substitutional vanadium concentrations up to 12at.%. without structural deformation or degradation. Vanadium doping reduces the optical bandgap and induces p-branch transport that reaches ambipolarity. What appears to be intrinsic ferromagnetic order is achieved at room temperature with maximum coercivity and saturation magnetization at an intermediate vanadium concentration (~2at.%.), which first-principles calculations suggest can be strengthened further by additional concentration tuning to maximize the distribution of dopant-dopant neighbor separations. These results establish a route to pursue room-temperature 2D spintronic devices.

6.2 One-step powder vaporization synthesis and elemental analyses of V-doped WS_2 monolayers

Pristine and V-doped WS_2 monolayers were synthesized by powder vaporization[19] with ammonium metatungstate ($(NH_4)_6H_2W_{12}O_{40}\cdot xH_2O$, AMT) and vanadium oxide sulfate ($VO[SO_4]$) acting as W/V cation precursors and sodium cholate ($C_{24}H_{39}NaO_5 \cdot xH_2O$) as a surfactant salt, all dissolved in DI water. $VO[SO_4]$ provides a direct supply of V^{4+} ions (i.e. oxovanadium, VO^{2+}), which may be key to achieving a wide range of substitutional V concentrations in WS_2. Results for

alternative precursors are following described (Fig. 6-1). The prepared solutions were spin-coated on oxidized Si substrates, followed by sulfidation at 800°C (Fig 6-2a). As-grown pristine and V-doped WS_2 monolayers have regular triangular shapes 10 to 50 μm across (Fig. 6-2b).

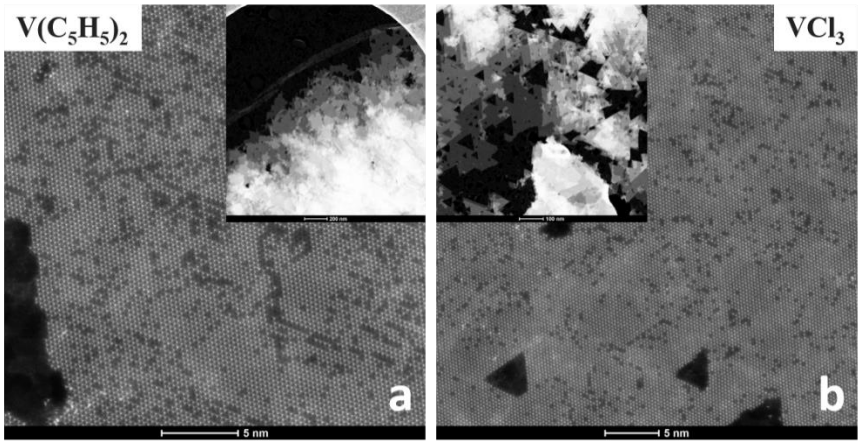

Figure 6- 1 HAADF-STEM image of V-doped WS_2 by V precursor of (a) $V(C_5H_5)_2$ and (b) VCl_3.

We studied several the vanadium precursors for doping WS_2 monolayers,

1. Vanadocene (II) ($V(C_5H_5)_2$), we realize the doping by powder vaporization method for the growth,[17] it could dope inside of the lattice with high concentration, however, there will show carbon contaminations or even a defective graphene layers underlying as-grown TMDs, as reported by other metal organic precursors.[20] The morphology is degraded which means it fails to form large area monolayer triangles. From the atomic resolution HAADF-STEM image of the highly-doped materials, we also see extensive stripes of V dopants in the lattice (Fig. 6-1a), which substantially affects the physical properties.

2. Vanadium (III) chloride (VCl_3), we realize the doping by powder vaporization method for the growth,[17] this precursor is very air sensitive so have to deal with inside the glove box, the doping could be also realized with high concentration doping level while the final morphology shows as WS_2 few layers filled with etched holes probably related with chloride (Fig. 6-1b).

3. Vanadium (IV) oxide sulfate ($VO[SO_4]$), is what we focused on for now, with different density of the precursor, we can dope into the TMDs as high as 12% of V with good morphology control discussed later in this chapter.

4. Vanadium (V) oxide (V_2O_5) is not working since they are very stable with extremely low vapor pressure thus hard to get sulfurized at least for sulfur vaporization.

5. Ammonium metavanadate (V) (NH_4VO_3), this precursor can be dissolved in DI-water in spin coated process, this precursor we have not tried but reported by a recent study,[4] the study claimed high concentration doping is possible yet no high quality large area monolayer triangles were found for higher doping concentration.

It is also noteworthy that the distribution of the transition metal dopants in the host TMD lattice is also highly dependent on the synthesis process, kinetically-driven powder vaporization process may result in the segregation and stripe formation of V dopants. Vanadium segregation and striping were consistently detected when using vanadocene ($V(C_5H_5)_2$) and vanadium (III) chloride (VCl_3) as precursors, which would significantly affect the magnetic properties of the materials discussed above by DFT calculations too.

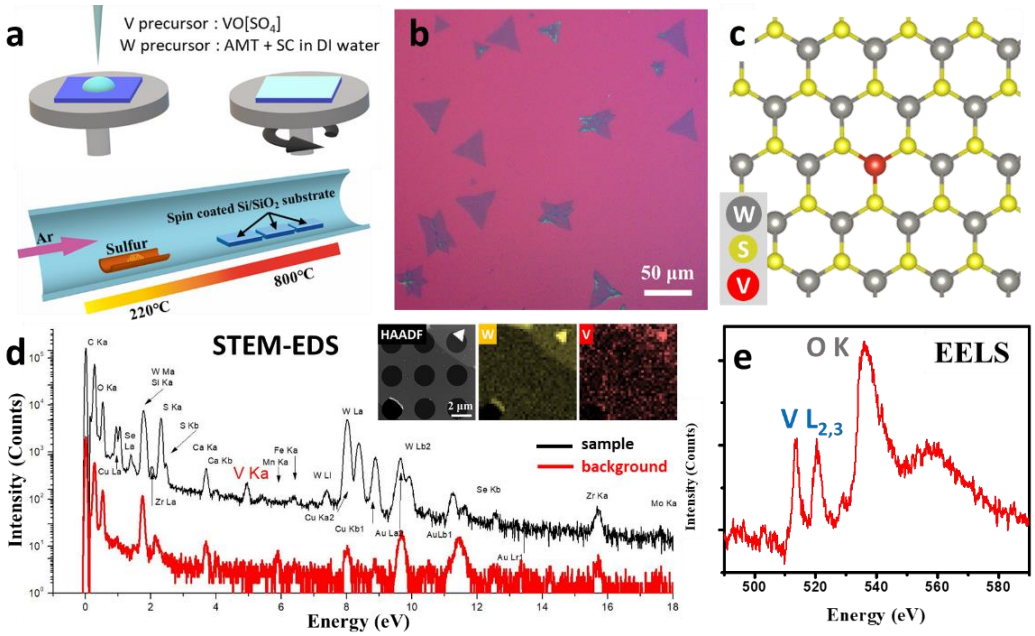

Figure 6- 2 One step synthesis of monolayer V-doped WS_2 and chemical analyses. (a) Schematics of the one-step synthesis of vanadium-doped tungsten disulfide; (b) Optical microscope image of triangular V-doped WS_2 monolayers; (c) Structure schematic of one V atom substitutional doping in WS_2 hexagonal lattice; (d) STEM/EDS spectrum of the monolayer V-doped WS_2, inset showing the STEM/EDS elemental mappings of the materials; (e) TEM/EELS measurement of vanadium $L_{2,3}$ edge, the inevitable oxygen peak is from oxidation of the sample surface and the film support.

Elemental fingerprints from TEM electron energy loss spectroscopy (EELS) using the vanadium $L_{2,3}$ edges at 513 eV and 521 eV (Fig. 6-2e) were further confirmed by the observation of a vanadium Kα peak *circa* 4.95 keV in STEM energy-dispersive X-ray spectroscopy (STEM/EDS, Fig. 6-2d) and XPS elemental analyses (Fig. 6-3). An oxygen peak is unavoidable in the EELS spectra, due to oxidation of the sample surface and film support. Keeping the overall volume of the precursor solution constant, the vanadium precursor concentration was varied from zero to 1×10^{-5}, 1×10^{-4} and 1×10^{-3} mol/L. XPS analysis measured overall doping levels of ~1.5at.% and ~10at.% for the 1×10^{-4} and 1×10^{-3} mol/L solutions, while the 1×10^{-5} sample was below the XPS detection limit. Direct enumeration of the local vanadium concentration by atomic resolution TEM (see discussion below) yields more sensitive results: 0at.%. vanadium for 0 mol/L solution

(i.e. pristine WS_2 monolayers) and average vanadium concentrations of 0.4, 2.0, and 8.0at.%. for V-WS_2 grown using the 1×10^{-5}, 1×10^{-4} and 1×10^{-3} mol/L solutions respectively.

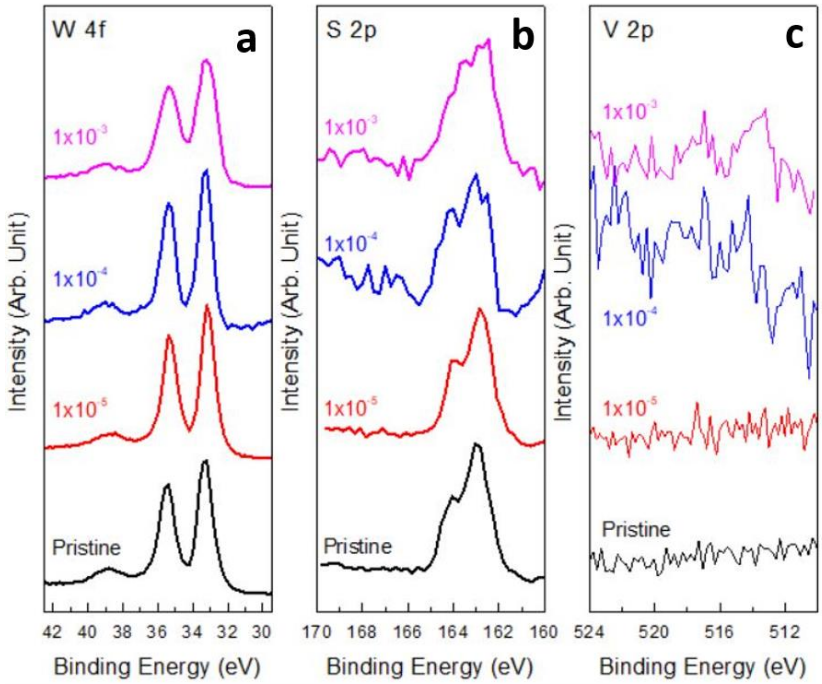

VO[SO_4]	C+O+Si	W	S	v	V % in WS_2
0	78.6	7.3	14.1	-	-
$1x10^{-5}$	80.5	6.9	12.6	-	-
$1x10^{-4}$	90.4	3.0	6.5	0.1	1.5%
$1x10^{-3}$	97.1	0.9	1.9	0.1	10%

Figure 6- 3 X-ray photoelectron spectroscopy (XPS) elemental analyses of pristine WS_2 and V-doped WS_2 (a) W 4f (b) C 1s and (c) V 2p core levels. The table list shows elemental compositions in both the pristine and V-doped WS_2.

6.3 Atomic resolution TEM investigation of V-doped WS_2 monolayers

High-angle annular dark field (HAADF)-STEM imaging in Fig. 6-4 confirms the presence of substitutional V atoms at W sites (written V_W) in the hexagonal lattice of WS_2. Under Z-contrast

imaging vanadium is straightforwardly distinguished from much heavier tungsten, and the vanadium concentration can then be extracted atom-by-atom from the HAADF-STEM images. The highest level of doping achieved was 12at.%. (synthesized with 5×10^{-3} mol/L of V precursor, Fig. 6-5). Further increase of the V precursor concentration triggered precipitation upon mixing the W and V precursor solutions, leading to degradation of the WS_2 monolayer's crystallinity and flatness. Although these deformed V-doped WS_2 layer indicate higher doping concentrations, their complex edges and highly defective structures make their physical characterization unreliable.[21]

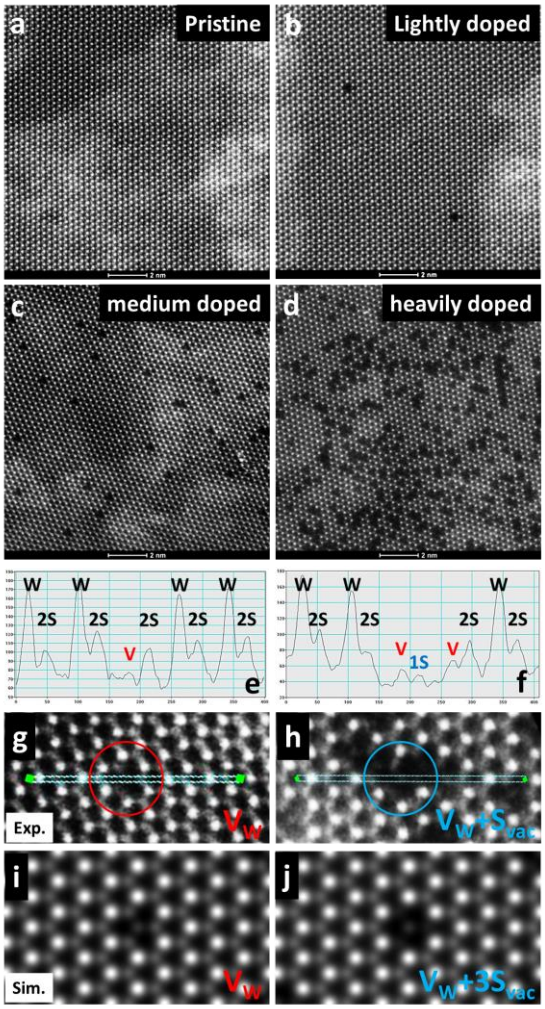

Figure 6- 4 Atomic resolution HAADF-STEM images of pristine and V-doped WS_2 monolayers. (a) pristine, (b) lightly-doped (0.4%), (c) moderately-doped (2%) and (d) heavily-doped (8%), respectively; scale bar = 2nm; Comparison between simulated and experimental high angle annular dark field (HAADF)-STEM images (the case of V substitutional dopant, and a V dopant coupled

with a sulfur vacancy). (g) and (e) Experimental atomic resolution HAADF-STEM images and corresponding intensity line profiles of the V-doped WS_2 monolayer contains a V substitutional dopant (red circled, defined as V_W) and (h) and (f) V dopant coupled with a sulfur vacancy (blue circled, defined as V_W+S_{vac}).

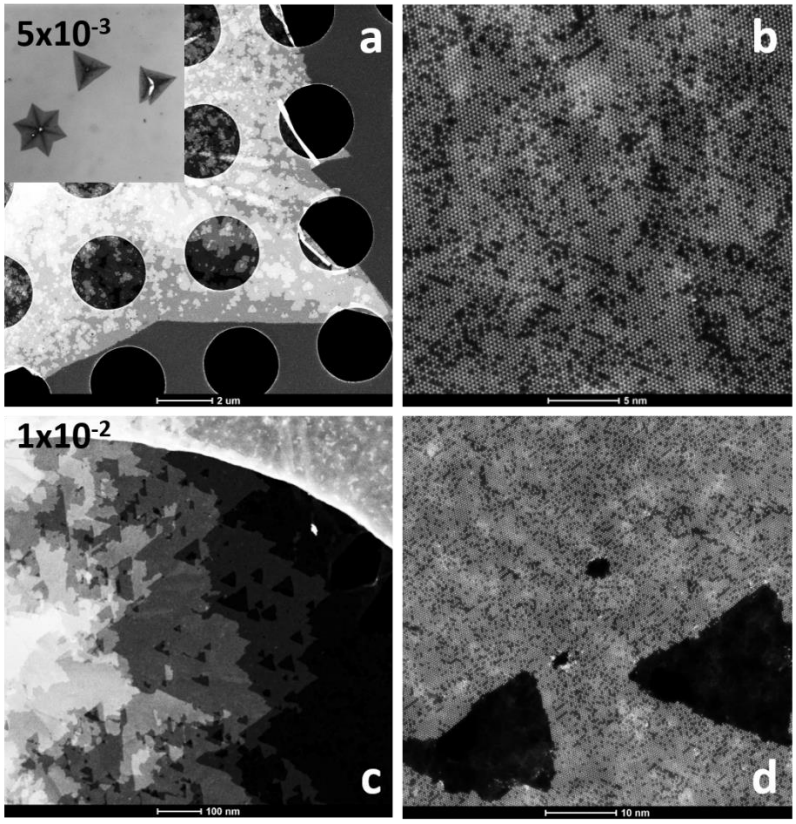

Figure 6- 5 Low-mag TEM images of over V-doped WS_2 monolayers at V precursor concentration at (a) $5x10^{-3}$ mol/L and (b) $1x10^{-2}$ mol/L, respectively; corresponding atomic resolution HAADF-STEM images shown in (b) and (d).

Moreover, dopant concentration gradient was observed by this single-step synthesis route (Fig. 6-6). Dopant aggregation (in e.g. stripes[21]) was only rarely seen, even in the 12at.%. vanadium monolayers. When comparing experimental STEM images with image simulations (Figs. 6-4e-j and 6-7), elemental identities can be clearly determined by contrast differences (W>2S>V>1S). When the V concentration is 8at.%. or higher (Fig. 6-8), vanadium atoms more likely to be coupled

with a sulfur vacancy (written V_W+S_{vac}), which is consistent with prior work on TMD alloys.[4,22] According to simulations, such defect coupling is energetically favorable, and the slight lattice distortion and strain induced by doping[22] could alter the electronic properties of the material.

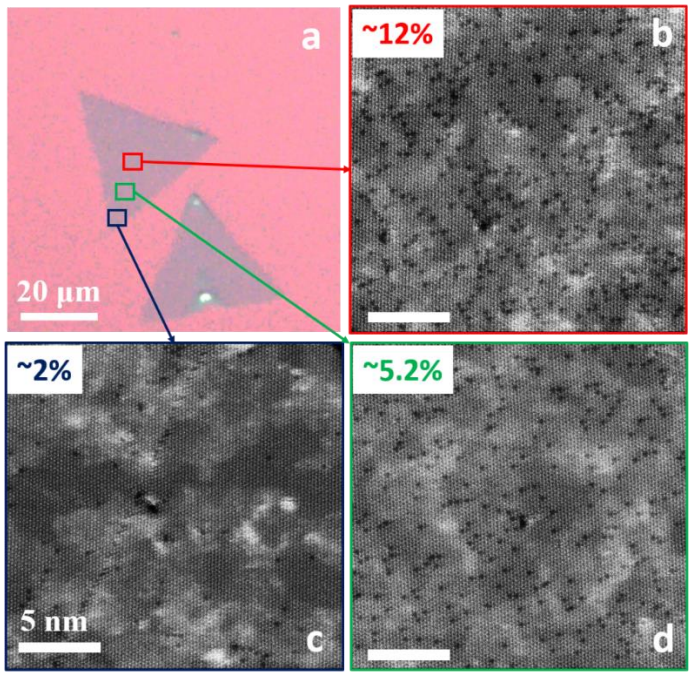

Figure 6- 6 Doping concentration gradient within heavily-doped monolayer WS_2 triangles.

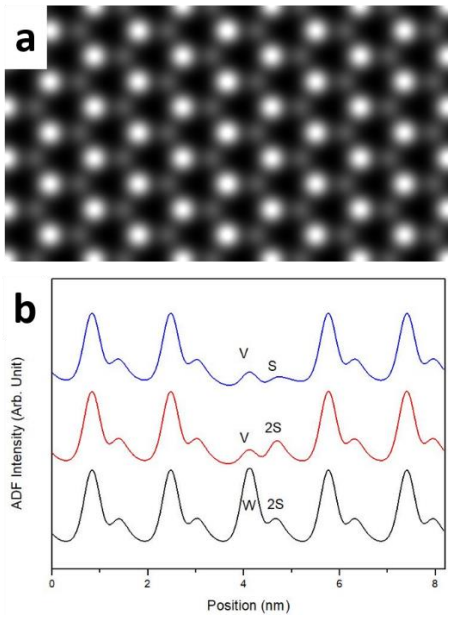

Figure 6- 7 (a) Simulated STEM image of pristine WS_2, (b) Intensity line profile of the STEM image simulations with pristine WS_2 lattice (black curve), V_W (red curve) and V_W+S_{vac} (blue curve), respectively.

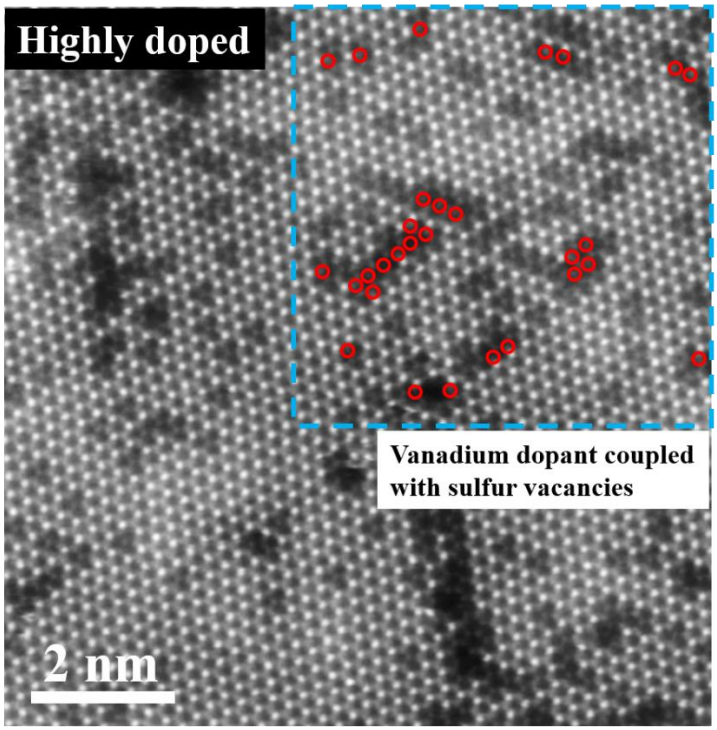

Figure 6- 8 Atomic resolution HAADF-STEM image of highly V-doped WS_2. Indexing of sulfur monovacancies by red circles, it is clear that the sulfur monovacancies tends to be coupled with V substitute dopants and even double V substitute dopants.

6.4 Optical, electronic and thermal transport properties of V-doped WS_2 monolayers

Representative Raman spectra of pristine and V-doped WS_2 monolayers were obtained for excitation wavelengths of 532 nm and 488 nm (Figs. 6-9a and b). Pristine WS_2 monolayers exhibit the representative E′(Γ) and A_1′(Γ) first-order phonon modes at 355 and 417 cm^{-1} respectively. In V-WS_2 samples, the defect-activated longitudinal acoustic mode (LA(M)) gradually emerges as the vanadium concentration increases, indicating lattice disorder induced by V dopants.[23] Both E′(Γ) and A_1′(Γ) blueshift as a function of vanadium concentration (Table 6-1). This is consistent with previously reported spectra of V-doped MoS_2, where the blueshift was attributed to electron-phonon coupling[24].

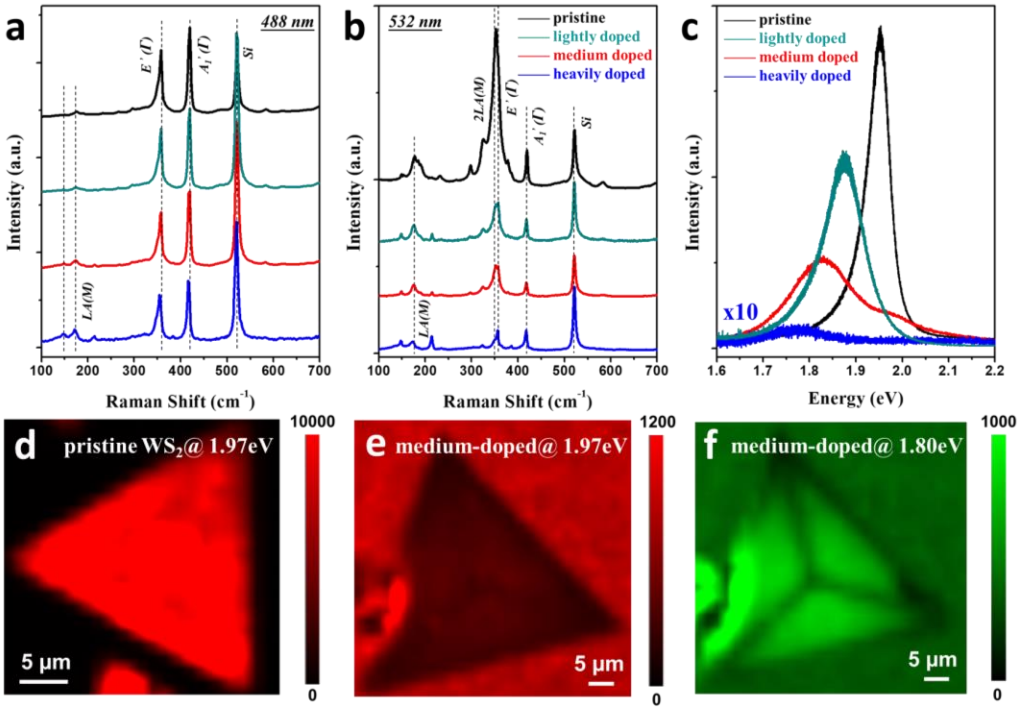

Figure 6- 9 Optical properties of pristine and V-doped WS_2 monolayers. Raman spectra (a) at 488 nm excitation laser, (b) at 532 nm excitation laser, and (c) photoluminescence of pristine, lightly-doped (0.4%), medium-doped (2%) and heavily-doped (8%) WS_2 monolayers, respectively; (d) PL mappings of pristine WS_2 monolayer showing the intensity of the response at 1.97 eV; PL mappings of pristine WS_2 monolayer showing the intensity of the response at (e) 1.97 eV and (f) 1.80 eV, respectively. a.u., normalized Raman/PL intensity shown in arbitrary units.

Peak position (cm^{-1}) @532 nm	E' (cm^{-1})	A_1' (cm^{-1})
pristine	357.6	419.3
Lightly doped	357.3	418.9
Moderate doped	356.2	417.7
Heavily doped	353.4	416.0
Peak position (cm^{-1}) @532 nm	**E'+2LA(M) (cm^{-1})**	**A_1' (cm^{-1})**
pristine	352.8	419.6
Lightly doped	352.1	418.9
Moderate doped	351.9	418.6
Heavily doped	356.2	417.5

Table 6- 1 E'(Γ) and A_1'(Γ) peak positions in Raman spectra

In pristine WS_2 monolayers under 532 nm excitation, a high-intensity second-order double resonance peak involving two longitudinal acoustic phonons appears (2LA(M), Fig. 6-9b).[25] This double resonant process was progressively suppressed under increasing vanadium concentration, indicating substantial changes in the WS_2 electronic structure which drive the system out of resonance for both phonon-electron and phonon-hole mediated processes.[17,25] Pristine monolayers of WS_2 show an intense PL peak at 1.97 eV corresponding to the A exciton[26]. The optical bandgap decreases under increasing vanadium doping, while the photoluminescence broadens (likely due to lattice disorder from dopants possibly accompanied by vacancies) and drops in intensity (Fig. 6-9c). This evolution of the PL response is consistent with the Raman results discussed above. The PL peak broadened and shifted progressively towards lower energies. PL mappings clearly indicate a uniform PL intensity throughout the pristine WS_2 monolayer, located at 1.97 eV (Fig. 6-9d-f). The emission from a representative V-WS_2 triangular monolayer remains uniform in intensity, however the emission is located at 1.80 eV.

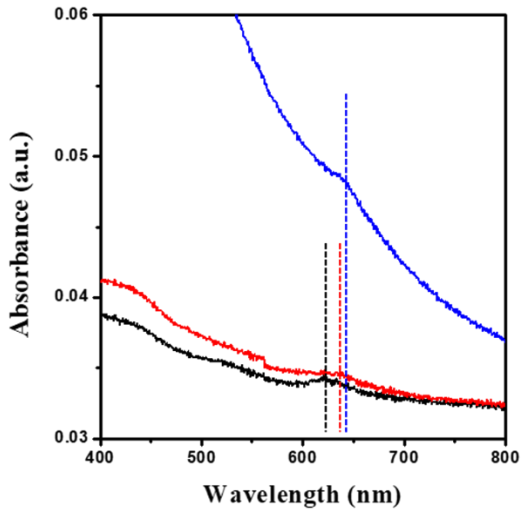

WS_2	Wavelength	Energy
Pristine (black)	622.5 nm	1.99 eV
Moderate doped (red)	639 nm	1.94 eV
Heavily doped (blue)	645 nm	1.922 eV

Figure 6- 10 UV-Vis spectra of the V-doped WS_2 samples transferred onto quartz substrates.

The red shifts of the A exciton observed in the ultraviolet-visible (UV-vis) spectra (Fig. 6-10) further support a bandgap reduction driven by vanadium doping. The A exciton can be observed at 622.5 nm (1.99 eV) in the pristine WS_2, which corresponds to the excitonic absorption at the K point of the Brillouin zone. This is one of the characteristic absorption peaks of the monolayered WS_2. As the V doping level increases, the A excitonic transition gradually shifts from 1.99 eV (608 nm) to 1.94 eV (639 nm) in moderate-doped WS_2 (red), and 1.922 eV (645 nm) in heavily-doped WS_2. The red shifts in the A excitonic transitions further support the bandgap reduction via V doping.

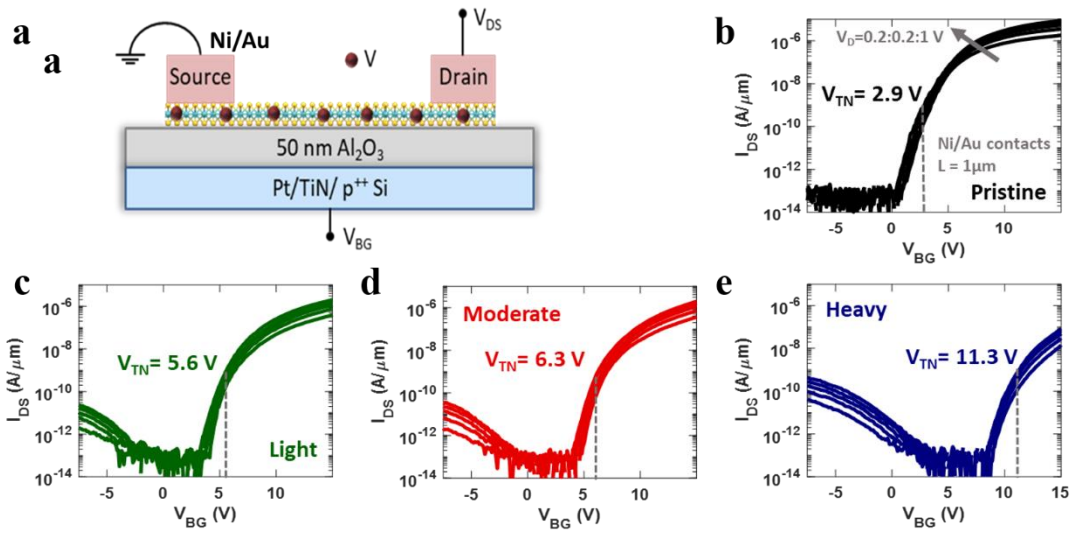

Figure 6- 11 (a) Schematic of a back-gated V-doped WS_2 FET fabricated on a 50nm thick Al_2O_3 substrate with Pt/TiN/p^{++} back-gate electrode for electronic transport measurement for each doping level. (b)-(d) Drain current (I_{DS}) versus back-gate voltage (V_{BG}) (obtained for drain voltages from 0.2 to 1V in 0.2V steps) show a steady shift in threshold voltage across different doping levels and achieve close-to-symmetric ambipolar conduction in heavily doped WS_2.

The back-gated FET geometry shown schematically in Fig. 6-11a (details in Methods) was used to characterize the electronic transport; Figures 6-11 b-d shows the drain current (I_{DS}) versus back-gate voltage (V_{BG}) for 0, 0.4, 2, and 8 at.% vanadium monolayers for various drain voltages (V_D). The 0 at.% device shows unipolar electron conduction with no hole current, as expected for a pristine WS_2-based FET. A small hole branch emerges at 0.4at.% doping, with increasing hole currents at higher doping levels as the threshold voltage shifts from 2.9 volts in the pristine system to 5.6, 6.3, and 11.3 volts in devices with progressively higher doping levels (we extract V_{TN} by the iso-current method for a current of 1 nA/μm at V_D=1 volt). The systematic threshold shift confirms *p*-type doping, with the most heavily doped sample demonstrating close-to-symmetric ambipolar transport.

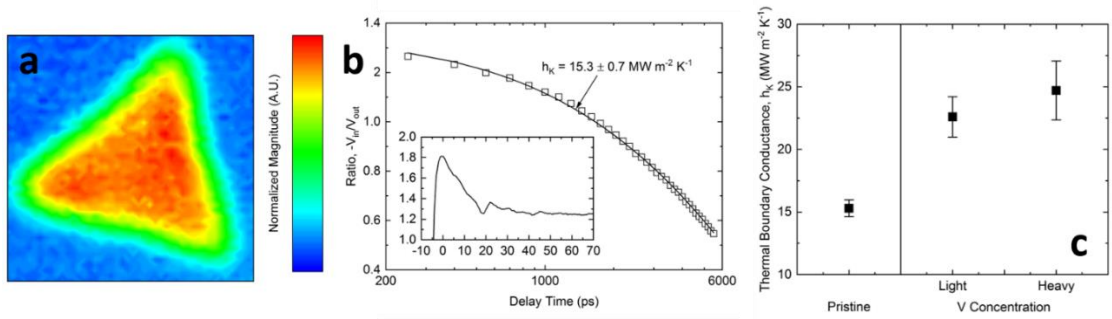

Figure 6- 12 (a) Time-domain thermoreflectance (TDTR) magnitude micrograph of a pristine single-crystal WS_2 flake. (b) TDTR model and best fit for the conductance at the Al/pristine WS_2/SiO_2 interface. The inset shows the picosecond acoustics response at earlier time delays. (c) Results for the thermal boundary conductance at Al/doped WS_2/SiO_2 interfaces.

The thermal boundary conductances (h_K) of the devices were measured at the Al / V-WS_2 / SiO_2 interface by time-domain thermoreflectance (Fig. 6-12). An example of this magnitude micrograph can be seen in Fig. 6-12a for a pristine WS_2 flake. The uniformity of the TR magnitude of the WS_2 flake suggests that the conductance is uniform. Full time delay TDTR measurements near the center of the triangles were examined for pristine WS_2 and V-doped WS_2 samples. The TDTR curve and best fit are shown in Fig. 6-12b for the pristine flake, where the inset shows the short delay time picosecond acoustic response, with which we used to extract the thickness of our Al transducer. This type of measurement was performed on lightly- (0.4%) and highly-doped (8%) V-WS_2 crystals as well. The final results are shown in Fig. 6-12c for all flakes measured, where an increase in the Al/WS_2/SiO_2 interface was observed as the V doping concentration increased. The enhancement in conductance is correlated with the V substitutional sites in the WS_2 lattice. It is assumed that the inclusion of V sites serves to alter the localized phonon density of states, allowing for an ameliorated thermal conductance as the concentration of V sites is increased. The improvement of heat dissipation of the V-doped WS_2 is promising as an electronic circuit component.

6.5 Magnetic properties of V-doped WS_2 monolayers

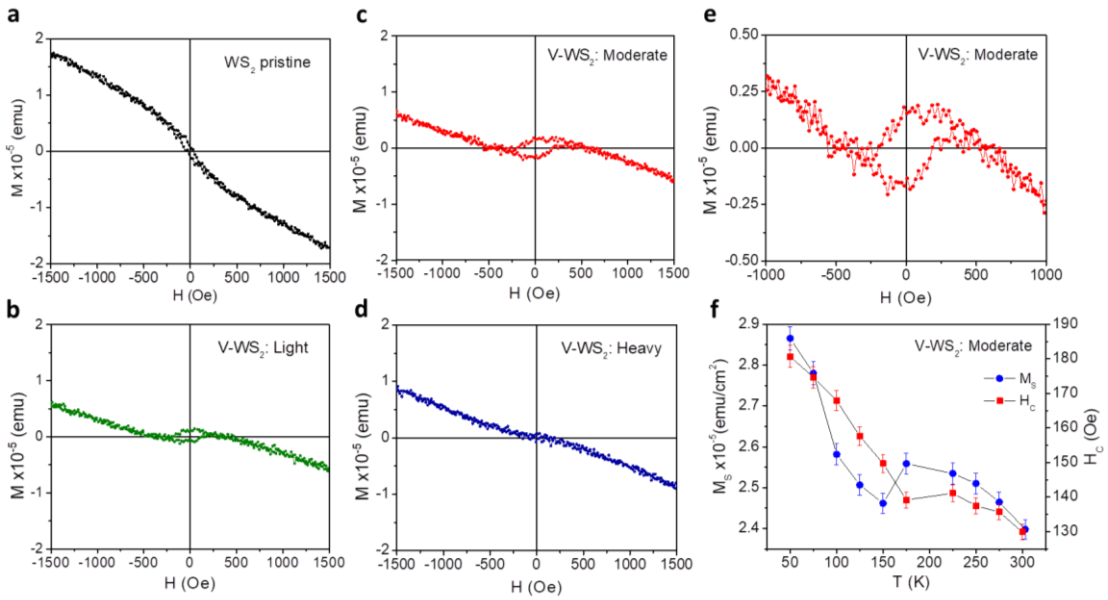

Figure 6- 13 Magnetic characterization of pristine and V-doped WS_2 monolayers. Magnetization versus field loops taken at 300 K for V-WS_2 samples at different doping levels (pristine, 0.4, 2, and 8at.%.), including an expanded view of the hysteresis loop for the 2 at.% sample and its temperature-dependent saturation magnetization (M_S) and coercivity (H_C).

The magnetic properties of pristine and V-doped WS_2 monolayer samples were measured by a vibrating sample magnetometer. To exclude unwanted effects on the magnetization versus magnetic field (*M-H*) loops from subtracting diamagnetic and paramagnetic backgrounds[27,28], Figure 6-13 presents as-measured *M-H* loops (at 300K, for samples at 0, 0.4, 2 and 8at.% doping levels) and deduce the saturation magnetization and coercive field directly from these loops. The pristine WS_2 sample exhibits a very weak ferromagnetic signal on a diamagnetic background, which we tentatively ascribe to unpaired sulfur p electrons at zig-zag monolayer edges.[29,30] Vanadium doping of 0.4at.%. greatly increases the ferromagnetic signal (M_S and H_C) with further strengthening at 2at.% doping, but a much weaker ferromagnetic response at the highest (8at.%) vanadium concentrations. The ferromagnetism observed in V-doped samples is too strong to originate from edge effects, and its dependence on vanadium concentration strongly suggests an

origin in local moments of unpaired spins on V orbitals hybridizing with W 5d and S 3p states.[4,27,31] The 2at.% WS_2 sample shows large, clear hysteresis loops at all temperatures, from which M_S and H_C are determined and plotted as a function of temperature. Coupled with the HAADF-STEM image and V-V dopant near neighbor distance analysis (Fig. 6-4c, histograms in Fig. 6-14, averaged distances as a function of doping concentrations in Fig. 6-15), the sharp increase in both M_S and H_C below ~160 K (Fig. 3f) can be attributed to the onset of the long-range ferromagnetic ordering between V dopants at large distances (~2 nm), in addition to the order between V-dopants at short distances (~0.5 nm) occurring at higher temperature (above 300 K). The saturation magnetization and coercivity both increase with decreasing temperature, but there is an interesting non-monotonicity of both around 150–200K which we discuss below in the context of first-principles results on competing ferromagnetic and anti-ferromagnetic orders and HAADF-STEM imaging of vanadium-vanadium separations.

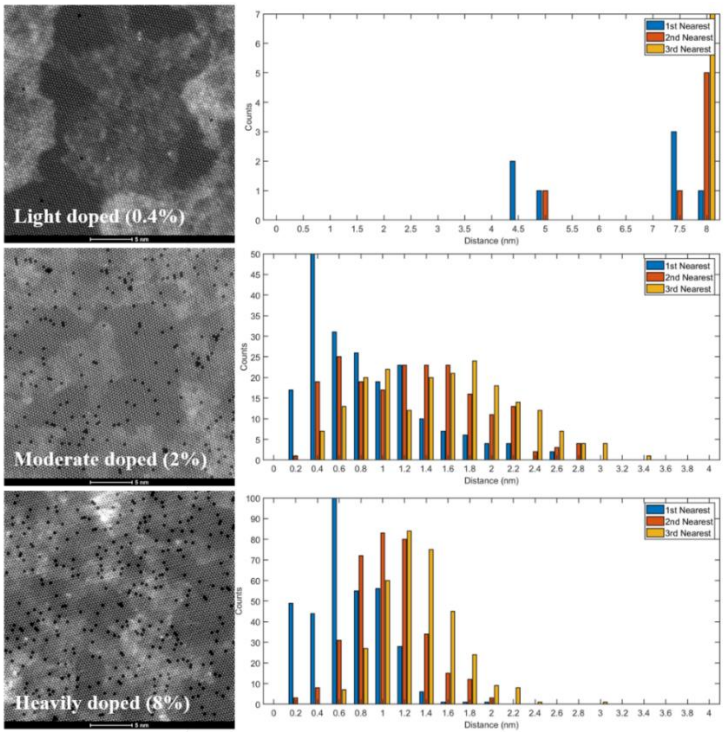

Figure 6- 14 HAADF-STEM images of V-doped WS_2 and the corresponding histogram of V-V near neighbor distance distribution analyses.

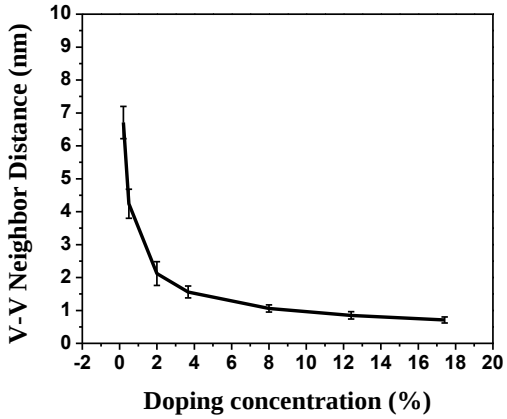

Figure 6- 15 Plot of V-V near neighbor average distance as a function of V doping concentration, analyzed by HAADF-STEM images.

6.6 DFT calculation and origin of ferromagnetism in V-doped WS_2 monolayers

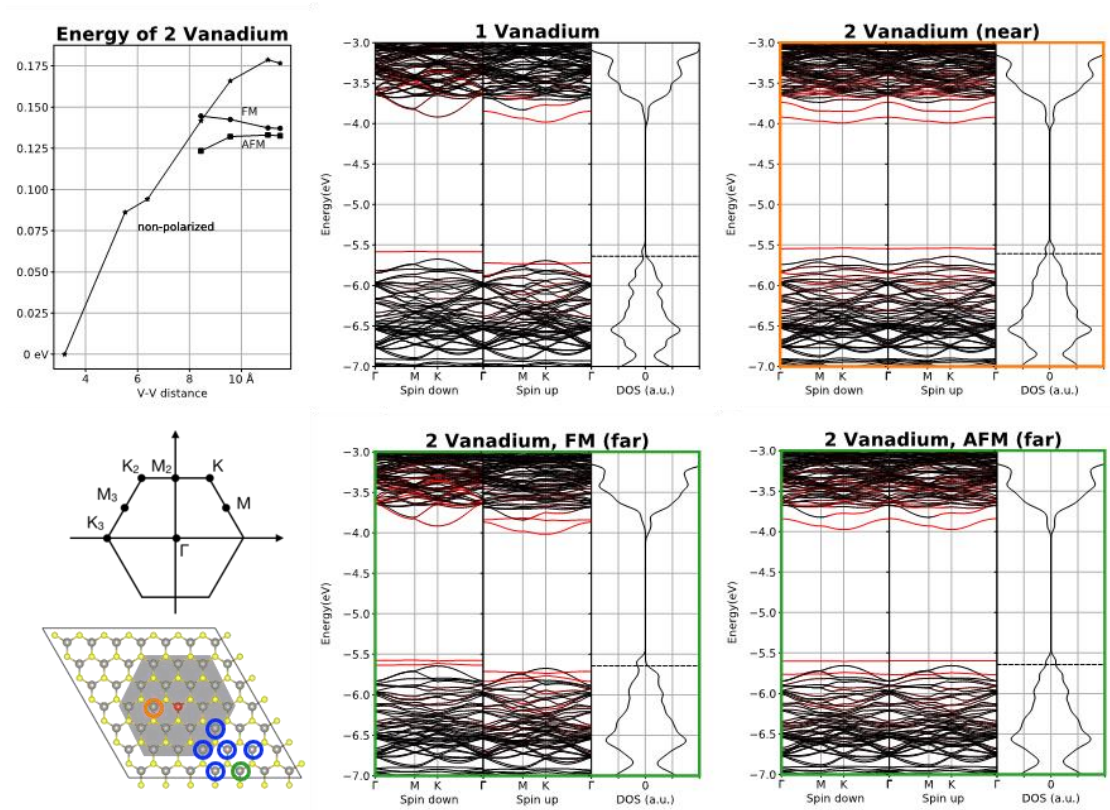

Figure 6- 16 DFT calculation results for V-doped WS_2 monolayers. In the energy plot for 7×7 WS_2 with 2 V, the nearest neighbor case is the reference point. All the possible non-equivalent positions for the second V dopant are circled at the lower left corner and the band structures of the nearest and the farthest sites have been plotted. The shaded area shows where the second V will quench the magnetic moments of both dopants. The red curve is to qualitatively show the projection on V d_{z^2} atomic orbital.

We examined isolated vanadium and the relative stability of ferromagnetic and anti-ferromagnetic states of a pair of vanadium in a set of range of separations in a 7×7 supercell. A single V dopant can provide 1 unpaired electron (or hole) occupying a spin-split defect state (Fig. 6-16b) with V d_{z^2} character.[9] For two V dopants in a 7×7 supercell, if they are far away from each other (Figs. 6-16e and f), they provide 2 local magnetic moments. Two observations are supporting this picture. First, the ferromagnetic and the anti-ferromagnetic states have almost the same energy (4.5 meV difference is within the calculation uncertainty). Second, for the ferromagnetic state (Fig. 6-16e), in spite of small covalent interaction between defect states as indicated by energy level repulsion in the band structure, and the orbital hybridization in real space, we obtain 2 μ_B, while in an anti-ferromagnetic state (Fig. 6-16f), the spin-up level of one defect state is degenerate with the spin-down level of the other defect state, and little hybridization is found between these two defect states. If the two vanadium dopants are too close to each other (Fig. 6-16c), the magnetic moments are quenched due to orbital hybridization. It is found that if the two dopants are neighboring or sharing their nearest W neighbors, their defect states will hybridize strongly and show no spin splitting (Shaded area in Fig. 6-16d). Otherwise, the total magnetic moments is 2 μ_B. Considering the random distribution of V atoms inside of WS2 lattice, gives the optimal level 1/19=5.3% and the rough estimation of saturation magnetization is 2.26×10^{-3} μ_B/nm^2. The AFM state is slightly preferred energetically but the AFM and FM magnetic orderings are competitive arrangement of local moments (Fig. 6-16a).

6.7 Chapter summary

Two-dimensional diluted magnetic semiconductors own unprecedented physical properties related to spin behavior in low dimensions, and also hold great promise in the fabrication of novel magneto-electric and magneto-optical devices. This study successfully develops scalable and controllable synthesis routes for monolayer DMSs with intrinsic ferromagnetic ordering at room temperature. High quality V-doped WS_2 monolayers with various doping concentrations were synthesized by single-step powder vaporization. The reduction of the optical bandgap and the emergence of p-type transport (reaching ambipolarity) are observed as the vanadium ~~doping~~ concentration increases. The V-doped WS_2 monolayers also show modulated inherent ferromagnetic ordering at room temperature, reaching the strongest ferromagnetic signal for the moderately-doped (2at.%.) sample. Atomic resolution TEM imaging combining with DFT calculations pinpoint the effect of the V-V distance on the local magnetic moments within the V-WS_2 monolayer and the upper doping limit for optimal ferromagnetism is predicted as 5.3%. Such dilute magnetic semiconductors based on magnetic element doped transition metal dichalcogenides exhibit great promise as future spintronic devices, with novel magneto-electric and magneto-optical applications.

6.8 References

1. Ohno, H.; Shen, A.; Matsukura, F.; Oiwa, A.; Endo, A.; Katsumoto, S.; Iye, Y., (Ga, Mn) As: a new diluted magnetic semiconductor based on GaAs. *Applied Physics Letters* **1996,** *69* (3), 363-365.

2. Dietl, T.; Ohno, H., Dilute ferromagnetic semiconductors: Physics and spintronic structures. *Reviews of Modern Physics* **2014,** *86* (1), 187.

3. Pappert, K.; Schmidt, M.; Hümpfner, S.; Rüster, C.; Schott, G.; Brunner, K.; Gould, C.; Schmidt, G.; Molenkamp, L., Magnetization-switched metal-insulator transition in a (Ga, Mn) As tunnel device. *Physical review letters* **2006,** *97* (18), 186402.

4. Yun, S. J.; Duong, D. L.; Doan, M.-H.; Singh, K.; Phan, T. L.; Choi, W.; Kim, Y.-M.; Lee, Y. H., Room-temperature ferromagnetism in monolayer WSe_2 semiconductor via vanadium dopant. *arXiv preprint arXiv:1806.06479* **2018**.

5. Habib, M.; Muhammad, Z.; Khan, R.; Wu, C.; ur Rehman, Z.; Zhou, Y.; Liu, H.; Song, L., Ferromagnetism in CVT grown tungsten diselenide single crystals with nickel doping. *Nanotechnology* **2018,** *29* (11), 115701.

6. Wang, Y.; Li, S.; Yi, J., Electronic and magnetic properties of Co doped MoS_2 monolayer. *Scientific reports* **2016,** *6*, 24153.

7. Ramasubramaniam, A.; Naveh, D., Mn-doped monolayer MoS_2: an atomically thin dilute magnetic semiconductor. *Physical Review B* **2013,** *87* (19), 195201.

8. Dietl, T., Ferromagnetic semiconductors. *Semiconductor Science and Technology* **2002,** *17* (4), 377.

9. Gao, Y.; Ganguli, N.; Kelly, P. J., Itinerant ferromagnetism in p-doped monolayers of MoS_2. *Physical Review B* **2019,** *99* (22), 220406.

10. Li, H.; Liu, S.; Huang, S.; Yin, D.; Li, C.; Wang, Z., Impurity-induced ferromagnetism and metallicity of WS_2 monolayer. *Ceramics International* **2016,** *42* (2), 2364-2369.

11. Ma, Y.; Dai, Y.; Guo, M.; Niu, C.; Lu, J.; Huang, B., Electronic and magnetic properties of perfect, vacancy-doped, and nonmetal adsorbed $MoSe_2$, $MoTe_2$ and WS_2 monolayers. *Physical Chemistry Chemical Physics* **2011,** *13* (34), 15546-15553.

12. Ohno, H.; Chiba, D.; Matsukura, F.; Omiya, T.; Abe, E.; Dietl, T.; Ohno, Y.; Ohtani, K., Electric-field control of ferromagnetism. *Nature* **2000,** *408* (6815), 944.

13. Chang, C.-Z.; Zhang, J.; Feng, X.; Shen, J.; Zhang, Z.; Guo, M.; Li, K.; Ou, Y.; Wei, P.;

Wang, L.-L., Experimental observation of the quantum anomalous Hall effect in a magnetic topological insulator. *Science* **2013,** *340* (6129), 167-170.

14. Gutiérrez, H. R.; Perea-López, N.; Elías, A. L.; Berkdemir, A.; Wang, B.; Lv, R.; López-Urías, F.; Crespi, V. H.; Terrones, H.; Terrones, M., Extraordinary room-temperature photoluminescence in triangular WS_2 monolayers. *Nano letters* **2012,** *13* (8), 3447-3454.

15. Ovchinnikov, D.; Allain, A.; Huang, Y.-S.; Dumcenco, D.; Kis, A., Electrical transport properties of single-layer WS_2. *ACS nano* **2014,** *8* (8), 8174-8181.

16. Zhang, K.; Bersch, B. M.; Joshi, J.; Addou, R.; Cormier, C. R.; Zhang, C.; Xu, K.; Briggs, N. C.; Wang, K.; Subramanian, S., Tuning the electronic and photonic properties of monolayer MoS_2 via in situ rhenium substitutional doping. *Advanced Functional Materials* **2018,** *28* (16), 1706950.

17. Zhang, F.; Lu, Y.; Schulman, D. S.; Zhang, T.; Fujisawa, K.; Lin, Z.; Lei, Y.; Elias, A. L.; Das, S.; Sinnott, S. B., Carbon doping of WS_2 monolayers: Bandgap reduction and p-type doping transport. *Science advances* **2019,** *5* (5), eaav5003.

18. Suh, J.; Park, T.-E.; Lin, D.-Y.; Fu, D.; Park, J.; Jung, H. J.; Chen, Y.; Ko, C.; Jang, C.; Sun, Y., Doping against the native propensity of MoS_2: degenerate hole doping by cation substitution. *Nano letters* **2014,** *14* (12), 6976-6982.

19. Han, G. H.; Kybert, N. J.; Naylor, C. H.; Lee, B. S.; Ping, J.; Park, J. H.; Kang, J.; Lee, S. Y.; Lee, Y. H.; Agarwal, R., Seeded growth of highly crystalline molybdenum disulphide monolayers at controlled locations. *Nature communications* **2015,** *6*, 6128.

20. Zhang, X.; Al Balushi, Z. Y.; Zhang, F.; Choudhury, T. H.; Eichfeld, S. M.; Alem, N.; Jackson, T. N.; Robinson, J. A.; Redwing, J. M., Influence of carbon in metalorganic chemical vapor deposition of few-layer WSe_2 thin films. *Journal of Electronic Materials* **2016,** *45* (12), 6273-6279.

21. Azizi, A.; Wang, Y.; Lin, Z.; Wang, K.; Elias, A. L.; Terrones, M.; Crespi, V. H.; Alem, N.,

Spontaneous formation of atomically thin stripes in transition metal dichalcogenide monolayers. *Nano letters* **2016,** *16* (11), 6982-6987.

22. Azizi, A.; Wang, Y.; Stone, G.; Elias, A. L.; Lin, Z.; Terrones, M.; Crespi, V. H.; Alem, N., Defect Coupling and Sub-Angstrom Structural Distortions in $W_{1-x}Mo_xS_2$ Monolayers. *Nano letters* **2017,** *17* (5), 2802-2808.

23. Carvalho, B. R.; Wang, Y.; Mignuzzi, S.; Roy, D.; Terrones, M.; Fantini, C.; Crespi, V. H.; Malard, L. M.; Pimenta, M. A., Intervalley scattering by acoustic phonons in two-dimensional MoS_2 revealed by double-resonance Raman spectroscopy. *Nature communications* **2017,** *8*, 14670.

24. Sun, X.; Dai, J.; Guo, Y. Q.; Wu, C. Z.; Hu, F. T.; Zhao, J. Y.; Zeng, X. C.; Xie, Y., Semimetallic molybdenum disulfide ultrathin nanosheets as an efficient electrocatalyst for hydrogen evolution. *Nanoscale* **2014,** *6* (14), 8359-8367.

25. Berkdemir, A.; Gutiérrez, H. R.; Botello-Méndez, A. R.; Perea-López, N.; Elías, A. L.; Chia, C.-I.; Wang, B.; Crespi, V. H.; López-Urías, F.; Charlier, J.-C., Identification of individual and few layers of WS_2 using Raman Spectroscopy. *Scientific reports* **2013,** *3*.

26. Cong, C.; Shang, J.; Wu, X.; Cao, B.; Peimyoo, N.; Qiu, C.; Sun, L.; Yu, T., Synthesis and Optical Properties of Large-Area Single-Crystalline 2D Semiconductor WS_2 Monolayer from Chemical Vapor Deposition. *Advanced Optical Materials* **2014,** *2* (2), 131-136.

27. Coelho, P. M.; Komsa, H. P.; Lasek, K.; Kalappattil, V.; Karthikeyan, J.; Phan, M. H.; Krasheninnikov, A. V.; Batzill, M., Room-Temperature Ferromagnetism in $MoTe_2$ by Post-Growth Incorporation of Vanadium Impurities. *Advanced Electronic Materials* **2019,** *5* (5), 1900044.

28. O'Hara, D. J.; Zhu, T.; Kawakami, R. K., Importance of Paramagnetic Background Subtraction for Determining the Magnetic Moment in Epitaxially Grown Ultrathin van der Waals Magnets. *IEEE Magnetics Letters* **2018,** *9*, 1-5.

29. Huo, N.; Li, Y.; Kang, J.; Li, R.; Xia, Q.; Li, J., Edge-states ferromagnetism of WS_2 nanosheets. *Applied Physics Letters* **2014,** *104* (20), 202406.

30. Tao, L.; Meng, F.; Zhao, S.; Song, Y.; Yu, J.; Wang, X.; Liu, Z.; Wang, Y.; Li, B.; Wang, Y., Experimental and theoretical evidence for the ferromagnetic edge in WSe_2 nanosheets. *Nanoscale* **2017,** *9* (15), 4898-4906.

31. Zhao, X.; Dai, X.; Xia, C., Magnetic properties of two nearest Cu-doped monolayer WS_2: A first-principles study. *Solid State Communications* **2015,** *217*, 66-69.

Chapter 7

Conclusion and Perspectives

In this dissertation, we have done a systematic study on the material synthesis, characterization and property investigations on transition metal dichalcogenides based heterostack and alloys, the detailed summary of the thesis are shown below:

(1) A defect-controlled approach for the nucleation and epitaxial growth of WSe_2 on hBN is demonstrated. The WSe_2 domains exhibit a preferred orientation of over 95% leading to a reduced density of inversion domain boundaries upon coalescence. First-principles calculations and experimental studies include detailed TEM analysis provides support for the role of single-atom vacancies on the hBN surface which trap W atoms and break surface symmetry leading to a reduced formation energy for one orientation of WSe_2 domains. Low temperature PL measurements and transport measurements of backgated FET devices fabricated on WSe_2/hBN films show improved optical and electrical properties compared to films grown on sapphire under similar conditions. Our results reveal an important nucleation mechanism for epitaxial growth of van der Waals heterostructures and demonstrate hBN as a superior substrate for single crystal transition metal dichalcogenide films, resulting in a reduced density of IDBs and improved properties. The results motivate further efforts focused on the development of single crystal hBN substrates and epilayers for synthesis of wafer-scale single crystal TMD films, further understanding of nucleation mechanism for van der Waal solids is yet to be explored.

(2) High quality superconducting α-phase molybdenum carbide (Mo_2C) flakes were used to engineer 2D molybdenum carbide/disulfide heterostructures, exhibiting moiré patterns. Our sulfurization assisted synthesis approach induced controlled successive phase transitions between

various superconducting phases, which led to consecutive increases in T_C. These findings provide an insight into the formation mechanism and stacking of the synthesized TMC/TMD heterostructures, studying various possible epitaxial-strained or moiré configurations that can be synthesized. Our approach opens the possibility of inducing superconductivity in topological non-trivial surface states of the MoC phases, particularly in the γ-MoC, through the fabrication of heterostructures with α-Mo_2C and could be generalized for other metal carbide and nitride systems, thus opening new opportunities for quantum information sciences. Fabrication of catalysis electrode for HER and assembly of Josephson junctions by TMC/TMD heterostructures are intriguing topics to study.

(3) We have used a plasma-assisted method to introduce carbon-hydrogen (CH) units into monolayer WS_2. We have found these CH groups to be the most stable dopant to anchor carbon in WS_2, leading to a reduction of the optical band gap from 1.98 eV to 1.83 eV, as revealed by photoluminescence spectroscopy. Aberration corrected high-resolution STEM observations in conjunction with first principles calculations indicate that CH groups incorporate into S vacancies within the WS_2 monolayers. To verify the substitution of CH groups within the lattice, Raman spectroscopy, electronic transport and XPS were also carried out. Although undoped WS_2 monolayers exhibit a unipolar n-type conduction, we have found that the carbon-doped WS_2 monolayers show the emergence of a p-branch. The conduction gradually becomes entirely p-type as the carbon doping level increases. Our results indicate that incorporating CH groups into the WS_2 lattice significantly affects the electronic and optical properties of WS_2, thus offering a clear alternative way to effectively tailor the physico-chemical properties of 2D TMD materials and devices. Further investigation on the CH units on catalysis or sensing performance is needed, other similar molecules as CH units substitutional doping into monolayer TMDs are also interesting.

(4) Vanadium-doped tungsten disulfide (V-WS_2) monolayers with a wide spectrum of vanadium concentrations were synthesized by a reliable single-step powder vaporization method. The V-WS_2 monolayers show a consistent reduction of the optical bandgap and the emergence of the p-type transport branch (reaching ambipolarity), as a function of vanadium concentration. Ferromagnetic ordering is simultaneously induced in monolayer V-WS_2 at room temperature and reaches optimal at ~2%at. vanadium concentration. Density functional theory calculations elaborate the experimental findings and, coupled with atomic resolution transmission electron microscopy imaging, reveal the important effect of the V-V near neighbor distance on the local magnetic moments within the V-WS_2 monolayer and predict the upper limit of doping level to reach optimal ferromagnetism is 5.3%at. Such novel two-dimensional room temperature ferromagnetic semiconductors will find wide-ranging applications in spintronics, valleytronics and quantum computing. Fabrication of devices with laser or biasing induced/modulated magnetic performance is under exploring, we also further extend the magnetic doping to other monolayer semiconducting TMD materials to find new functionalities.

This dissertation has systematically demonstrated that the multidiscipline performance of TMDs could be tuned by defect engineering such as introducing foreign atoms into the lattice or by heterostacks formation. Mechanisms associated with these changes were also comprehensively elucidated by combination of material synthesis and atomic resolution TEM anatomy of the structural and chemistry of the 2D TMD materials. The results summarized in this study could contribute to the fabrication of next-generation optoelectronic, magneto-optical and magneto-electronic devices, superconducting devices, which is foreseen that 2D materials could have practical applications in the near future.

VITA

Fu Zhang

Education

Pennsylvania State University PA, USA — August 2017- December 2019
Ph. D. candidate in Materials Science and Engineering, — Advisor: Mauricio Terrones

Pennsylvania State University PA, USA — January 2015-August 2017
M.S. in Material Sciences and Engineering, — Advisor: Nasim Alem

Harbin Institute of Technology Harbin, China — August 2012-December 2014
M.S. in Material Physics and Chemistry, — Advisor: Weidong Fei, co-advisor: Junlei Qi

Dalian University of Technology Dalian, China — August 2008-July 2012
B.S. in Material Physics.

Selected Publications

- **Fu Zhang**, Yanfu Lu, Susan Sinnott, Mauricio Terrones. Carbon doping of WS_2 monolayers: band gap reduction and p-type doping transport. ***Science Advances***, 2019, 5: eaav5003
- **Fu Zhang**, Yuanxi Wang, Vincent Crespi, Nasim Alem. Full orientation control of epitaxial MoS_2 on hBN assisted by substrate defects. ***Physical Review B***, 2019, 99(15), 155430
- **Fu Zhang**, Kasra Momeni, Long-Qing Chen, Joan M. Redwing, Nasim Alem. Understanding controlled synthesis of 2D crystals: From vertical to planar MoS_2. ***2D Materials***, 2017, 4, 025029
- **Fu Zhang**, Nasim Alem. Etchant-free transfer of 2D nanostructures ***Nanotechnology***, 2017, 29 (2), 025602
- Xiaotian Zhang*, **Fu Zhang***, Mauricio Terrones, Joan M. Redwing. Defect-Controlled Nucleation and Orientation of WSe_2 on hBN – A Route to Single Crystal Epitaxial Monolayers ***ACS Nano***, 2019, 13(3), 3341-3352
- Amritanand Sebastian, **Fu Zhang**, Mauricio Terrones, Saptarshi Das. Electrochemical Polishing of Two-Dimensional Materials. ***ACS Nano***, 2019, 13 (1), 78–86
- Tarak K Patra, **Fu Zhang**, Mauricio Terrones, Saptarshi Das. Defect dynamics in 2-D MoS_2 probed by using machine learning, atomistic simulations and high-resolution microscopy. ***ACS Nano***, 2018, *12* (8), 8006–8016
- Daniel S Schulman, Dan May-Rawding, **Fu Zhang** et. al Superior electro-oxidation and corrosion resistance of monolayer transition metal disulfides ***ACS Applied Material and Interfaces***, 2018, 10 (4), 4285–4294
- Xiaotian Zhang, Zakaria Y Al Balushi, **Fu Zhang** et. al Influence of carbon in metalorganic chemical vapor deposition of few-layer WSe_2 thin films, ***Journal of Electronic Materials***, 2016, 12, 6273-6279
- Junlei Qi, Xu Wang, Jing-Huang Lin, **Fu Zhang** et. al Vertically oriented few-layer graphene-nanocup hybrid structured electrodes for high-performance supercapacitors. ***Journal of Materials Chemistry A***, 2015, 3, 12396-12403